Diapycnal mixing and the internal wave field north of the Kerguelen Plateau

Amélie Meyer
M.Sc. Oceanography

A thesis submitted in complete fulfilment of the requirements of the Doctor of Philosophy in the CSIRO-UTAS Ph.D. Program in Quantitative Marine Science.

Institute for Marine and Antarctic Studies
(IMAS)
University of Tasmania

April, 2014

0.1 Declaration

This thesis contains no material which has been accepted for a degree or a diploma by the University or any other institution, except by way of background information and duly acknowledged in the thesis, and to the best of my knowledge and belief, no material previously published or written by another person except where due acknowledgment is made in the text of the thesis, nor does the thesis contain any material that infringes copyright.

Amélie Meyer

April 22, 2014

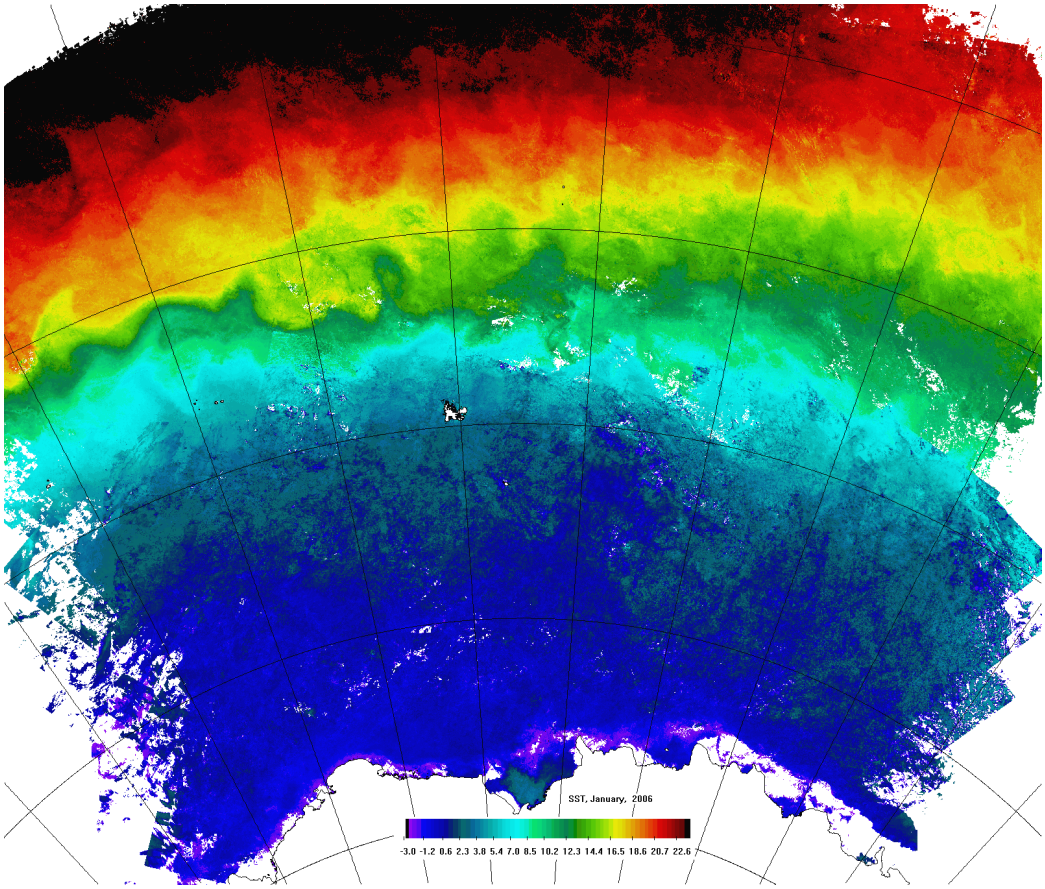

Figure 1: Kerguelen Island region sea-surface temperature composite.

0.2 Abstract

Dissipating internal waves are the main source of mixing in the stratified ocean. Recent observational and modelling studies in the Southern Ocean primarily associate the generation of internal waves with either wind forcing or with rough topography. This work explores the nature of mixing and its sources north of the Kerguelen Plateau, a large topographic feature in the Southern Ocean. Based on novel observations, we present the distribution and intensity of mixing, and the internal wave field properties.

This thesis includes (i) a regional description of the Kerguelen Plateau oceanographic characteristics; (ii) estimates of mixing and its sources; and (iii) a study of the internal wave field in the vicinity of the Plateau. The data consist of 914 temperature, salinity, pressure and horizontal velocity profiles from Electromagnetic Autonomous Profiling Explorer (EM-APEX) floats deployed northeast of the Kerguelen Plateau in 2008. We are able to estimate diapycnal mixing in the upper 1600 m of the water column. To estimate mixing, we apply both a Thorpe-scale analysis on density inversions and a shear-strain parameterization method and compare the estimates with direct microstructure measurements.

The observational results provide the first clear connection between the distribution and intensity of mixing, and the associated internal wave field properties. In the Kerguelen Plateau area, mean mixing from the EM-APEX data is slightly larger (diffusivity of $O(10^{-5}m^2s^{-1})$) than typical open-ocean background levels. Mixing intensities show strong spatial and temporal variability reaching considerably large values close to the Plateau (diffusivity of $O(10^{-3}m^2s^{-1})$). Topographic roughness at the seafloor, mean current speed and wind speed are identified as important factors in determining local dynamical mixing regimes. In particular, identified fronts of the Antarctic Circumpolar Current are associated with the most intense mixing and internal wave activity of the region. Using our mixing observations from the Kerguelen region, we infer a water-mass transformation rate of 17 Sv ($1\,Sv=10^6m^3s^{-1}$) across the boundary of Antarctic Intermediate Water and Upper Circumpolar Deep Water in the Antarctic Circumpolar Current for

the entire Southern Ocean.

We identify 46 internal waves with characteristics that support the findings from the mixing analysis. The properties and location of the observed internal waves are dependent on regional dynamics. Mixing is enhanced in areas where internal waves are identified. There is clear evidence that the enhanced mixing and internal wave activity in the front results from dissipating internal waves generated by the interaction of the frontal jet and the rough topography of the Kerguelen Plateau.

This analysis demonstrates the value of the floats to better understand upper ocean dynamics and processes driving the internal wave and mixing field. The results suggest that north of the Kerguelen Plateau, internal waves generated by the interaction of the flow and rough topography play a bigger role in enhancing mixing than internal waves generated by wind at the ocean surface.

0.3 Acknowledgements

First and foremost, thank you to my thesis supervisors, Helen Phillips, Bernadette Sloyan, Nathan Bindoff and Kurt Polzin for their guidance and patience over the past five years. This work would not have been possible without their continuous support.

I thank the SOFine group for a fantastic research cruise, JC029, that provided many opportunities and a great data set.

Many thanks to Stephanie Waterman, Alberto Naveira Garabato, Clothilde Langlais, Paul Durack, Jean-Baptiste Sallee, Andrew Meijers, Emlyn Jones, Les Muir, Stephanie Downes, Mathieu Mongin, Esmee VanWijk, and others who have provided advice, suggestions and shared their knowledge. I feel privilege to have benefited from so much advice.

I would also like to thank individuals who have been particularly encouraging throughout my years as a graduate student: Susan Wijffels, Trevor McDougall, Denbeigh Armstrong and Richard Matear.

Stephanie Waterman, Clothilde Langlais and Beatriz Pena-Molino provided their time and invaluable comments on the manuscript.

As reviewers, both Jennifer MacKinnon and Andrew Thompson provided very thorough and constructive feedback, for which I am grateful.

Finally a big thank you to my family, in particular Clint and our little Amandine, for their unwavering support. The past few years have been extremely happy, rewarding and rich with enlightenment.

Funding for this project was provided by the UTAS Quantitative Marine Science (QMS) program and the 2009 CSIRO Wealth from Ocean Flagship Collaborative Fund Postgraduate Top Up Scholarship.

Contents

List of Figures

List of Tables

Chapter 1

INTRODUCTION

In the stratified ocean, turbulent mixing is primarily attributed to the breaking of internal waves. Internal waves in the Southern Ocean are thought to be mostly generated by inertial wind forcing. However, it has recently been suggested that in certain regions of the Southern Ocean, the interaction between the Antarctic Circumpolar Current (ACC) or tidal flows and rough topography is a significant source of internal waves (Naveira Garabato et al., 2004; Nikurashin and Ferrari, 2010). Dissipating internal waves are the source of ocean turbulence. There is growing evidence that enhancement of turbulent mixing over regions of rough topography affects the abyssal stratification, circulation of the Southern Ocean and the global overturning circulation. This thesis investigates small-scale diapycnal turbulent mixing and its sources north of the Kerguelen Plateau, an important topographic feature in the Southern Ocean.

1.1 Turbulent mixing

In the ocean, mixing results from density overturns driven by wave breaking and Kelvin-Helmholtz instabilities. Turbulent mixing leads to the transfer of kinetic energy into heat by viscous dissipation. The heat generated by turbulence is small compared to that of other sources (Thorpe, 2005), but the total loss in energy by turbulent motions is substantial and must be balanced by other energy sources for the ocean to remain in quasi-steady state. As such, turbulent mixing can control the strength of the ocean's overturning circulation (Bryan, 1987), dissipating energy from the winds and tides.

A key remaining challenge in physical oceanography is the understanding and parameterization of small-scale mixing in the oceans (Alford et al., 2012). In spite of much work on new instruments and techniques to measure turbulence in the ocean, data sets of mixing are still sparse and our limited understanding of the physical processes behind turbulent mixing leads to inaccurate representations of mixing in ocean general circulation models (OGCMs) (Wunsch and Ferrari, 2004). High resolution modelling studies have shown that the uptake and storage of tracers, such as heat, salt, nutrients and dissolved gases, are very sensitive to the temporal and spatial

variations of mixing (Harrison and Hallberg, 2008). With turbulent mixing playing such a key role in the ocean overturning circulation, ocean's energy, carbon and nutrient budgets, it is crucial to correctly represent mixing in ocean models (Gregg et al., 2003).

The eddy diffusion coefficient of mass across isopycnal surfaces, called diapycnal turbulent eddy diffusivity of mass and hereinafter referred to as diffusivity (K_ρ), is used to characterise turbulent mixing in the ocean. It is defined by the flux gradient relation

$$F_c = -K_c \nabla C, \tag{1.1}$$

where F_c is the flux of some property C, K_c is the diffusivity of that property and ∇C its gradient. Assuming C is density, a positive diffusivity flux will decrease the density gradient and conversely, a negative diffusivity flux will increase the density gradient (i.e. increase stratification). Double diffusion is an example of a process associated with a negative diffusivity flux.

The rate of loss of the kinetic energy of the turbulent motion per unit mass through viscosity to heat is often referred to as the turbulent kinetic energy dissipation rate (ϵ), hereinafter referred to as the dissipation rate. The dissipation rate has typical values that range from $1 \times 10^{-10}\,\mathrm{W\,kg^{-1}}$[1] in the abyssal ocean, to $1 \times 10^{-1}\,\mathrm{W\,kg^{-1}}$ in areas such as the surf zone. Diffusivity can be estimated from the turbulent kinetic energy dissipation rate by applying the Osborn (1980) relation (see Chapter 4.1.2, Section 4.2.2).

1.1.1 Mixing and the Southern Ocean

The Southern Ocean is the only ocean with no meridional continental barriers, allowing for the existence of the ACC, an eastward flowing current composed of many fronts, which connects the three major ocean basins (Figure 1.1). The meridional overturning circulation is composed of the flow of deep waters generated at high latitudes and the compensating return flow of less dense waters. The Southern Ocean meridional circulation consists of the

[1] $1\,\mathrm{W\,kg^{-1}} = 1\,\mathrm{m^2\,s^{-3}}$

upwelling to the surface of northern-sourced Deep Waters and the production of dense Antarctic Bottom Water and intermediate waters (Figure 1.1), and is driven by winds and surface buoyancy forcing (Talley, 2013). The Southern Ocean therefore regulates fluxes of heat, freshwater and carbon between the surface and deep ocean, and thus, is an important component of the Earth's climate (Rintoul and Naveira Garabato, 2013).

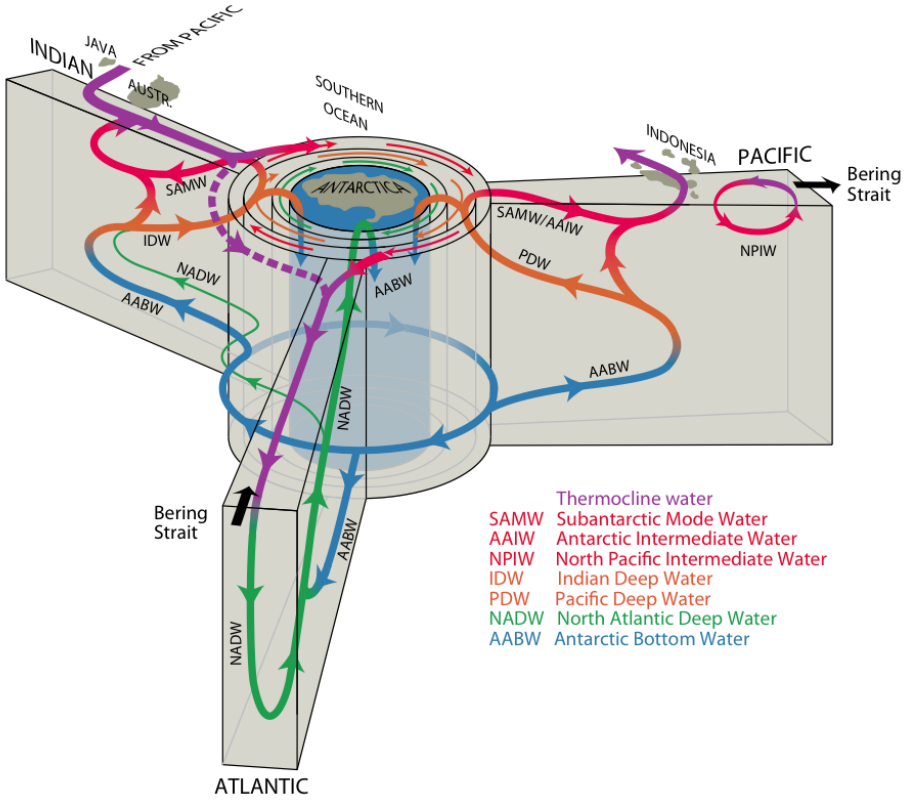

Figure 1.1: Schematic of the overturning circulation from a Southern Ocean perspective, revised from Talley et al. (2011), after Gordon (1986); Schmitz (1995); Lumpkin and Speer (2007). Talley (2013).

Dense waters are formed in a few regions at high latitudes and mass balance requires the conversion of these waters to less dense water masses. This can be achieved through diapycnal mixing where the downward diffusion of heat is balanced by the upward diapycnal advection of the overturning circulation Munk (1966). Recent work also suggests that the conversion of dense waters to less dense waters can be buoyancy- and wind-driven in the

Southern Ocean, where abyssal isopycnals outcrop at the surface (Nikurashin and Vallis, 2012). The quantitative contribution of either is unknown, yet we know that diapycnal mixing that results in the upwelling of tracers across isopycnals, at least partly closing the Southern Ocean meridional circulation (Huang, 1999). As such, the intensity and distribution of diapycnal mixing in the Southern Ocean plays a key role in the global overturning circulation (Polzin et al., 1997; Wunsch and Ferrari, 2004).

The main energy source for the ACC is the wind through wind work at the ocean surface (Wunsch, 1998) and variations in the wind forcing driving inertial fluxes (Alford, 2001; Watanabe and Hibiya, 2002). The sink for this energy is ocean turbulent mixing. Assuming uniform mixing, Munk (1966) used an advective and diffusive model of heat transfer to estimate that approximately $K_\rho = 10^{-4}\mathrm{m}^2\mathrm{s}^{-1}$ was required to close the global meridional overturning circulation. $K_\rho = 10^{-4}\mathrm{m}^2\mathrm{s}^{-1}$ became the canonical value for diapycnal diffusivity throughout the ocean interior.

Observations of diapycnal diffusivity in the thermocline waters, determined by tracer release (Ledwell et al., 1993, 1998) and microstructure studies (Gregg, 1987), sparked some controversy with values of diapycnal diffusivity of approximately 10^{-5} $\mathrm{m}^2\mathrm{s}^{-1}$: an order of magnitude lower than the canonical value. Recently, observational estimates of diapycnal diffusivity have shown diffusivity to be highly spatially non-uniform with values above rough topography two orders of magnitude larger than the canonical value (Polzin et al., 1997; Ledwell et al., 2000; St. Laurent et al., 2001; Naveira Garabato et al., 2004; Sloyan, 2005). Over smooth topography, diffusivity estimates are comparable to mid-latitude ocean interior values of $\mathrm{O}(10^{-5}\mathrm{m}^2\mathrm{s}^{-1})$. These observations question the assumption of uniform turbulent mixing. The significance of topography is of particular importance in the Southern Ocean because the stratification is weak compared to the global ocean and because the ACC is quasi-barotropic with strong currents extending to the sea floor. The enhanced diapycnal mixing rates observed over rough topography in the Southern Ocean have been attributed to the breaking of internal waves generated over rough topography (Ledwell et al., 2000; Nikurashin and Ferrari, 2010; Wu et al., 2011).

We are left with the questions: (1) Are there enough turbulent mixing hot spots ($K_\rho > 10^{-4}\mathrm{m}^2\mathrm{s}^{-1}$) in the ocean to account for the global averaged diffusivity ($K_\rho \approx 10^{-4}\mathrm{m}^2\mathrm{s}^{-1}$) required to close the meridional overturning circulation? (2) How much of the dynamics in the Southern Ocean are driven by eddy-mean flow interactions and how much by flow-topography interactions? (3) How do regional dynamics influence the magnitude and variability of mixing? (4) Is it the tides, large mesoscale eddies, fronts or a combination of all that interact with the rough topography to generate internal waves?

1.1.2 Estimating mixing

Turbulence in the ocean is the result of a downscale energy cascade that transfers energy and momentum from large scale currents towards smaller scale internal waves, mostly as a result of nonlinear internal wave-wave interactions (McComas and Muller, 1981). Diapycnal mixing can be estimated directly as an area average using tracer release experiments (Ledwell et al., 2011) or indirectly with microstructure profilers (measuring shear with an air-foil shear probe) (Gregg, 1987). Diapycnal mixing can also be indirectly estimated using finescale parameterization derived from empirical and theoretical relations based on finescale observations of the internal wave field characteristic shear and strain. The intensity of turbulent mixing is correlated to the energy and the shear of the local internal wave field (Polzin et al., 1995). Many variants of the finescale parameterization exist using observations of shear and strain, or either shear or strain only.

The uncertainties associated with these various finescale parameterization methods are typically $\pm 50\%$ (Polzin et al., 2002; Thorpe, 2005; Polzin et al., 2013). The method provides order of magnitude estimates of mixing as well as estimates of the spatial gradients of mixing.

1.2 The internal wave field

Oceanic internal waves are gravity waves that oscillate on density surfaces in the ocean interior as opposed to surface gravity waves that oscillate at

the surface of the ocean. The combination of gravity forces and the stratified ocean allows for internal waves to develop, propagate and disperse in the ocean. They radiate phase and energy, perpendicular to one another, both horizontally and vertically (St. Laurent et al., 2012b). Internal waves are the result of restoring gravity forces on water particles that have been displaced from equilibrium. Even very small variations in pressure gradients will generate internal inertial waves which propagate both horizontally and vertically, interacting with the mean flow.

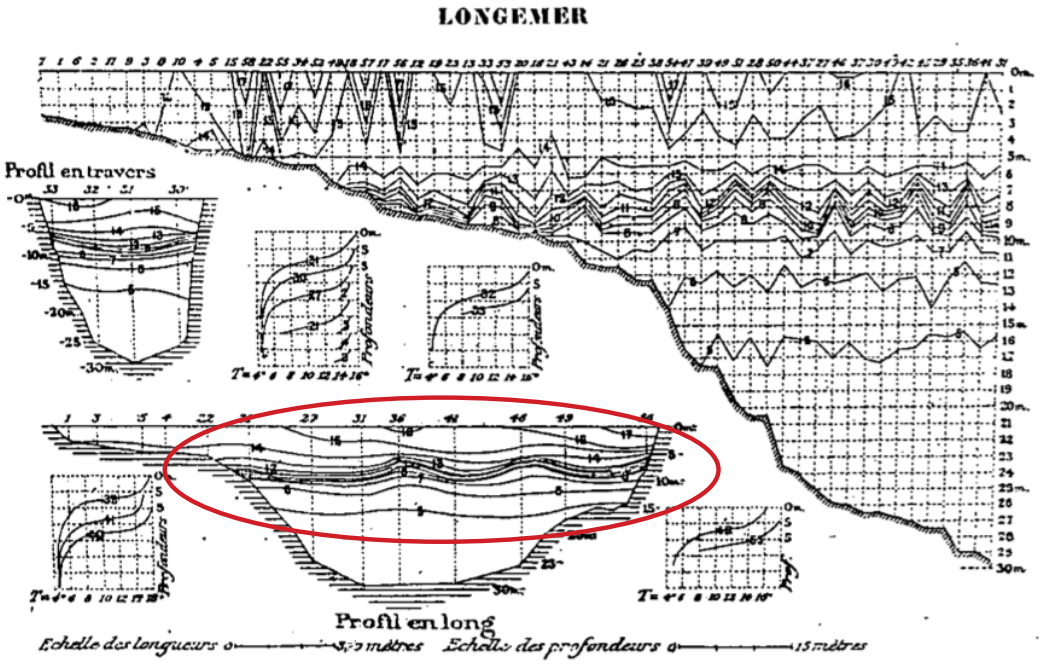

Figure 1.2: Temperature cross-lake profile ("Profil en travers") and along-lake profile ("Profil en long") of Lake Longemer . The along-lake temperature profile shows oscillations in the temperature contours along the length of the lake between 5 and 15 m depth (highlighted in red). (From Thoulet, 1894, Figure 8.).

The formation of waves at the interface of two liquids with different densities was reported by Benjamin Franklin in 1762. Stokes (1847) published a theory for these waves and Love (1891) formulated the equations for their propagation in a stratified fluid. Yet it was not until 1894 that Thoulet (1894) observed internal waves but did not recognise them as such in the Longemer

Lake, France (Figure 1.2). Nansen (1902) and Watson (1903) were the first to observe and identify internal waves in the Loch Ness.

1.2.1 Generation of internal waves

Internal waves in the ocean are mostly generated by tides and flows interacting with topography, and by the wind variability at inertial frequencies (Figure 1.3). Some internal waves are sufficiently non-linear to break immediately, enhancing diapycnal mixing locally, and some internal waves radiate away from their generation point, contributing to the background mixing of the ocean interior.

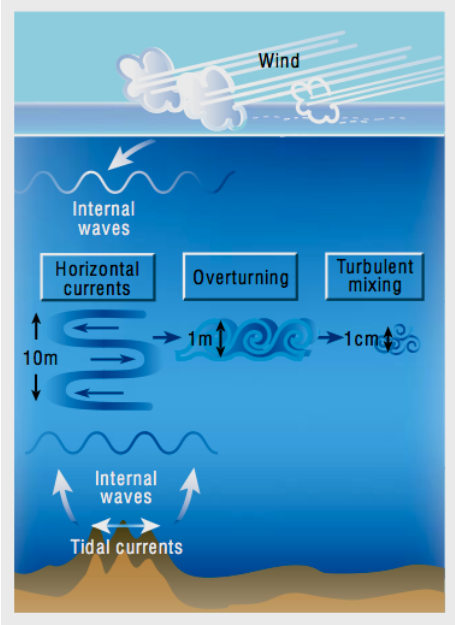

Figure 1.3: Internal wave generation and corresponding scales of ocean mixing. (From Garrett, 2003).

Non-linear interactions between the waves, also called "wave-wave" interactions, transfer the energy of the internal waves to other frequencies and wavenumbers. Ultimately, internal wave energy must dissipate as turbulent mixing.

One of the most important sources of kinetic energy in the ocean is the force exerted by the wind on the ocean surface, also called wind stress (τ_w)

(Wunsch and Ferrari, 2004). The global net transfer of kinetic energy from the wind to the ocean is estimated at 7 to 36 TW (Lueck and Reid, 1984; Wunsch and Ferrari, 2004), most of which is directly dissipated in the surface mixed layer. Some of this energy, 0.3 to 1.2 TW (Alford, 2001; Watanabe and Hibiya, 2002; Scott and Xu, 2009), is transferred into near-inertial motions that can propagate away from the ocean surface before breaking and generating mixing at depth (Pollard and Millard, 1970).

Rapid changes in wind stress induce near-inertial internal waves through the direct generation of internal waves at the surface, through the indirect generation of near-inertial waves at the mixed-layer interface, and through the indirect generation of internal waves by nonlinear interactions with surface gravity waves (Wunsch and Ferrari, 2004). Observations of energy propagation from near-inertial waves from the mixed-layer into the ocean interior suggest that wind generated inertial motions are an important part of the ocean mixing budget (Alford et al., 2012).

A second source of internal waves in the ocean is the interaction of currents with topographic features: internal waves are generated when stratified tidal flows and geostrophic currents flow over a topographic obstacle. Globally, the flow of the barotropic tide over topographic features (such as continental slopes, shelf breaks, sills, abyssal hills and seamounts) generates more internal waves than geostrophic currents: the estimate of the global tidal energy input into internal tidal waves is 1 TW, while the global energy conversion from geostrophic currents into internal waves is 0.2 TW (Nikurashin and Ferrari, 2013). In the Southern Ocean however, where there is the deep reaching Antarctic Circumpolar Current, the generation of internal waves by geostrophic currents rather than by tidal motions dominates (Nikurashin and Ferrari, 2013).

1.2.2 Garrett and Munk model

The observed local internal wave field is composed of many waves from various sources such as geostrophic flows, inertial oscillations and tides, locally generated or from the global internal wave continuum. In 1975, following

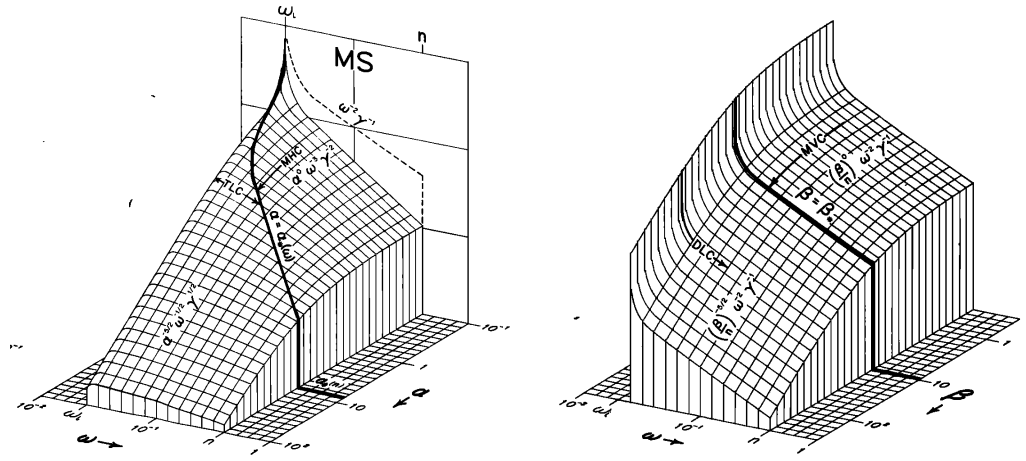

(a) (b)

Figure 1.4: The Garrett-Munk spectrum of internal waves in the ocean where the spectral energy is plotted vertically in logarithmic coordinates as a function of frequency and wavenumber.(a) The horizontal scales are frequency (ω) and the horizontal wavenumber (α). (b) The horizontal scales are frequency (ω) and the vertical wavenumber (β). The spectrum has a peak at the inertial frequency and the spectral energy decreases as both wavenumbers increase. (From Garrett and Munk, 1975).

their 1972 paper, Garrett and Munk were the first to describe and model the background oceanic internal wave field in terms of a vertical wavenumber and frequency spectrum using observations from Site 'D' in the western North Atlantic Ocean (39°20′ N, 70° W) (Garrett and Munk, 1972; Fofonoff, 1966).

The energy spectrum Garrett and Munk produced, which models the changes of wave energy in frequency, horizontal and vertical wavenumber space (Figure 1.4), is a good representation of the background state of the internal wave field for the North Atlantic, and has influenced global analysis of the internal wave field. However, in the past 20 years, the internal wave field has been found to vary considerably from the Garrett and Munk reference spectrum (D'Asaro and Morehead, 1991; Polzin and Lvov, 2011). At steady state, the rate at which internal waves break and dissipate energy into the wave field equals the rate of energy transfer from large scales to small

scales. By estimating the rate of energy transfer, the dissipation rate (ϵ) can be derived from internal wave properties.

1.2.3 Internal wave properties

Internal waves are characterised with vertical length scales from a few metres to one kilometre, horizontal length scales from a few metres to tens of kilometres, typical group velocities of $5\,\mathrm{cm\,s^{-1}}$, amplitudes from metres to tens of metres, and periods from several minutes to several hours (Thorpe, 2005; Kantha and Clayson, 2000, Chapter 6). They usually have lower frequencies and higher amplitudes than surface gravity waves due to reduced density differences (stratification) in the ocean interior relative to the density difference across the air-sea interface. Internal waves that are inertially forced at the ocean surface are expected to have intrinsic frequencies close to the local inertial frequency (f).

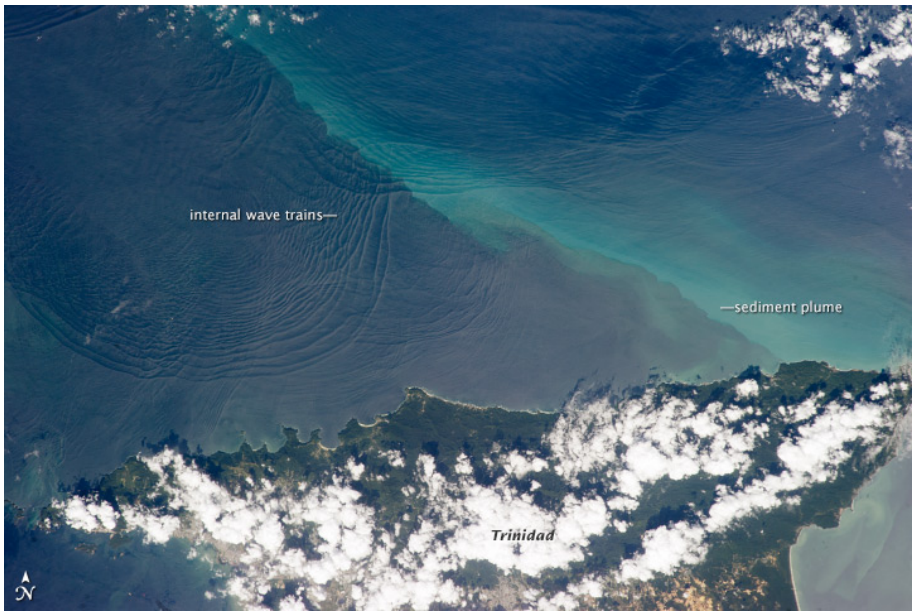

Figure 1.5: Photograph of sets of internal waves interacting near the shelf break off Tobago, north of the Caribbean island of Trinidad, taken from the International Space Station on the 18 January 2013. Also visible is a sediment plume traveling northwest with the Equatorial Current. (From NASA Earth Observatory.)

Direct observations of internal waves are not easily acquired and much of the available data come from continental shelves and other shallow regions, where the vertical displacement of the thermocline due to internal waves modulates the roughness of the ocean surface (Figure 1.5). Thus, the signature of internal waves can then be detected on images from synthetic aperture radars (SAR) and properties such as wavelength, direction of propagation and amplitude of the internal waves can be estimated (Zheng et al., 2002). Internal waves are best observed in echograms, acoustic backscattering and other sonar images, as well as time series of density, velocity or temperature variance. The properties of internal waves can be derived by applying spectral analysis to velocity observations of internal waves. A review of internal waves is provided in the June 2012 special issue of the journal *Oceanography* (St. Laurent et al., 2012b; Alford et al., 2012; Da Silva et al., 2012; Van Haren and Gostiaux, 2012).

1.3 Objectives and outline

Understanding the dynamics that maintain the deep ocean stratification is of fundamental importance to understanding the large-scale ocean circulation. Turbulent mixing plays a key role in maintaining deep ocean stratification. Direct measurements of mixing require specialised microstructure instruments and therefore are rare. However, finescale parameterization of mixing only require observations of velocity and density, making it possible to provide global order of magnitude estimates of mixing (Whalen et al., 2012). To develop accurate predictions of future climate under altered forcing conditions, we must know how internal waves driving the turbulent mixing are generated, propagate and interact with the ocean. This improved understanding will allow us to develop appropriate parameterization that can be included in climate models.

Here we first estimate the regional distribution and intensity of both the dissipation rate (ϵ) and diffusivity (K_ρ) at the northern edge of the Kerguelen Plateau in the Southern Ocean by applying two different finescale parameterization methods. Secondly, we analyse and describe the internal wave field

in the vicinity of the Kerguelen Plateau and link it to the mixing field. The Kerguelen Plateau, which is a volcanic ridge, is the largest plateau in the Southern Ocean and acts as an obstacle to the ACC. The flow of the ACC over this topographic feature should theoretically generate a dynamic local internal wave field and possibly an enhanced mixing field.

The objectives of this thesis are to:

(1) Estimate the intensity and distribution of turbulent mixing in the vicinity of the Kerguelen Plateau using EM-APEX profiling floats, an innovative Lagrangian observing platform.

(2) Investigate the impact of the interaction of the ACC and topography, the wind forcing and eddy structure on magnitude and distribution of turbulent mixing.

(3) Analyse and describe the internal wave field north of the Kerguelen Plateau.

The thesis is divided into seven chapters. This first chapter, introduces the concept of mixing and the internal wave field. Chapter 2 describes the instruments and data used in this study, and Chapter 3 describes the physical oceanography of the region. The theory and application of Thorpe-scales and shear-strain parameterizations of dissipation and mixing are presented in Chapter 4. Analysis of the mixing intensity, distribution and sources are presented in Chapter 5. The internal wave field in the vicinity of the Kerguelen Plateau is analysed and described in Chapter 6. Finally, the main findings, implications of this research and suggestions for future work are provided in Chapter 7.

Chapter 2

INSTRUMENTS AND DATA

2.1 EM-APEX floats

The core of the data (temperature, salinity and velocity profiles) used for this study are *in situ* ocean measurements from eight Electromagnetic Autonomous Profiling Explorer (EM-APEX) floats. The EM-APEX is an innovative instrument that provides relatively inexpensive, autonomous, high-resolution observations of velocity. The floats were deployed during the RRS James Cook cruise JC029 in late 2008 as part of the Southern Ocean FINEstructure (SOFine) project. The SOFine project is a U.K., U.S. and Australian collaborative experiment to investigate the impact of finescale processes on the momentum balance in the Antarctic Circumpolar Current (Naveira Garabato, 2009).

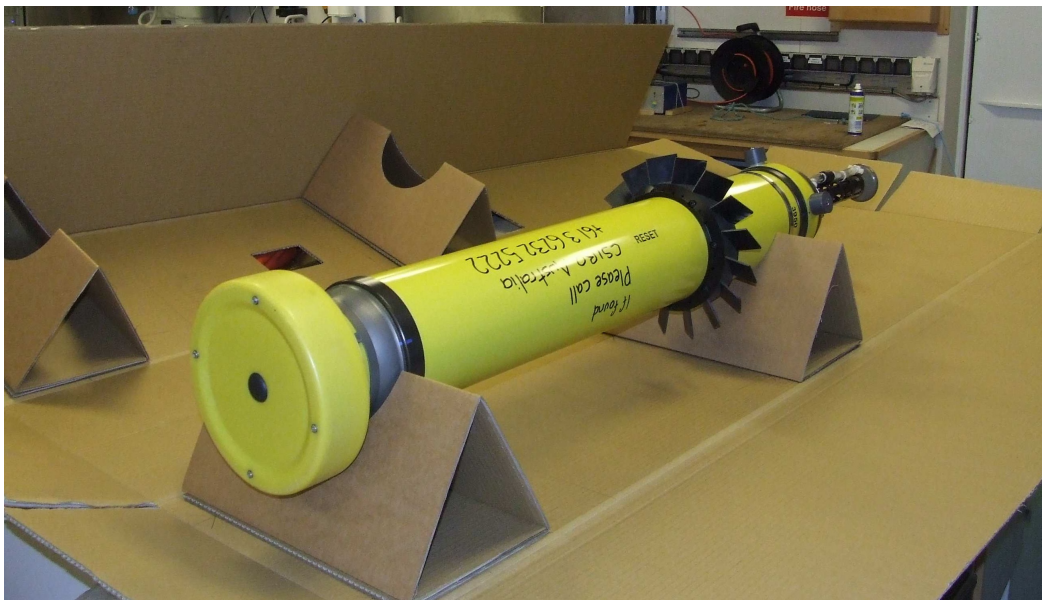

Figure 2.1: EM-APEX float prior to deployment in the wet lab onboard RRS James Cook. The cardboard box is used to protect the float during the deployment procedure. Two characteristics specific to the EM-APEX float are the black fins allowing it to rotate as it sinks in the water column and the grey electrodes close to the top of the float.

2.1.1 Float characteristics

The EM-APEX profiling float (Figure 2.1) is a recent addition to the array of autonomous profiling instruments and measures vertical profiles of temperature, salinity and horizontal velocity. EM-APEX floats are the result of a collaboration between the University of Washington Applied Physics Laboratory (APL-UW) and Teledyne Webb Research Corporation (WRC). The float combines a standard Teledyne APEX float with an electromagnetic subsystem. The main technical characteristics of the EM-APEX are described below.

SBE-41 CTD

On the EM-APEX float, temperature (T), salinity (S) and pressure (P) are measured by a Sea Bird Electronics SBE-41 CTD. The float rate of descent and ascent has a range of 0.10 to 0.12 $\mathrm{m\,s^{-1}}$. The CTD is pumped on demand for approximately 2.5 s, delivering 40 $\mathrm{ml\,s^{-1}}$ flow. The CTD sensor accuracy provided by the manufacturer is 2 dbar for pressure, 2×10^{-3} °C for temperature, and 2×10^{-3} for conductivity. The CTD data were processed in 2.2 m vertical bins for preliminary work and then in 3 m vertical bins when deriving mixing estimates to match the electro-magnetic subsystem data vertical resolution (see below).

EM-APEX electromagnetic subsystem

The EM-APEX electromagnetic subsystem has a compass, accelerometer and five electrodes to estimate the magnitude of horizontal currents (Figure 2.2). The horizontal velocity is estimated using the principle that a conductor moving through a magnetic field develops an electrical potential drop across the conductor. In this application, the conductor is seawater and the magnetic field is that of the Earth's (Sanford et al., 2005). The EM-APEX electromagnetic subsystem voltmeter measures this electric potential difference across the body of the float with electrodes.

The float rotates with a period of 12 s due to external fins and the motionally-induced electric field is sampled at 20 Hz and then averaged with

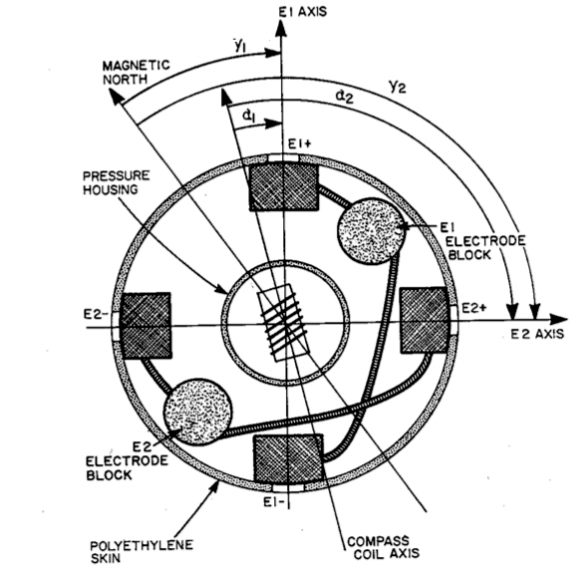

Figure 2.2: Cross-section of the EM-APEX electromagnetic subsystem at the level of the electrodes showing the arrangement and the orientation of the electrodes (Sanford et al., 1978) p191.

a sinusoidal fit. The fit is made over 50 s long segments of data with 25 s between successive fits, acting as a low-pass filter (Sanford et al., 2011). The fits provide an estimate of the horizontal current and the residuals provide an estimate of the velocity noise level. Measured voltages are transmitted over the Iridium global phone system and the processing of the voltages into eastward and northward velocity components is shore-based. The velocity profiles are relative to a depth-independent offset. Given the GPS positions, by pairing profiles, we can determine the absolute velocity profile (see Section 2.2.2) at approximately 3 m vertical resolution. Profiles were gridded into 3 m vertical bins for the mixing analysis.

2.1.2 Deployment strategy

Eight EM-APEX floats were deployed on the northern edge of the Kerguelen Plateau in late 2008 to drift along the Antarctic Circumpolar Current (ACC) (Figure 2.3).

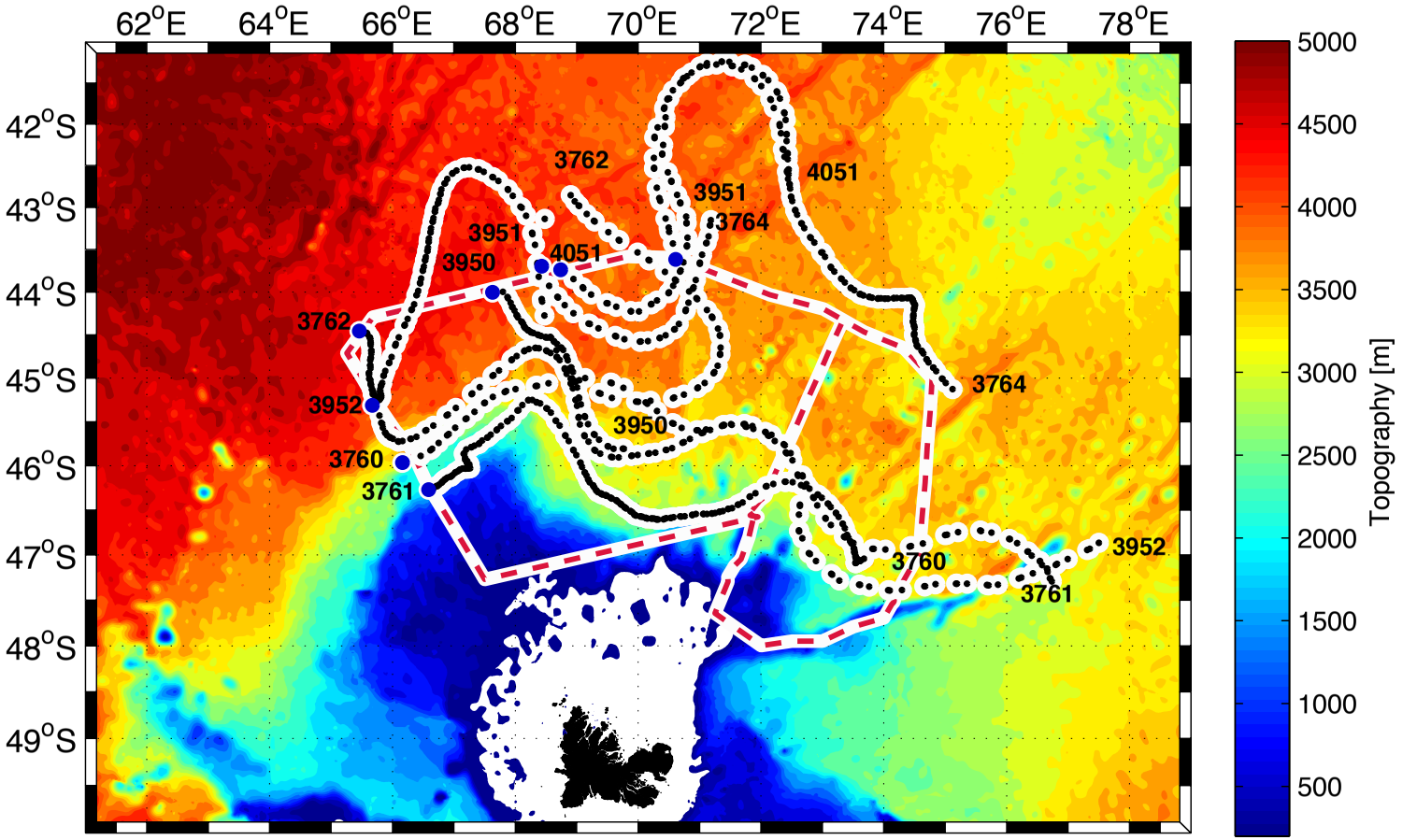

Figure 2.3: EM-APEX float trajectories overlying topography in colour scale ranging from 200 to 5000 m at 200 m increments. Each black dot denotes a float profile surface location and the deployment location is highlighted by a bigger blue dot. The float numbers are indicated at the first and last profile of each float. There are 914 profiles, sampled between the 18^{th} November 2008 and 30^{th} January 2009. Also shown is the voyage track of RRS James Cook JC029 (dash red line).

While drifting north of the Kerguelen Plateau, the floats were programmed to surface twice a day, measuring four profiles of temperature, salinity, pressure and horizontal velocity from the sea surface to 1600 m (Figure 2.4). The floats spent typically 30 minutes at the surface to transmit the profile data over the Iridium satellite network as opposed to floats transmitting over the Argos communication system spending on average 10 hours at the surface. Using the Iridium communication system allows for two way communication as well as faster data transfer and therefore the option to sample at higher resolution. The floats only sampled the top 1600 m of the water column rather than going to their maximum 2000 m so that consecutive up profiles are approximately half an inertial period apart (17 hours at 45° S latitude), and the inertial frequency can be resolved in the data.

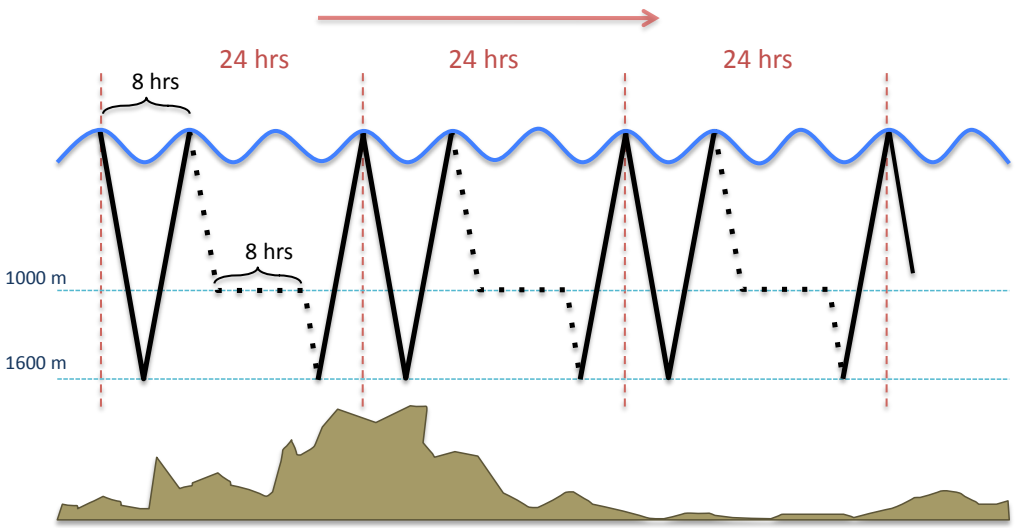

Figure 2.4: EM-APEX float vertical sampling strategy. The black line denotes the path of the float in the water column. The dotted line refers to profiles not used in this study.

In the Southern Ocean, dynamic height can be used as a proxy for front and water mass positions (Sokolov and Rintoul, 2009a). The EM-APEX floats were deployed using dynamic height as a criterion so as to cover as wide a dynamic height range as possible and to be likely to sample evenly the full width of the ACC. This was achieved by working with near real-

Float	Date UTC	Time UTC	Dynamic Height	Latitude	Longitude	Depth	CTD Station
3670	18/11/2008	02:02	0.87	46^o 16.85'S	66^o 37.82'E	1766	17
3761	18/11/2008	11:50	0.99	45^o 42.71'S	66^o 22.71'E	2438	None
3952	20/11/2008	06:08	1.13	45^o 01.66'S	65^o 46.00'E	4625	22
3762	21/11/2008	07:26	1.09	44^o 16.67'S	65^o 31.92'E	4383	None
3950	23/11/2008	15:44	1.08	43^o 53.87'S	67^o 45.40'E	4287	28
3951	24/11/2008	03:38	1.32	43^o 51.97'S	68^o 26.65'E	4031	29
4051	24/11/2008	12:18	1.50	43^o 54.80'S	68^o 49.97'E	3712	None
3764	25/11/2008	11:44	1.53	43^o 54.80'S	70^o 35.54'E	4037	32

Table 2.1: EM-APEX float deployments details: float hull number, date, time, dynamic height [m], latitude, longitude, depth [m] and associated station number. Cruise JC029 (RRS James Cook) November 2008.

time sea surface height anomaly fields that allowed us to track the locations of the ACC jets and fronts during the voyage. The cruise track with the deployment positions of the floats is shown in Figure 2.3 and deployment details are summarized in Table 2.1. Five of the eight EM-APEX floats were deployed at a CTD station, allowing calibration of the float salinity sensor with the CTD salinity observations.

The data transmitted by the floats over the Iridium phone system were received by a data server at the University of Tasmania and converted to relative velocity using software developed by John Dunlap at the University of Washington in the research group of Prof. Tom Sanford. This was followed by extensive processing by Dr. Helen Phillips to calibrate the instruments, automate the quality control of the velocity data, and to convert relative velocity to absolute velocity.

2.2 Data quality control

The EM-APEX floats provide vertical profiles of temperature, salinity, pressure and relative horizontal velocity for the upper 1600 m of the ocean. Unlike ship-based observations, it is difficult to monitor the condition of the sensors of the EM-APEX floats once they have been deployed. A thorough quality control of the data is crucial to ensure data reliability.

2.2.1 Quality control of the CTD data

We applied the standard CMAR (CSIRO Marine and Atmospheric Research) Argo Delayed-mode quality control (DMQC) to the eight EM-APEX floats. The DMQC applies a rigorous and internationally standardised quality control procedure to ensure that the temperature and salinity profiles are free of detectable errors and biases. The software had to be adapted in some places to fit the sampling strategy and data format of the EM-APEX floats, which are different to those of standard Argo program profiling floats. The CMAR DMQC procedure is based on visual checks for bad data points, biases and trends as well as comparisons of the data with local CTD profiles and with the Argo profiles data base. Below we describe each step of the DMQC procedure and Table 2.2 summarises the quality control findings for all eight floats. As an example, the complete DMQC procedure for float 3760 is described in Appendix B: Australian Argo Delayed Mode Quality Control (DMQC) Processing a complete example.

Identify bad pressure points

We visually check each profile for bad pressure points in particular at the bottom of each profile where the float sometimes overshoots its turning depth. Bad pressure points are flagged as bad data. Data points flagged as bad for one variable such as pressure are also flagged across other variables. For here and below, more details and figures that illustrate the procedure that we applied are shown in Appendix B.

Check for density inversions

Density inversions are identified based on a density difference criterion of $0.004\,\mathrm{kg\ m^{-3}}$ based on Argo DMQC processing standards. Each density, temperature and salinity profile is then plotted for visual inspection and suspicious inversions are flagged (see Figure B.4 in Appendix). Spurious density inversions are often the result of a bad salinity reading due to some foreign particle affecting the sensor's reading. Only density inversions due to spurious temperature, salinity or pressure data are flagged as bad.

Identify bad data points

We check visually a range of diagnostic plots to identify and eliminate various bad data points. These diagnostic plots include individual T-S plots for each float where obvious outliers, spikes and "salt hooks" can be identified. Salt hooks are sometimes observed at the base of the profiles, where the deepest salinity measurements are too high with respect to above samples, looking like a hook in the data. This happens as the float slows down at the bottom of a profile when water with a higher salinity from a shallower depth stays in the sensor cell and is not flushed out completely. A comparison with nearby Argo floats in potential temperature-salinity space is also performed to identify outliers.

Check for surface pressure drift

We check for a surface pressure drift by analysing the reported surface value which should be constant. If a cumulative drift in the surface value is observed, a correction is applied.

Apply thermal lag correction

A thermal lag correction is applied to the salinity data using parameters ($\alpha = 0.023$ and $\tau = 25.0s$) that are estimated for this particular data set (see Section 2.2.3). We apply the method of Johnson et al. (2007), which is valid for a fall rate between 0.06 and 0.12 $\mathrm{m\,s^{-1}}$.

Float number	Number of profiles	Number of bad data points identified	Surface pressure drift detected	Thermal lag correction applied	Salinity drift detected
3760	211	9	none	✓	none
3761	88	4	none	✓	none
3952	131	3	✓	✓	none
3762	184	6	none	✓	none
3950	58	none	none	✓	none
3951	36	4	none	✓	none
4051	65	none	none	✓	none
3764	141	none	none	✓	none

Table 2.2: DMQC results for the eight EM-APEX floats.

Check for salinity drift

We apply a visual check for a salinity drift using profiles from three different climatologies: Gouretski and Koltermann, CARS2006 (precursor to CARS2009, based on WOD2001 that covers globally to 24°N and only to 10°N in the Atlantic) and CARS2009 (CSIRO Atlas of Regional Seas 2009: global ocean property climatology based on historical profile data from the World Ocean Database WOD05, July 2008 update with locally surface pressure corrected and screened Argo data to May 2009) developed by Ridgway et al. (2002). This check also uses nearby Argo float data to compare the observed salinity with nearby Argo salinity fields. If a sensor drift is identified, a salinity drift correction is applied.

Check for data points outside set ranges

This script will report if values are outside location specific and strict range checking envelopes. We then take the decision whether or not those values are bad data points that need to be removed or extreme values that can be kept.

2.2.2 Quality control of the velocity data

The quality control of the horizontal relative and absolute velocity data was defined and implemented by Dr. Helen Phillips at University of Tasmania (UTAS) (Phillips and Bindoff, 2014). We provide a description of the procedure that was applied. EM-APEX floats measure the electrical potential difference across their body with reference to the local magnetic field. Each float has two independent pairs of electrodes that provide two vector profiles of electrical potential difference. The actual sampling rate of the float is 1 Hz, but the on-board processing of the raw data (least-squares fit over a 50 points window, overlapping the neighbouring window by 25 points) results in one voltage component pair for each channel every 3 to 5 m. The on-board processing also provides an associated root-mean-square error to the fit for each channel. From the voltages, velocity components relative to a depth-independant offset are calculated using Sanford (1971).

Removing outliers

The first check flags velocities with magnitude larger than $2\,\mathrm{m\,s^{-1}}$ and velocities with RMS error larger than a depth dependent value (Table 2.3). If more than 50 data points fail these checks or if the number of points in the profile is less than 100, then the entire profile is flagged as bad data. The threshold values (Table 2.3) were determined from a statistical analysis of the magnitude of the velocity error at each depth and through visual examination of each velocity and root mean square (RMS) error profile. Note that close to the surface, much of the RMS error is due to surface wave activity.

Correcting the compass orientation

The angle between the electrode axes and the compass orientation is determined mechanically during the construction of the float. The estimates of the horizontal velocity are very sensitive to the value of this angle and an error in the angle of the order of 1° can result in a velocity error of the order of $1\,\mathrm{cm\,s^{-1}}$ (Sanford et al., 1974). By modifying the angle estimate to minimize the offset between velocity on consecutive down and up profiles

Pressure range PR [m]	Threshold RMS error value [$\mathrm{m\,s^{-1}}$]
$PR < 100$	none
$100 \leqslant PR < 220$	0.015
$220 \leqslant PR < 900$	0.008
$PR \geqslant 900$	0.005

Table 2.3: Depth dependent RMS error thresholds.

close to the maximum pressure of the profiles, we obtain a precise value of the angle. The minimization is done for each down-up profile pair and the resulting time series of angles is averaged, providing one angle per channel, per instrument. The relative velocities are then re-calculated with the new angle.

Deriving the absolute horizontal velocity

The difference between the absolute (u, v) and the relative (u_{rel}, v_{rel}) velocities is a depth-independent offset (u_b, v_b), which is equal to the depth-averaged absolute velocity from the surface to the sea floor.

$$\begin{aligned} u &= u_{rel} + u_b \\ v &= v_{rel} + v_b \end{aligned} \tag{2.1}$$

Determining the offset requires an independent measure of the float velocity, obtained from the float surfacing GPS positions (Phillips and Bindoff, 2014).

We define the surface position of the float at t_1 (start of a descending profile) as (x_1, y_1) and the surface position of the float at t_2 (end of the next ascending profile) as (x_2, y_2). The horizontal distance between the two surface positions is the absolute displacement $(\triangle x, \triangle y)$, which can be estimated using the Global Positioning System (GPS) or satellite positioning of the float.

$$\triangle x = x_2 - x_1$$

$$\triangle y = y_2 - y_1 \tag{2.2}$$

Next we define the relative displacement $(\delta x_{rel}, \delta y_{rel})$ as the horizontal displacement between t_1 and t_2 due to the relative velocity along the subsurface path of the float

$$\delta x_{rel} = \int_{t_1}^{t_2} u_{rel} dt$$

and

$$\delta y_{rel} = \int_{t_1}^{t_2} v_{rel} dt. \tag{2.3}$$

The absolute displacement of the float is

$$\triangle x = \delta x_{rel} + \delta x_b$$

and

$$\triangle y = \delta y_{rel} + \delta y_b, \tag{2.4}$$

where $(\delta x_b, \delta y_b)$ is the displacement due to the depth independent offset. Combining (2.2) with (2.3) and (2.4), we have an estimate of the displacement due to the depth independent offset

$$\delta x_b = (x_2 - x_1) - \int_{t_1}^{t_2} u_{rel} dt$$

and

$$\delta y_b = (y_2 - y_1) - \int_{t_1}^{t_2} v_{rel} dt, \tag{2.5}$$

from which we can deduce the velocity offset

$$u_b = \frac{\delta x_b}{\triangle t}$$

and

$$v_b = \frac{\delta y_b}{\triangle t}, \tag{2.6}$$

and so, combining (2.1) with (2.5) and (2.6), we have

$$u = u_{rel} + \frac{(x_2 - x_1) - \int_{t_1}^{t_2} u_{rel} dt}{\triangle t}$$

and

$$v = v_{rel} + \frac{(y_2 - y_1) - \int_{t_1}^{t_2} v_{rel} dt}{\triangle t}, \tag{2.7}$$

where $\triangle t = t_2 - t_1$.

2.2.3 Thermal lag correction

Salinity is estimated using measurements of seawater conductivity, which is mostly dependent on seawater temperature, significantly less on salt ions and weakly dependent on pressure. Salinity can be derived from measurements of pressure, temperature and conductivity. The accuracy of the salinity measurements will depend on the matching of the temperature and conductivity sensors response times. The signal of the conductivity sensor in a CTD depends on three factors: the flushing of the inside of the sensor, the boundary layer of the fluid against the wall of the sensor and the heat stored in the wall of the sensor (Lueck and Picklo, 1990). The first two factors are "short-term" while the heat stored in the sensor (sensor's thermal inertia) induces a "long-term" response. This long-term response, hereafter referred to as "Thermal lag error", is about one order of magnitude larger than both short-term responses. Correcting for this long-term response is particularly important for data that are going to be used to estimate ocean mixing since estimating mixing requires highly precise density estiamtes.

Thermal lag error

The Sea Bird conductivity sensor is mostly composed of glass, which has a high thermal inertia. The heat stored in the glass walls of the sensor takes a few tens of seconds to diffuse through the water inside the sensor, changing the temperature of the water being sampled. This leads to an incorrect estimate of conductivity and thus salinity, with characteristic thermal-lag

timescale error of tens of seconds. The thermal lag error is highest in large in-situ temperature gradients. During a downcast, for example, the sensor travels from warmer waters to colder waters (Figure 2.5). As the instruments descends, the heat stored in the conductivity sensor warms entering water, raising the conductivity measurement and therefore the salinity reading. Similarly, on an upcast, the sensor is moving from colder to warmer water, lowering the conductivity and salinity measurements. A pumped instrument will minimize this error but not eliminate it.

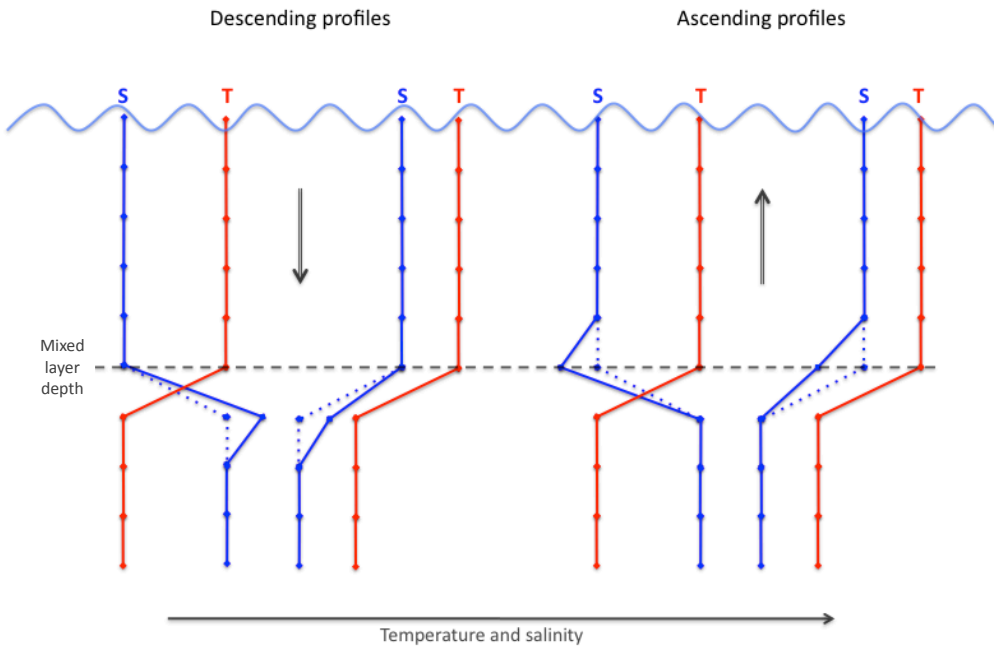

Figure 2.5: Theoretical example of temperature and salinity profiles for descending (left) and ascending (right) profiles. The solid lines show observed values that include the thermal lag effect; dashed lines show the theoretical or thermal lag corrected data.

Correction method

The thermal lag correction involves deriving a "corrected" temperature of the seawater in the conductivity sensor and then re-calculating salinity. This

is done applying a discrete time domain, recursive filter scheme with two parameters: α, which describes the initial amplitude of the conductivity error and τ, which describes the time constant of the conductivity error (Morison et al., 1994). The temperature correction (T_c) at sample index (n) is subtracted from the measured temperature to estimate the corrected temperature in the conductivity sensor

$$T_c(n) = -bT_c(n-1) + a\left[T(n+1) - T(n)\right], \tag{2.8}$$

where T is the measured temperature and

$$a = 4f_n\alpha\tau(1 + 4f_n\tau)^{-1} \qquad b = 1 - 2a\alpha^{-1}.$$

Here we follow the method used by Johnson et al. (2007) on SBE-41 CTDs to estimate α and τ. We expect a spike in salinity at the transition between the bottom of the mixed-layer and the ocean interior due to the thermal lag effect (Figure 2.5). A thermal lag signature will be more easily identified for profiles with a well-defined surface thermal mixed-layer and a large vertical temperature gradient. When an ascending float goes from cooler to warmer waters, the deepest measured data point of the thermal mixed-layer typically shows a low salinity spike when compared to the points above (Figure 2.5). We identify all profiles with a well-defined surface thermal mixed-layer and a large vertical temperature gradient and apply the thermal lag correction with a range of values for α and τ.

We then search for the α and τ combination that minimizes the difference between the mean thermal lag corrected potential density of the bottom two points of the thermal mixed-layer and the mean uncorrected potential density in the rest of the thermal mixed-layer. The bottom of the mixed-layer is defined as the depth where $dT/dz > 0.0005°\mathrm{C\,m^{-1}}$. The mean uncorrected potential density is calculated in the mixed-layer from 20 data points below the surface down to 60 data points above the mixed-layer. When the thermal lag correction parameters are accurate, the mixed-layer profile is close to being statically stable (Figure 2.6).

We identify 27 profiles with well-defined surface thermal mixed-layers

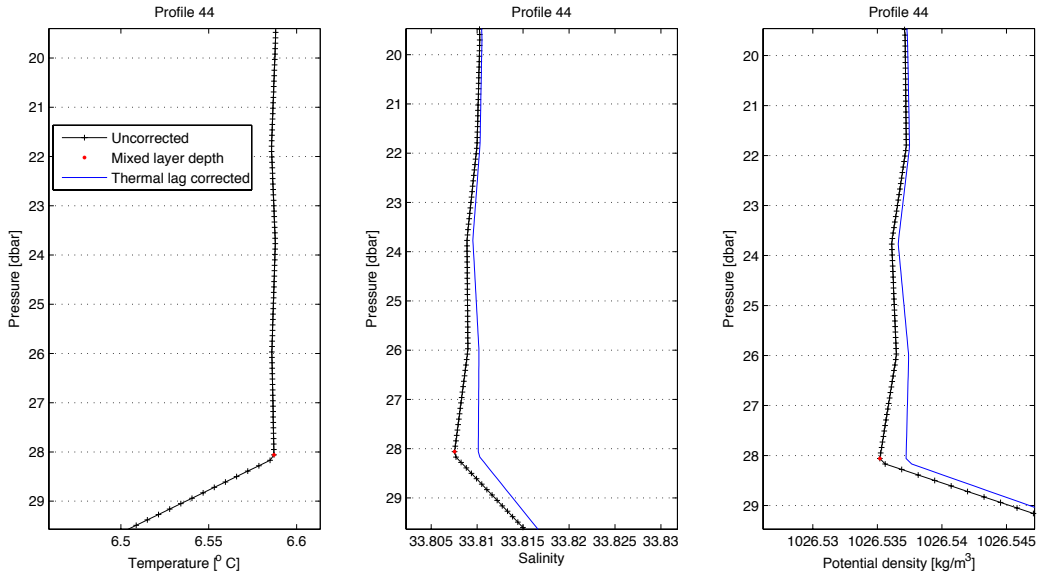

(a) Profile 44 of float 3761

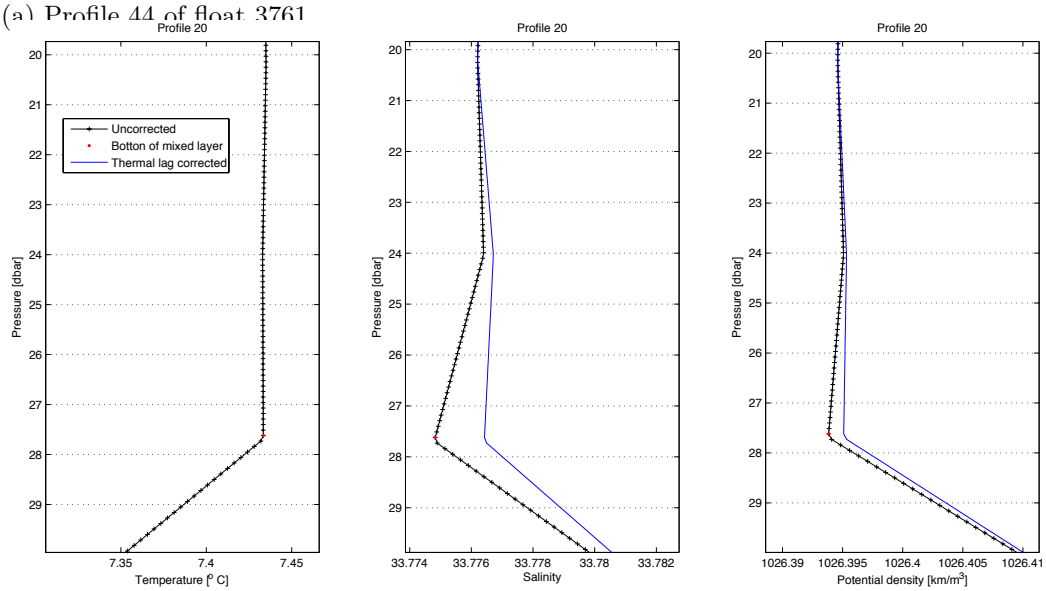

(b) Profile 20 of float 3762.

Figure 2.6: Temperature, salinity and potential density profiles of (a) profile 44 from float 3761and (b) profile 20 from float 3762 where black denotes raw data and blue denotes thermally corrected data. The corrected salinity was derived using median thermal lag correction coefficients $\alpha = 0.023$ and $\tau = 25$ s.

Reference	**CTD**	α	τ [s]	$\alpha * \tau$	α IS	τ IS
Lueck and Picklo (1990)	SBE-4-01	0.028	9	0.25	N/A	N/A
Morison et al. (1994)	SBE-9	0.0245	9.5	0.23	N/A	N/A
Pinot et al. (1997)	SBE-25	0.03	14	0.42	N/A	N/A
Johnson et al. (2007) NOAA floats	SBE-41	0.023	20	0.46	0.019	24
Johnson et al. (2007) UW floats	SBE-41	0.028	16	0.45	0.011	32
This study EM-APEX floats	SBE-41	0.023	25	0.60	0.031	23

Table 2.4: Weighted median values and interquartile spreads (IS) of sensor response corrections for SBE-41 CTDs.

and large vertical temperature gradients at the bottom of the mixed-layer by applying a careful screening on ascending profiles. The temperature and salinity data are interpolated onto a uniform 1 Hz grid to work in temporal gradients rather than vertical spatial gradients. For each profile we identified the best α and τ combination that minimizes the difference between the mean thermal lag corrected potential density of the bottom of the thermal mixed-layer and the mean uncorrected potential density in the rest of the thermal mixed-layer (Figure 2.7).

Thermal lag parameters

The median value of τ is 25 s with an interquartile spread of 23 s. The median value of α is 0.023 with an interquartile spread of 0.031 and the product of the median α and τ is 0.60 (Table 2.4). These values are very close to the values Johnson et al. (2007) derived for the National Oceanic and Atmospheric Administration/Pacific Marine Environmental Laboratory (NOAA/PMEL) and University of Washington (UW) floats (Table 2.4). The fact that the original 1 Hz CTD data from the EM-APEX floats were not accessible makes

correcting for thermal lag difficult. However, it is encouraging that the thermal lag correction coefficients for the same CTD but different float types are very similar. The thermal lag correction is described in Section 2.2.1.

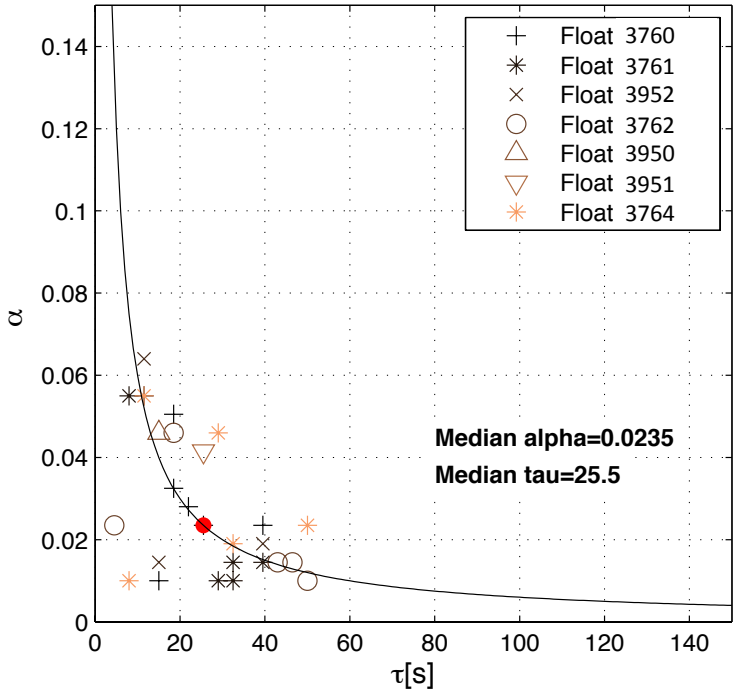

Figure 2.7: Values of thermal lag correction parameters α and τ for selected profiles from EM-APEX floats with SBE-41 CTD (3760, 3761, 3952, 3762, 3950, 3951, and 3764). The median value (red circle) and the curve for constant median value of $\alpha \times \tau$ (thin black line) are displayed.

2.3 Other data sets

2.3.1 Topography data

We use version 13.1 of the Smith and Sandwell topography data (Smith and Sandwell, 1997) [1]. This data set has a resolution of one minute and is derived from shipboard depth soundings and from satellite altimetry. The observed

[1] http://topex.ucsd.edu/cgi-bin/get-data.cgi

ocean depth data were obtained by screening surveys from the National Geophysical Data Centre, the Scripps Institution of Oceanography and Lamont-Doherty Earth Observatory databanks, and other data. The satellite gravity field combines all data from the European Remote Sensing satellite (ERS-1) and GEOdetic SATellite (GEOSAT) satellites. We subsample the data set to obtain the area between 50°E to 90°E and 55°S to 30°S.

2.3.2 Wind data

We use blended satellite derived wind data provided by European Remote Sensing Satellite Processing and Archiving Facility (CERSAT) at the French Research Institute for Exploitation of the Sea (IFREMER) [2]. The wind observations are derived from near real-time measurements by a scatterometer onboard the Quick Scatterometer (QuikSCAT) satellite and by three Special Sensor Microwave Imager (SSM/I) instruments onboard Defense Meteorological Satellite Program (DMSP) satellites F13, F14 and F15[3]. The wind data, which consist of wind speed [$\mathrm{m\,s^{-1}}$] and wind stress [$\mathrm{N\,m^{-2}}$], are provided 6-hourly at $0.25^\circ \times 0.25^\circ$ resolution over the global ocean, excluding sea ice areas. For each of the 914 EM-APEX profiles, we identify the closest wind data points within 24 hours of the profile being sampled and within a radius of 0.5° around the location of the profile. For each profile, an average value of the wind speed and stress is then computed within those time and space scales.

[2] ftp://ftp.ifremer.fr/ifremer/cersat/products/gridded/mwf-blended/data/6-hourly/

[3] ftp://ftp.ifremer.fr/ifremer/cersat/products/gridded/mwf-blended/documentation/BlendedWind-Doc_27112006.pdf

Chapter 3

REGIONAL OCEANOGRAPHY

In this Chapter, data collected by the EM-APEX floats is used to explore the characteristics of the temperature, salinity and horizontal velocity fields in the Kerguelen Plateau region. Hydrographic fronts and water masses are identified and vertical stratification is discussed.

The 914 profiles from the EM-APEX floats stretch over 6500 km of float trajectories in the vicinity of the Kerguelen Plateau ($41°S - 50°S$ and $61°E - 79°E$), sampling the upper water column (0 to 1600 m) between November 2008 and February 2009 (Figure 3.1). Further profiles were obtained downstream but will not be analysed in this study.

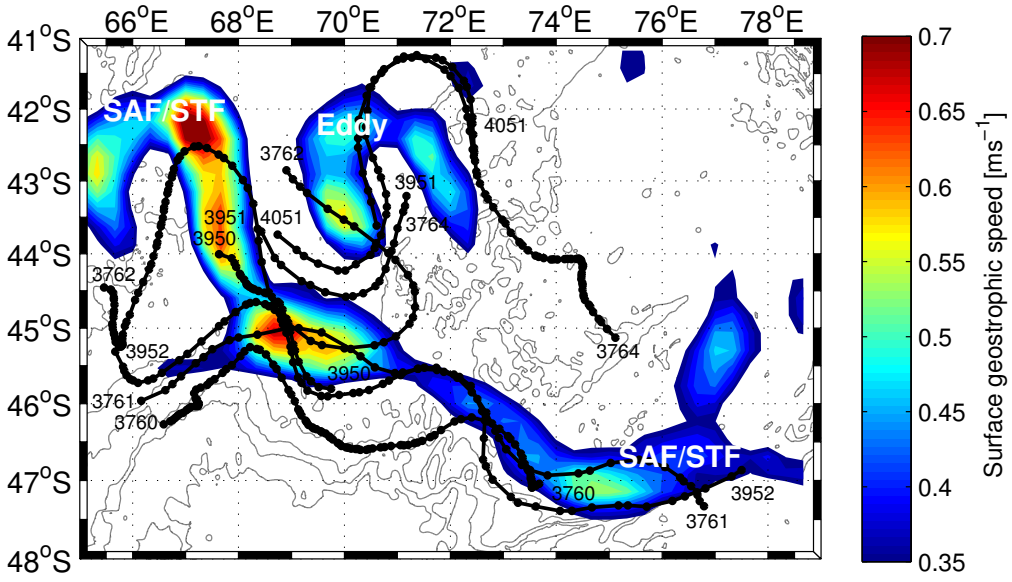

Figure 3.1: Trajectories of the EM-APEX floats (black) over the sampling period mean surface geostrophic speed from combined altimetry and ocean climatology (see text)(colour scale) and topography contours (grey). To identify jet flows, mean surface geostrophic speeds below 0.35 m s^{-1} are ignored. Topography contours range from 500 to 5000 m at 800 m intervals. The main jet is identified as the Subantarctic Front and Subtropical Front combined.

The surface geostrophic speed is derived using a weekly geostrophic velocity product (satGEM) from combined hydrographic data (GEM field) and satellite altimetry data (AVISO) (Meijers et al., 2011). The satGEM weekly geostrophic velocities are averaged over a density range (26.6 to 26.8 kg m^{-3}) and over the sampling period (18/11/2008-30/01/2009), resulting in a mean

velocity field with a horizontal resolution of 1/3°.

The EM-APEX overall mean potential temperature is 4.65 °C, the mean salinity is 34.45, the mean potential density is 27.24 kg m^{-3}, the mean buoyancy frequency squared is 8.6×10^{-6} rad^2 s^{-2} and the mean current speed is 0.29 m s^{-1} (Figure 3.2).

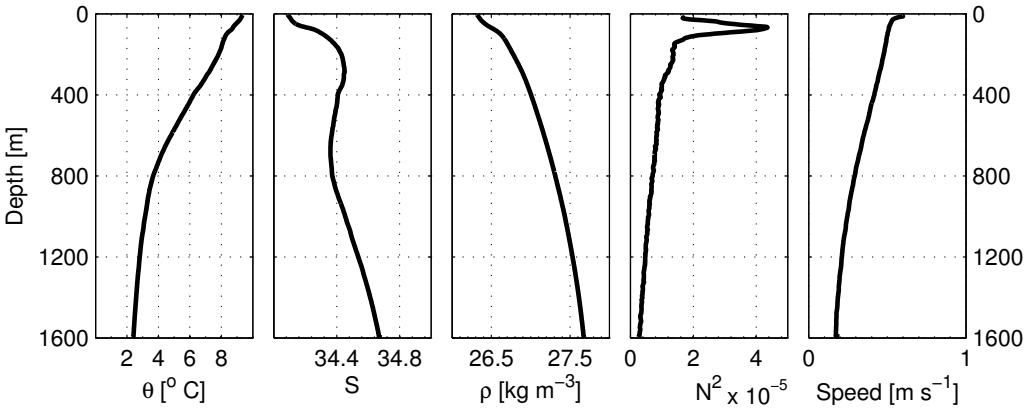

Figure 3.2: Mean EM-APEX vertical profiles as a function of depth of potential temperature (θ), salinity (S), potential density (ρ_θ), stratification (N^2) and speed.

3.1 Hydrographic fronts

Fronts can be identified using hydrographic criteria such as velocity maxima (jet) location, water mass distribution, and locations where certain hydrographic properties cross particular depths (Belkin and Gordon, 1996). In the Kerguelen region sampled by the EM-APEX floats, we can expect the southern branch of Subtropical Front (STF), the Subantarctic Front (SAF) and possibly the Polar Front (PF) to have crossed the area (Sokolov and Rintoul, 2009a,b).

Traditionally, the STF is identified by temperature and salinity ranges of 10 to 12 °C and salinities on the practical salinity scale pss-78 of 34.6 to 35.0 at 100 m depth respectively (Orsi et al., 1995). The SAF is located at the rapid descent of the subsurface salinity minimum (Whitworth and Nowlin, 1987), and the PF can be defined by the northern limit of the subsurface

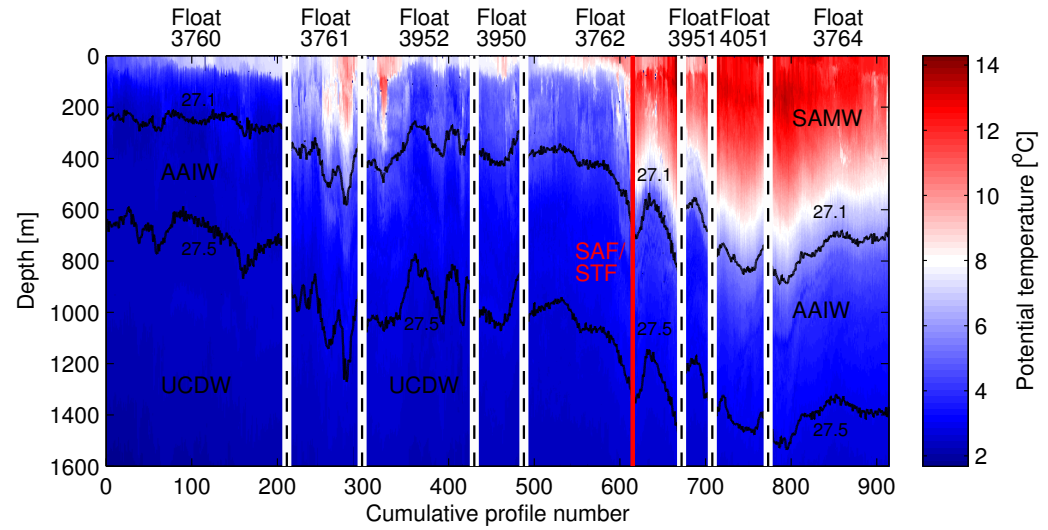

(a)

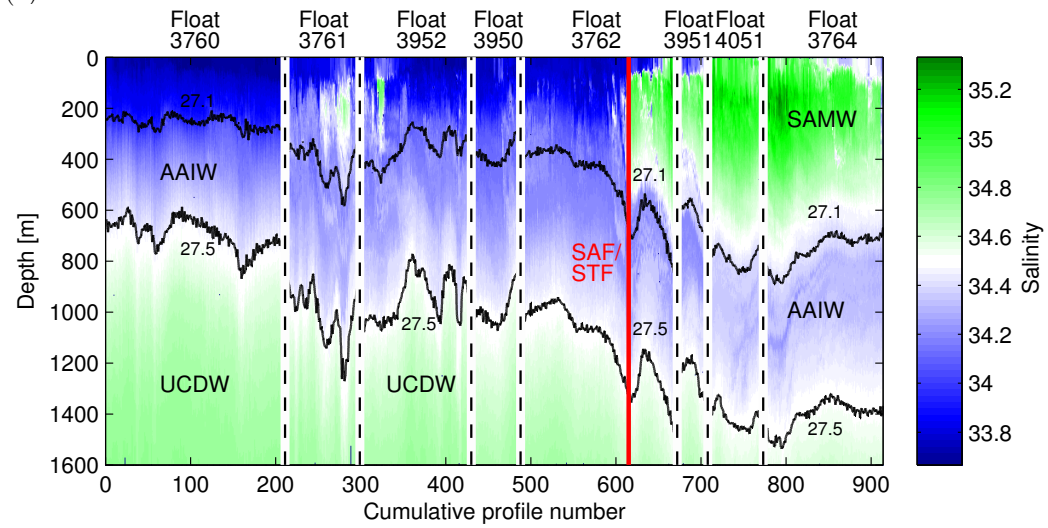

(b)

Figure 3.3: Vertical distribution of (a) potential temperature and (b) salinity along trajectories of the floats. The position of the Subantarctic Front (SAF) is indicated by the vertical red line. Selected labeled potential density contours delimit water masses north and south of the SAF/STF: subantarctic mode water (SAMW) is defined as $\sigma_\theta \leqslant 27.1\ \mathrm{kg\,m^{-3}}$, Antarctic Intermediate Water (AAIW) is defined as $27.1 \leqslant \sigma_\theta \leqslant 27.5\ \mathrm{kg\,m^{-3}}$ and Upper Circumpolar Deep Water (UCDW) is defined as $\sigma_\theta \geqslant 27.5\ \mathrm{kg\,m^{-3}}$. The vertical dashed lines separate floats.

2 °C temperature minimum at the 200 to 300 m depth range (Park et al., 1998). Recent studies have shown that fronts in the Antarctic Circumpolar Current are complex and that their position and intensity are highly variable in time (Sokolov and Rintoul, 2007, 2009a). Upstream and downstream from topographic features, fronts often have many branches which merge, diverge and meander with time (Langlais et al., 2011). The different branches of the SAF are known to merge into an intense jet north of the Kerguelen Plateau, while downstream of the plateau, the jet shows a strong variability and the fronts split (Sallee et al., 2008). The PF location in the region of the Kerguelen Plateau is more ambiguous than that of the SAF. The northern branch of the PF has been observed (Belkin and Gordon, 1996) and modelled (Langlais et al., 2011) to pass both north and south (Park et al., 1998) of the Kerguelen Plateau with the possibility of atmospheric forcing as a control factor (Sallee et al., 2008).

The EM-APEX profiles of potential temperature (hereinafter referred to as temperature) and salinity enable us to identify oceanographic features near the Kerguelen Plateau (Figure 3.3). Profiles, which are shown in their sampling order are grouped by floats and the floats are organised in decreasing mean sampling latitude. This gives the composite trajectories the appearance of a meridional transect. In the EM-APEX data, temperature varies between 1.8 and 14.3 °C, and salinity between 33.7 and 35.3. Combining the information from the positions of the velocity jets using the satGEM geostrophic velocity product (Figure 3.4), the EM-APEX temperature profiles (Figure 3.3a) and the EM-APEX salinity profiles (Figure 3.3b), we are able to identify the Southern ocean fronts sampled by the EM-APEX floats. Using the surface velocity jets determined from the satGEM product as an indication of the position of fronts, we find an intense jet north of the Kerguelen Plateau (Figure 3.4) that is coherent over the sampling period. This jet diverges and splits downstream of the Kerguelen Plateau ($80°E$). We identify this as the middle and northern branches of the SAF, likely merged with the southern branch of the STF. Float 3762 crossed the path of this jet at $42.5°S - 67.5°E$, recording a jump (from south to north of the front) in temperature from 5.21 °C to 11.36 °C and in salinity from 34.05 to 34.85

at 200 m depth, which corresponds to both the ranges of the SAF and STF. Note that Damerell et al. (2013) defined a similar front using the SOFine ship-based hydrographic data from the same region and period of time.

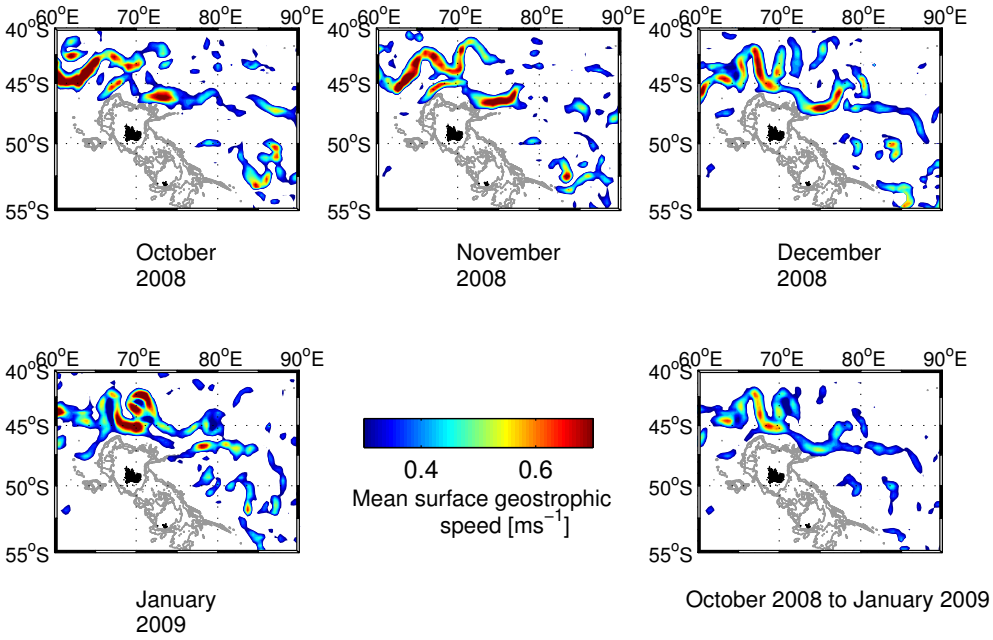

Figure 3.4: Monthly mean satGEM derived surface geostrophic speed (colour scale). The mean geostrophic speed map for October 2008 to January 2009 represents the period when the EM-APEX floats were sampling in the area. To identify jet flows, mean surface geostrophic speeds below 0.30 m s^{-1} are ignored. Topography contours range from 0 to 1500 m at 500 m intervals (grey).

South of the SAF/STF, we identify Upper Circumpolar Deep Water (UCDW) as the water mass below $\sigma_\theta = 27.5$ kg m^{-3} (Figure 3.3). This corresponds to water cooler than 2.34 °C and salinity above 34.5. North of the SAF/STF, we define Subantarctic Mode Water (SAMW) as $\sigma \leqslant 27.1$ and the Antarctic Intermediate Water (AAIW) as $27.1 \leqslant \sigma \leqslant 27.5$, which corresponds to $2.7 \leqslant \theta \leqslant 5.8$ °C and $34.4 \leqslant S \leqslant 34.7$. These definitions are consistent with those used by Sloyan and Rintoul (2001) and Damerell et al. (2013).

The presence of the PF is not obvious in the data. Firstly, there is no jet signature between the SAF/STF and Kerguelen Island to indicate its

position (Figure 3.4). More significantly, the 2 °C isotherm at the 100 to 300 m depth range is not found in the EM-APEX profiles. Only the 2.2 °C isotherm appears at 300 m in the first 50 profiles of the southernmost float (float 3760). In the SOFine hydrographic survey, the 2 °C isotherm is found at 200 m in the South-East section not sampled by the EM-APEX floats (Damerell et al., 2013). This suggests that the PF is likely located between the SAF/STF and Kerguelen Island but is not sampled by the EM-APEX floats. The horizontal speed profiles for the whole data set as well as the dynamic height of 100 m relative to 1500 m value of each profile confirm the water mass property and satGEM analysis (Figure 3.5). Horizontal velocity reaches a maximum of 2.1 $\mathrm{m\,s^{-1}}$ and have an overall mean value of 0.3 $\mathrm{m\,s^{-1}}$.

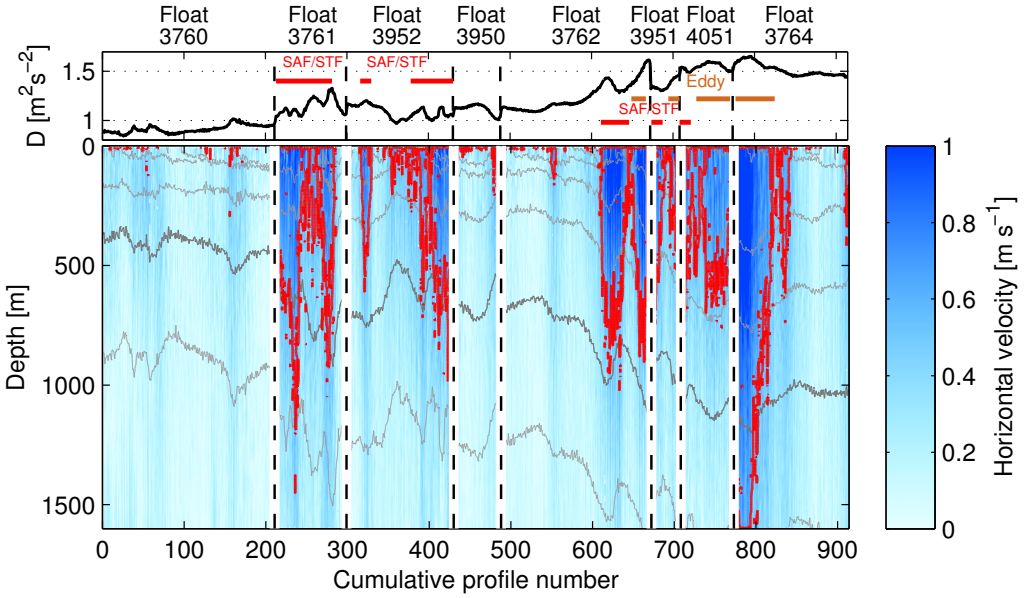

Figure 3.5: Dynamic height ($D_{(100,1500)}$) (top panel) and vertical distribution of horizontal velocity (main panel) along floats' trajectories. The 0.55 $\mathrm{m\,s^{-1}}$ speed contour (red) identifies the location of jets. Potential density contours (σ_θ =26.1, 26.4, 26.7, 27.0, 27.3 (bold) and 27.6 $\mathrm{kg\,m^{-3}}$) are shown (grey). Profiles located in the SAF/STF and the eddy are indicated respectively by red and brown horizontal bars. The vertical dashed lines separate floats.

Another feature observed in the data is a large amplitude meander of the front that evolves in time and is hereinafter referred to as the eddy. The eddy is located between $44°S - 42°S$ and $69°E - 73°E$ (Figure 3.1). Three floats

(3764, 4051 and 3951) sampled along the rim of the eddy. Its signature in the speed profiles is similar in magnitude and depth to that of the SAF/STF. Note that this feature is identified using satellite SST data as a cold core eddy with water temperature typical of south of the SAF/STF (not shown here) but this is not seen in the floats's data since they sampled the rim rather than the core of the eddy. The dynamic height ($D_{(100,1500)}$) range of the eddy's rim is different from that of the SAF/STF (see Figure 3.5 top panel).

3.2 Buoyancy frequency

The buoyancy frequency (N), also called the $Brunt - V\ddot{a}is\ddot{a}l\ddot{a}$ frequency, is expressed as an angular frequency in radians per second [rad s^{-1}], often abbreviated as s^{-1}

$$N = \sqrt{gE} \simeq \sqrt{-\frac{g}{\rho_\theta}\frac{d\rho_\theta}{dz}}, \tag{3.1}$$

where g is the acceleration due to gravity, E is the stability of the water column and ρ_θ is the potential density (a more detailed discussion on the definition of the buoyancy frequency can be found in Pickard and Emery (1990) p.54).

To derive N, we use equation (3.1) with potential density derived at local reference levels through the water column. We apply the Fofonoff adiabatic steric anomaly levelling method developed by Bray and Fofonoff (1981) where the potential density gradient is estimated using a linear regression. The temperature data are therefore effectively adiabatically referenced back to the mid-point of the vertical pressure window, in our case a 6 dbar pressure window, before being used to derive the potential density.

For the purpose of this study, we estimate two buoyancy frequencies that are derived over different time and length scales. First, we derive "local" squared buoyancy frequency profiles, N^2 using the EM-APEX data (Figure 3.6). For this local N^2, the density gradient is estimated using a linear regression of potential density on pressure, calculated over a vertical

pressure window of 12 dbar in equation (3.1). N^2 varies between 0 and $3.4 \times 10^{-4}\,(\mathrm{rad\,s^{-1}})^2$ with a mean value of $8.6 \times 10^{-4}\,(\mathrm{rad\,s^{-1}})^2$ (Figure 3.6). We use the same method to derive mean local squared buoyancy frequency ($< N^2_{ref} >$) profiles (not shown), using a longer vertical averaging pressure window (24 dbar) as well as a horizontal averaging window. The <> denote horizontal averaging over 20 profiles.

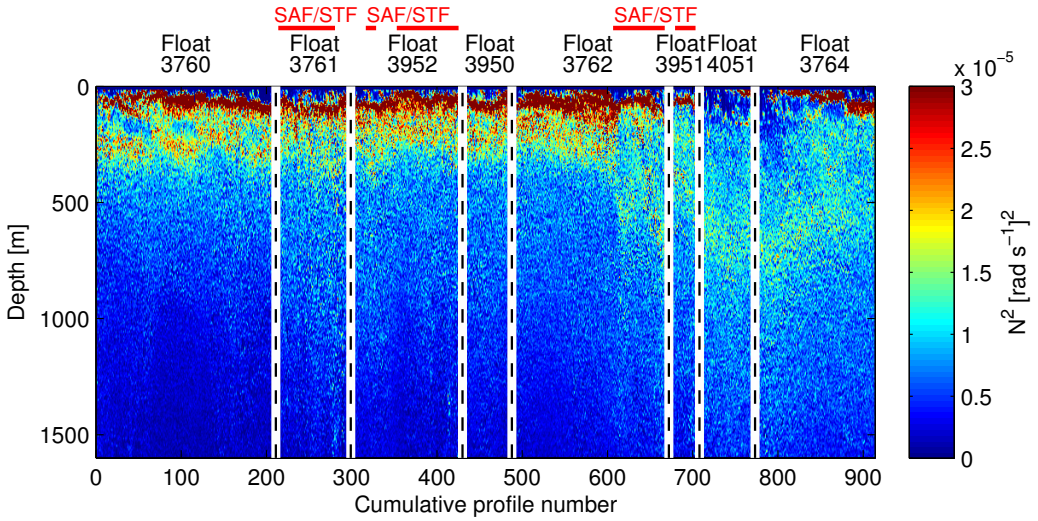

Figure 3.6: Vertical distribution of the "local" squared buoyancy frequency N^2 along trajectories of the floats. Profiles located in the SAF/STF front are indicated by red horizontal bars. The vertical dashed lines separate floats.

3.3 Mixed-layer depth

The mixed-layer is the upper layer of the ocean where hydrographic properties such as temperature and salinity are uniform. Sources of mixing in the mixed-layer are the breaking of wind generated surface waves, shear instability due to wind-driven currents, convection and Langmuir circulation. In the Southern Ocean, the mixed-layer typically reaches 50 m in the summer and can exceed 600 m in the winter where AAIW and SAMW formation takes place (Dong et al., 2008; Sallee et al., 2010; Holte et al., 2012).

In this study, the depth of the mixed-layer is a key parameter since the

shear-strain parameterization and Thorpe-scale methods applied to derive mixing estimates are only valid below the mixed-layer. We define the mixed-layer depth (Figure 3.7) as the depth at which the potential density changes by $\Delta\rho_\theta = 0.03$ kg m^{-3} relative to the potential density at $Z_{ref} = 10$ m (de Boyer Montégut et al., 2004).

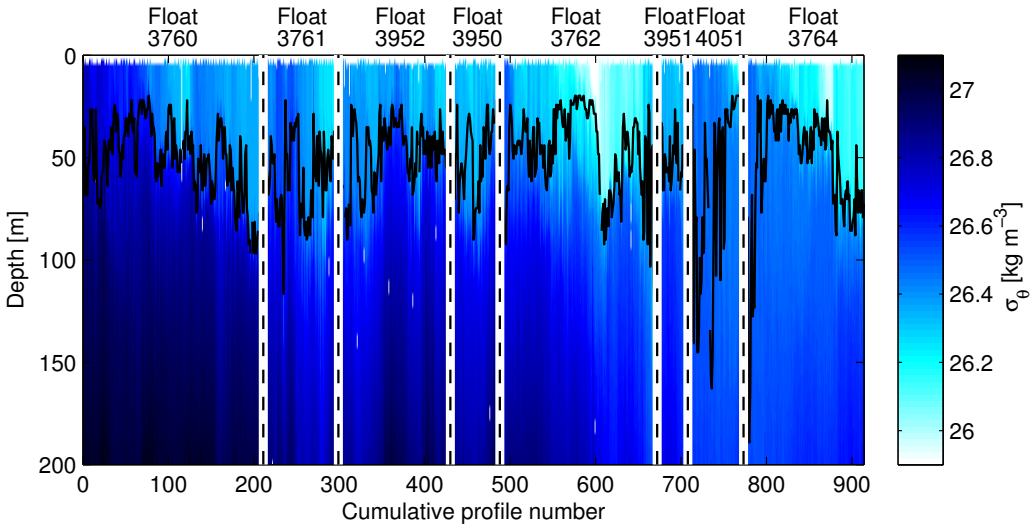

Figure 3.7: Mixed layer depth (black contour) overlying vertical distribution of potential density along floats' trajectories. The vertical dashed lines separate floats.

The reference depth, as defined by de Boyer Montégut et al. (2004), $Z_{ref} = 10$ m, is used to avoid the signature of the diurnal cycle. In this study, the mixed-layer depth varies between 20 and 190 m with a mean value of 53 m.

3.4 Relative vorticity

Vorticity is twice the angular velocity at a point in a fluid (Talley et al., 2011). The local vertical component of the relative vorticity (ζ) has units of inverse time [s^{-1}]

$$\zeta = \left(\frac{\partial v}{\partial x} - \frac{\partial u}{\partial y}\right), \tag{3.2}$$

where u and v are the components of the horizontal velocity vector in the x and y coordinate system.

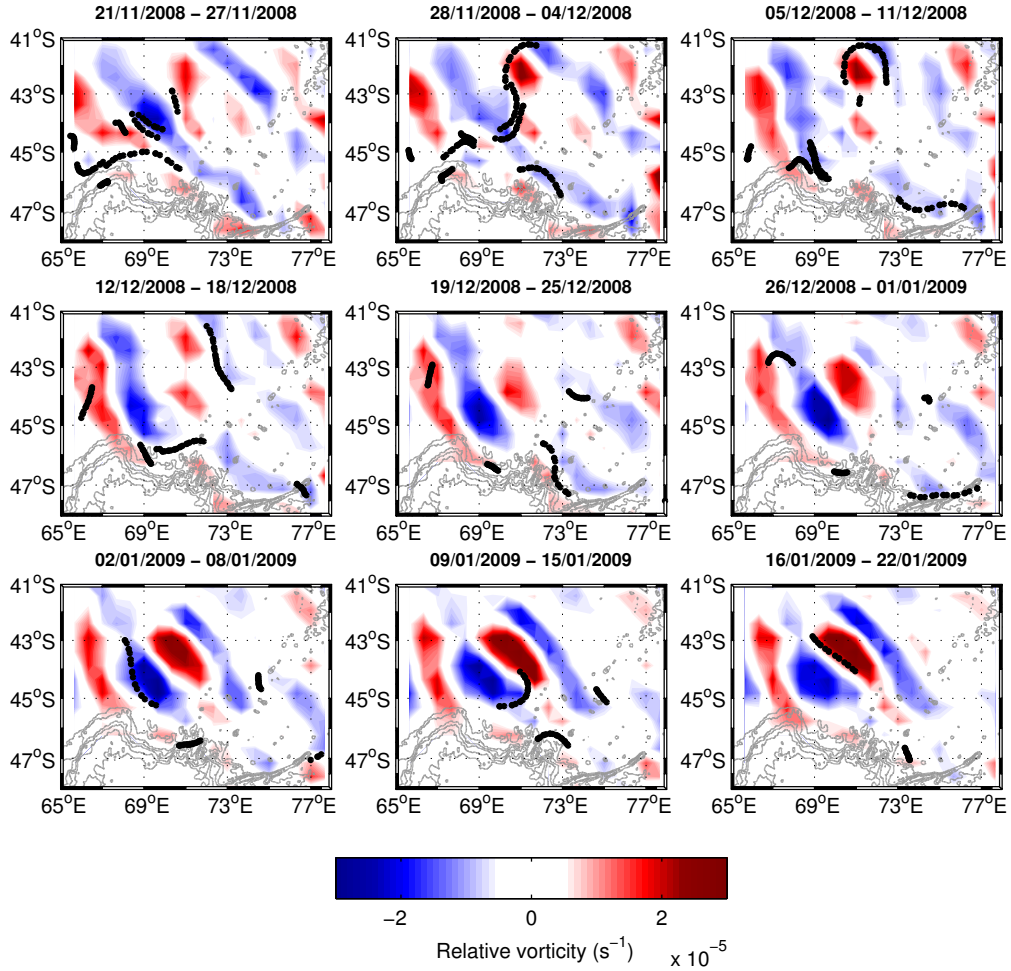

Figure 3.8: Weekly satGEM derived mean surface relative vorticity maps (colour scale). The nine maps corresponds to the sampling period of the EM-APEX floats between November 2008 and January 2009 with the position of individual profiles sampled during each week indicated (black dots). Topography contours range from 500 to 3000 m at 500 m intervals (grey).

Here we apply equation (3.2) on the horizontal scales $\partial x = \partial y = 50$ km to SatGEM velocity fields, a weekly geostrophic velocity products from combined hydrographic data (GEM field) and satellite altimetry data (AVISO) (Meijers et al., 2011). The resulting weekly maps of mean relative vorticity

show a strong variability in the relative vorticity with values ranging from $-3.1 \times 10^{-5}\,\mathrm{s}^{-1}$ to $3.1 \times 10^{-5}\,\mathrm{s}^{-1}$ (Figure 3.8). The eddy identified in Section 3.1 is associated with large positive relative vorticity values throughout the sampling period.

Chapter 4

METHODS OF ESTIMATING MIXING

4.1 Thorpe-scale method

Density inversions can be used to estimate the rate of turbulent mixing using a Thorpe scale analysis. First, we explain the theory of Thorpe scale parameterization of diapycnal turbulent eddy diffusivity. Next we describe how this method is applied to 914 EM-APEX density profiles. We then discuss the overall patterns and levels of turbulent mixing derived.

4.1.1 Thorpe-scale theory

The Thorpe scale (L_T) has a size that is characteristic of turbulent overturns. It is defined as the root mean square of the vertical displacement (d) of a water parcel in a gravitationally unstable region when the density profile is re-ordered to be continuously stable (Thorpe, 1977)

$$L_T = \sqrt{< d^2 >}, \tag{4.1}$$

where the angle brackets denote an averaging process in the vertical (see Figure 4.1).

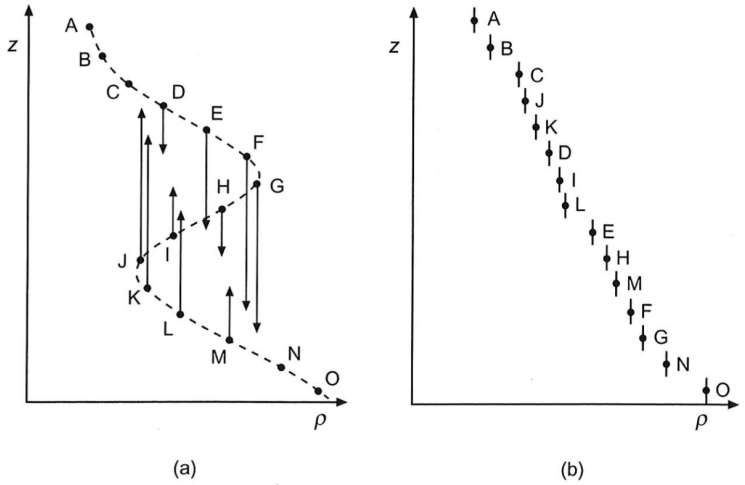

Figure 4.1: Estimating the vertical displacement d: A stable profile of density (b) is derived from the observed density profile (a). The vertical arrows show the vertical displacement d needed to bring each measured value to a statically stable order. (From Thorpe (2005) p.176.)

Microstructure studies (Dillon, 1982; Crawford, 1986; Ferron et al., 1998; Stansfield et al., 2001) have shown that the Thorpe scale is proportional to the Ozmidov scale (L_O), as follows

$$L_O = aL_T, \tag{4.2}$$

where a is an empirical constant of proportionality determined from microstructure observations. Studies have found that a ranges between 0.65 and 0.98 (for a review see Finnigan et al., 2002). For the present work, we use $a = 0.8$ (Dillon, 1982). The Ozmidov scale (Ozmidov, 1965) is arrived at by dimensional analysis as the scale at which gravitational forces proportional to N^2 are equal to the inertial forces of turbulence, which are proportional to the dissipation rate

$$L_O = \left(\frac{\epsilon}{N^3}\right)^{1/2}, \tag{4.3}$$

where ϵ is the dissipation rate and N is the buoyancy frequency. Combining equations (4.3) and (4.2), we can estimate the dissipation rate (ϵ) for each turbulent overturn

$$\epsilon = a^2 {L_T}^2 < N_{L_T} >^3. \tag{4.4}$$

Here, $< N_{L_T} >$ is the average buoyancy frequency over the turbulent overturn (typically 10 to 20 m). Using the Osborn (1980) relation, we derive the diapycnal diffusivity (K_ρ) for each turbulent overturn

$$K_\rho = \Gamma\epsilon < N^{-2}_{100m} >, \tag{4.5}$$

where the mixing efficiency, Γ, is assumed to be constant $\Gamma = 0.2$ (Thorpe, 2005); ϵ is the mean dissipation rate for each turbulent overturn; and $< N^{-2}_{100m} >$ is the mean buoyancy frequency squared over 100 m scale. Here we invoke a scale separation argument where the N^2 variability at 100 m scale is an approximation for a time mean. The mixing efficiency Γ has been shown to vary (Ivey et al., 2008), but $\Gamma = 0.2$ is typically used (for further details, see discussion in Polzin et al., 2013).

4.1.2 Implementation of Thorpe-scale method

To estimate diapycnal turbulent eddy diffusivity from observed density profiles using equations (4.4) and (4.5), we first derive the Thorpe scale (L_T) and the associated buoyancy frequency squared ($N^2_{L_T}$). Then, we apply a test based on known instrument accuracy, to ensure that dubious Thorpe scales are excluded. Finally, turbulent mixing is estimated. Note that in some previous studies, temperature profiles, which often have lower noise levels, have been used instead of density profiles to estimate Thorpe scales. In this study, the presence of density compensated temperature/salinity intrusions could lead to erroneous inversion detection if temperature profiles were used.

Deriving the Thorpe scale lengths

Theoretically, the vertical displacement (d) in equation (4.1) is the difference in depth between the original and re-ordered positions when a measured density profile is ordered to obtain a density profile that increases monotonically with depth. The accuracy of this displacement is dependent on the noise level of the density data and its local mean vertical gradient (Ferron et al., 1998). When the noise is high and the local mean vertical gradient low, ordering the raw density profiles might lead to measuring density inversions that are due to noise rather than real inversions.

Several tests exist to detect spurious overturns and are reviewed in Galbraith and Kelley (1996); MacKinnon et al. (2011). Here we first apply a method to detect "real" density inversions in the density profiles developed by Ferron et al. (1998). With this method, it is not the raw potential density profile that is re-ordered to measure the vertical displacement but rather an intermediate potential density profile. To obtain the intermediate potential density profile, we use a "hinge" potential density value (ρ_{θ_0}), which we set at ρ_{θ_0} =1027.8320 $\mathrm{kg\,m^{-3}}$ (Ferron et al., 1998) and a density accuracy ($\delta\rho$) which we estimate[1] to be $\delta\rho = 0.0019$ $\mathrm{kg\,m^{-3}}$. The resulting intermediate profile is only composed of fluctuations that are integer multiples of the

[1]The density accuracy is based on the SBE41 CTD specifications provided by Seabird: the temperature accuracy is 0.002 °C and the salinity accuracy is 0.002.

relative accuracy (see Ferron et al. (1998) appendix for details).

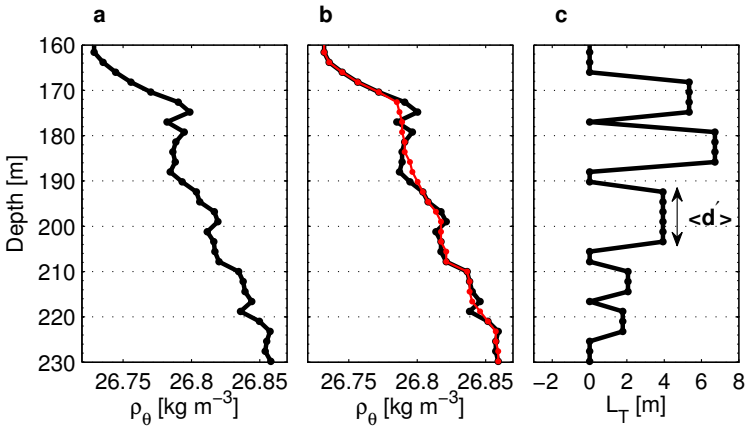

Figure 4.2: Section of a vertical profile from float 3952 of (a) potential density, (b) intermediate potential density (black) and ordered intermediate potential density (red) and (c) corresponding Thorpe scales.

The intermediate potential density profile is re-ordered to be gravitationally stable, and the vertical displacement $d = z_0 - z_r$ is the difference between the position (z_0) in the intermediate profile and the ordered position (z_r) in the gravitationally stable intermediate potential density profile (Figure 4.2). Finally, we derive the Thorpe scale as the root mean square of the vertical displacement ($< d >$) of each density overturn (Figure 4.2).

The buoyancy frequency (N) is defined in Section 3.2. We calculate $N^2_{L_T}$ for each turbulent overturn identified by Thorpe scales with the height of the density inversion as the vertical fitting window (dz).

Dubious Thorpe scales are discarded using the Galbraith and Kelley (1996) minimum thickness test, which puts a limit on the resolution of the data set. The minimum height of a density overturn and therefore Thorpe scale that can be resolved in a given density profile is defined as

$$L_{\rho min} = \frac{g}{N^2_{L_T}} \frac{2\delta\rho}{\rho_{\theta ref}}, \tag{4.6}$$

where $\rho_{\theta ref}$ is a reference potential density for that profile (mean value over the water column) and $\delta\rho = 0.0019$ kg m^{-3} is the density accuracy of the instrument. Density overturns that are smaller than the minimum thickness

($L_{\rho min}$) are discarded (Figure 4.3). As well as discarding spurious turbulent overturns, this test might discard some true turbulent overturns. The largest turbulent overturns have been shown to make the most important contribution to turbulent mixing (Stansfield et al., 2001), however discarding small turbulent overturns could lead to underestimating overall mixing rates.

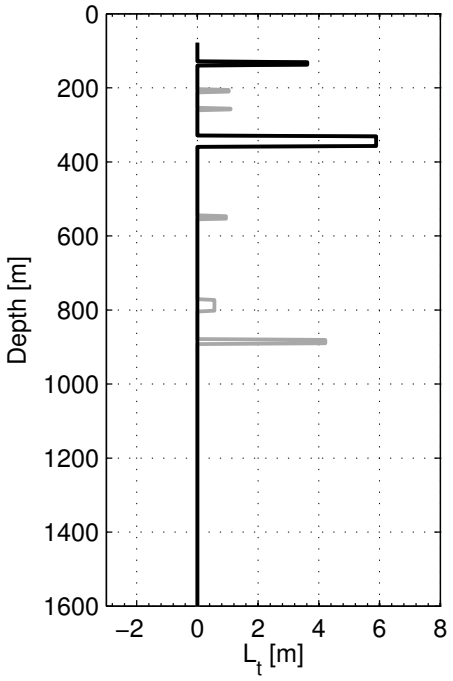

Figure 4.3: Example of Thorpe scale vertical profile from float 3762. In black is the post-test Thorpe scale profile and in grey are the overturns discarded by the minimum overturn thickness test. Note that the mixed-layer data were removed.

Estimating diapycnal eddy diffusivity

Once we have accurate L_T and $N^2_{L_T}$ estimates, we are able to derive the dissipation rate (ϵ) for each overturn by applying equation 4.4, where we use $\sqrt{N^2_{L_T}}$ for $< N >$. The mean diapycnal turbulent eddy diffusivity (K_ρ) for each overturn can then be estimated using equation (4.5). We exclude data in the mixed-layer where convective processes dominate mixing, and therefore where equation (4.5) is not appropriate.

4.2 Shear-strain parameterization of dissipation

The dissipation rate (ϵ) can be predicted from shear and strain measurements of internal waves using finescale parameterizations (Gregg, 1989; Polzin et al., 1995). Finescale parameterization is based on (1) the assumption that most of the turbulent mixing is driven by breaking internal waves (locally and remotely generated) in the stratified ocean (Alford and Gregg, 2001), and (2) the notion of a downscale energy cascade. The finescale parameterizations have been widely used in the past decade (e.g. Mauritzen et al., 2002; Naveira Garabato et al., 2004; Sloyan, 2005; Kunze et al., 2006; Alford et al., 2007; Park et al., 2008; Fer et al., 2010; MacKinnon et al., 2011; Wu et al., 2011; Whalen et al., 2012), mostly because the observations needed (vertical density and velocity measurements) to derive the dissipation rate with this method are much more easily acquired than direct dissipation microstructure observations.

4.2.1 Ocean mixing and the energy cascade

The downscale energy cascade in the internal wave band (Figure 4.4), also referred to as the forward cascade, transfers energy and momentum towards smaller scale internal waves (from low to high vertical wavenumber), mostly as a result of nonlinear internal wave-wave interactions (McComas and Muller, 1981). The high vertical wavenumber internal waves at the end of the cascade break and dissipate their energy through overturns that result in viscous dissipation at the high wavenumber end of the inertial subrange (Polzin, 2004). The dissipation rate (ϵ) is typically used as a measure of the turbulence's intensity. As well as the downscale energy cascade, in the ocean there is an inverse cascade of energy associated with barotropic modes (Ferrari and Wunsch, 2009). This inverse cascade is not part of the finescale parameterization theory. Direct *in situ* estimates of the dissipation rate can in theory only be obtained by resolving the centimetre scale at which turbulent kinetic energy is being dissipated by molecular viscosity (Polzin et al.,

2013). By measuring the dissipation rate in the inertial subrange (wavelengths below 1 cm Figure 4.4), microstructure instruments provide the most accurate estimates of turbulent mixing.

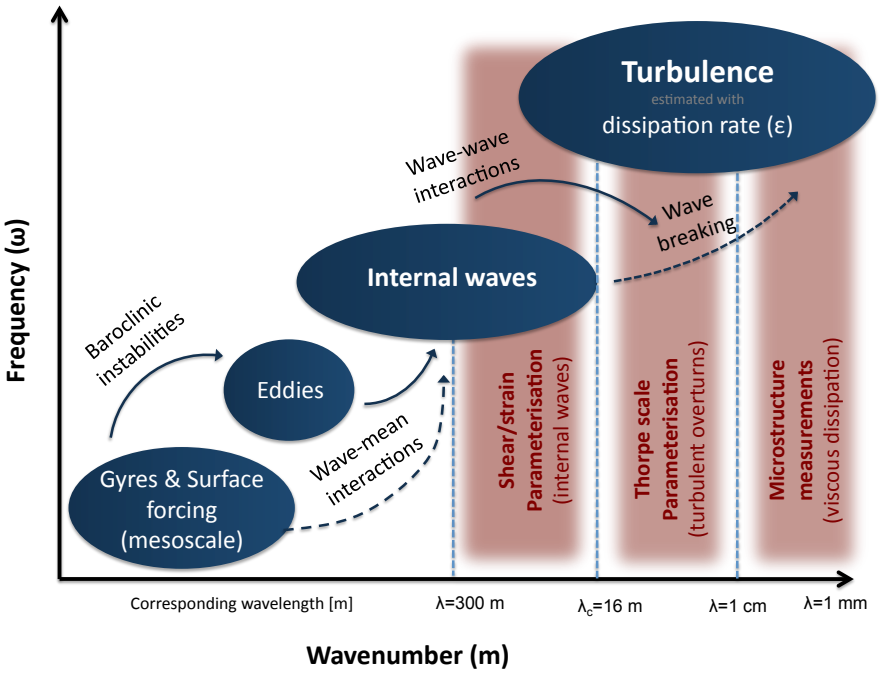

Figure 4.4: Schematic of the downscale energy cascade in the frequency-wavenumber domain leading to turbulent mixing; also shown are various methods (red highlighted areas) available to estimate this turbulent mixing, and the vertical scales to which they are applied. Equivalent approximate wavelengths estimates are provided along the wavenumber axis.

The Thorpe-scale method (see Section 4) uses information from the vertical scale of turbulent overturns, while the shear-strain finescale parameterization uses information from the smallest resolved scales of the internal wave field. When inferring the dissipation rate on large spatial and time scales, one often assumes that the rate of downscale energy transfer in the downscale cascade is constant at all scales. Under this assumption, all of the above methods measure the same dissipation rate. In reality, the larger the scale used to infer the dissipation rate, the more assumptions are made and the more uncertainty in the final mixing estimates (MacKinnon et al., 2011).

Below we explain the theory behind shear-strain finescale parameterization.

4.2.2 Theory of shear-strain parameterization

Turbulence is strongly related to the energy and shear of the internal wave field through wave-wave interaction theory (Polzin et al., 1995). By combining observations of the internal wave field (finescale measurements) with theoretical models of energy transfer through wave-wave interactions, the local turbulent dissipation rate can be estimated. As mentioned, Garrett and Munk (1975) (hereinafter GM) were the first to describe and model the background internal wave field in terms of a vertical wavenumber and frequency spectrum using velocity and temperature observations from Site 'D' in the western North Atlantic Ocean (39°20′ N, 70° W) (Garrett and Munk, 1972; Fofonoff, 1966). Additional work by Garrett and Munk (1975) and Cairns and Williams (1976), denoted GM75 and GM76 respectively, further characterised the background internal wave field.

McComas and Muller (1981) developed a theoretical spectral model based on resonant interaction theory to obtain a stationary vertical wavenumber spectrum space. Henyey et al. (1986) used ray tracing simulations to model the average transport of energy to small scales. Both models led to similar predictions of the local turbulent dissipation rate from internal wave properties (Polzin et al., 1995). Gregg (1989) was the first to apply these models to shear and strain observations to obtain estimates of the dissipation rate. Over the next 20 years, theoretical work (e.g. Lvov et al., 2004), observational work (e.g. Polzin et al., 1995) and numerical simulations (e.g. Winters and D'Asaro, 1997) further tested and refined the model of energy transfer that predicts the turbulent dissipation rate from the internal wave energy level as derived from finescale measurements of the vertical shear (from velocity profiles) and vertical strain (from density profiles). Note that finescale parameterizations are always described relative to the GM internal wave spectrum. For further details, Polzin et al. (2013) provide an in-depth discussion on finescale parameterizations for estimates of turbulent dissipation.

As suggested by the theory (Henyey et al., 1986) and some observations

(Polzin et al., 1995), the dissipation rate scales quadratically with the shear spectral level. Assuming the spectral energy transfer arrives at dissipation scales (ϵ) where wave-breaking dissipates turbulent kinetic energy, the dissipation rate (ϵ) is

$$\epsilon = \epsilon_0 \Big(\frac{N^2}{N_0^2}\Big) \frac{< V_z^2 >^2}{< V_{z-GM}^2 >^2} \frac{3(R_\omega + 1)}{2\sqrt{2} R_\omega (R_\omega - 1)^{1/2}} \frac{f \cosh^{-1}(N/f)}{f_0 \cosh^{-1}(N_0/f_0)}. \tag{4.7}$$

Constants from the background internal wave field as described by the GM76 model (latitude 32.5°N) are the dissipation $\epsilon_0 = 8 \times 10^{-10}$ W kg^{-1}, the buoyancy frequency $N_0 = 3$ cph extrapolated to the surface in GM76 and the inertial frequency $f_0 = 7.86 \times 10^{-5}$ s^{-1}. N is the buoyancy frequency; $< V_z^2 >$ is the integrated variance of the vertical shear normalized by N; $< V_{z-GM}^2 >$ is the GM76 model integrated vertical shear variance; R_ω is the shear-to-strain variance ratio and f is the local inertial frequency (f). Here (and throughout), the angle brackets denote variance integrated over a specified vertical wavenumber range. We follow the Polzin et al. (2002) and Naveira Garabato et al. (2004) notations.

The shear-to-strain variance ratio (R_ω) is defined as

$$R_\omega = \frac{< V_z^2 >}{< \xi_z^2 >}, \tag{4.8}$$

where $< \xi_z^2 >$ is the strain variance integrated in the specified vertical wavenumber range. We spatially Fourier transform each strain (ξ_z) and shear (V_z) segment to obtain the strain spectra (Φ_{strain}) and the shear spectra (Φ_{shear}) respectively. The shear variance and the strain variance are then determined by integrating the shear spectra (Φ_{shear}) and the strain spectra (Φ_{strain}) from a minimum vertical wavenumber (m_0) to a cutoff vertical wavenumber (m_c)

$$< V_z^2 >= \int_{m_0}^{m_c} \Phi_{shear} dk and \qquad < \xi_z^2 >= \int_{m_0}^{m_c} \Phi_{strain} dm. \tag{4.9}$$

The cutoff vertical wavenumber (m_c) is the threshold where there is a transition from quasi-linear wave-wave interactions to strongly non-linear wave breaking (D'Asaro and Lien, 2000). It is defined as the point where the integrated shear variance reaches $2\pi N^2/10$ (Polzin et al., 2013). The shear variance from the GM model spectrum $< V^2_{z-GM} >$ is derived from integration over the same wavenumber band, using the GM model parameters of GM76 ($E_0 = 6.3 \times 10^{-5}$ is a dimensionless energy, $b = 1300$ m is the vertical stratification scale and $j* = 3$ is the mode number scale). To estimate the diapycnal turbulent eddy diffusivity (K_ρ) from the estimates of ϵ, we use the Osborn (1980) relation

$$K_\rho = \Gamma \frac{\epsilon}{N^2}, \tag{4.10}$$

where the mixing efficiency ($\Gamma = 0.2$) is assumed to be a constant. For further details about the choice of Γ, see discussion in Polzin et al. (2013). In regions where the water is not stably stratified or where mixing is dominated by convective processes, the Osborn relation is not valid.

4.2.3 Implementation of shear-strain parameterization

Deriving shear and strain spectra

We derive the vertical shear (V_z) for each of the 914 velocity profiles from the EM-APEX floats defined as

$$V_z = \frac{\partial u}{\partial z} + i\frac{\partial v}{\partial z}, \tag{4.11}$$

where $V = u + iv$ is the horizontal current. Shear, which is calculated as a centred difference over $\partial z = 6$ m, has a vertical resolution of 3 m.

Strain ξ is a measure of changes of the mean stratification

$$\xi = \frac{N^2 - N^2_{ref}}{N^2_{ref}}, \tag{4.12}$$

where N^2 is the local buoyancy frequency and N^2_{ref} is the local mean buoyancy frequency. The two different buoyancy frequencies are derived using

the same method but over different length and time scales (see Section 3.2). Strain is estimated from density profiles with a vertical resolution of 2.2 m and subsequently linearly interpolated to a 3 m grid. Starting from the ocean surface, each shear and strain profile is divided into 384 m long vertical segments, overlapping by 360 m. We apply a Hanning window to each segment before applying a Fourier transform (over 128 points) to the shear and the strain vertical profiles, computing their vertical wavenumber power spectral density (or spectrum).

We apply two transfer functions modified for the floats' characteristics to correct the shear spectrum for unresolved variance due to the instrument's limitations, data processing and instrument's characteristics (adapted from Polzin et al., 2002, 2013).

Estimating shear and strain variance

To derive the variance, the spectra is integrated over a specified vertical wavelength band. Ideally, this window covers the entire internal waveband, particularly if the spectra is not flat, but it is often set to a constant range such as 50 to 300 m (Naveira Garabato et al., 2004; Whalen et al., 2012; Waterman et al., 2013). Here, the high vertical resolution of the velocity data from the EM-APEX floats enables us to resolve the cutoff wavenumber and therefore to use the appropriate minimum wavelength of integration for each profile. We use the cutoff wavenumber (m_c), derived for each vertical segment (the point where the integrated shear variance reaches $2\pi N^2/10$), as the minimum wavelength of integration. The corresponding cutoff wavelength (λ_c) has a mean value of 16 m (Figure 4.5a). The minimum limit integration wavelength is $\lambda_0 = 1/m_0$ =384 m, which is a compromise between integrating at wavelengths large enough to resolve vertical structure but not so large that non-wave (e.g. geostrophically balanced motion) variance contaminates the spectra.

Shear-to-strain variance ratio

The shear-to-strain variance ratio (R_ω) is derived with (4.8) for each vertical segment of each profile. By definition, R_ω is larger than one when the hydrostatic approximation is invoked. It is an estimate of the internal wave field's mean aspect ratio from which, a measure of the wave field's bulk frequency content can be derived (Polzin et al., 2013). R_ω was first introduced by Fofonoff (1969) as a linear diagnostic to describe the frequency content of the internal wave field. Higher R_ω values imply a dominant presence of near-inertial waves, while lower R_ω values can be attributed to the presence of more high frequency internal waves at high vertical wavenumber or the presence of shear instabilities when $m > m_c$ (Polzin et al., 2003).

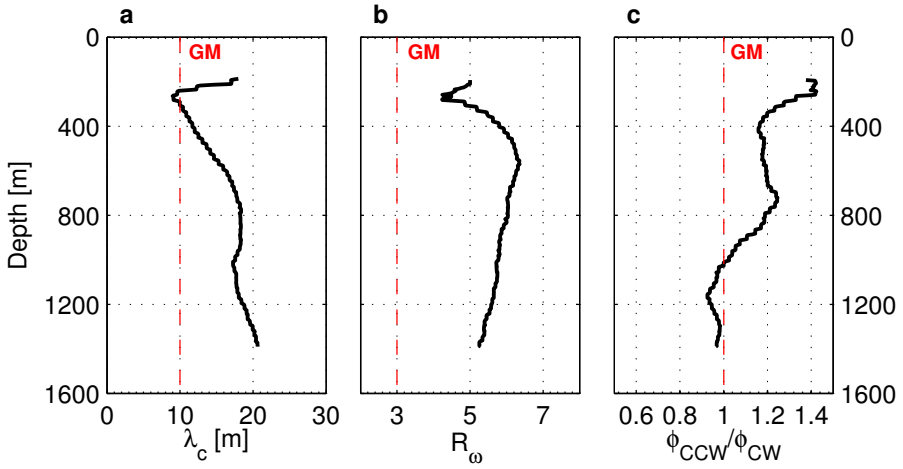

Figure 4.5: Mean EM-APEX vertical profiles of (a) cutoff wavenumber (m_c), (b) shear-to-strain ratio (R_w) and (c) ratio of CCW to CW rotating shear variance for the Kerguelen Plateau region. The vertical red dotted lines indicate the GM values.

For the GM model, $R_\omega = 3$. For $R_\omega > 3$, the ocean internal wave field has more energy in the near-inertial band than the GM model. Data from surveys at mid-latitude (Polzin et al., 2003) and at high latitudes (Naveira Garabato et al., 2004; Fer et al., 2010) found $3 < R_\omega < 14$. In this study, R_ω ranges from 1 to 19 with a mean value of 5.6 (Figure 4.5b). The shear-to-strain ratio calculation is not accurate in the mixed-layer and therefore not shown

in that region.

Ratio of counter-clockwise to clockwise rotating shear variance

The ratio of rotary-with-depth shear variance (counterclockwise (CCW) / clockwise (CW)), hereinafter ϕ_{CCW}/ϕ_{CW}, can be used to infer the dominant direction of energy propagation of rotationally affected internal waves. It represents an approximate decomposition into upward and downward propagating fields and may not be indicative of the energy flux in a multi-chromatic wave field. We define the counterclockwise shear variance (ϕ_{CCW}) and the clockwise shear variance (ϕ_{CW}) as

$$\phi_{CCW} = \frac{V_z[u/N] + V_z[v/N] + 2QS}{2} \tag{4.13}$$

and

$$\phi_{CW} = \frac{V_z[u/N] + V_z[v/N] - 2QS}{2}, \tag{4.14}$$

where V_z is the vertical shear, u and v are the zonal and meridional velocity components, N is the buoyancy frequency, and QS is the quadrature spectrum (Gonella, 1972).

This diagnostic was first used by Leaman and Sanford (1975) to describe the phase and energy propagation of internal waves from velocity observations. A dominance of CCW polarization of the shear suggests predominantly downward energy propagation in the Southern Hemisphere (upward phase propagation) and a dominance of CW polarization of the shear indicates that upward energy propagation dominates (downward phase propagation). Figure 4.5c shows the mean vertical profile of ϕ_{CCW}/ϕ_{CW} for the EM-APEX data.

Mixing estimates and confidence intervals

We apply (4.7) and (4.10) to observations and obtain dissipation and diffusivity estimates for each float profile. The deepest mixing estimate is at 1429 m depth since we use overlapping segments centred at equally spaced depths, with T-S profiles that reach 1621 m. The shallowest mixing estimate

varies depending on the mixed-layer depth (see Section 3.3). The statistical distribution of dissipation rate estimates, predicted to be log-normal by Gurvich and Yaglom (1967), has been found to be both log-normal (Gregg et al., 1973; Osborn and Lueck, 1985; Crawford and Dewey, 1990) and not log-normal (Lueck, 1988; Moum and Lueck, 1985).

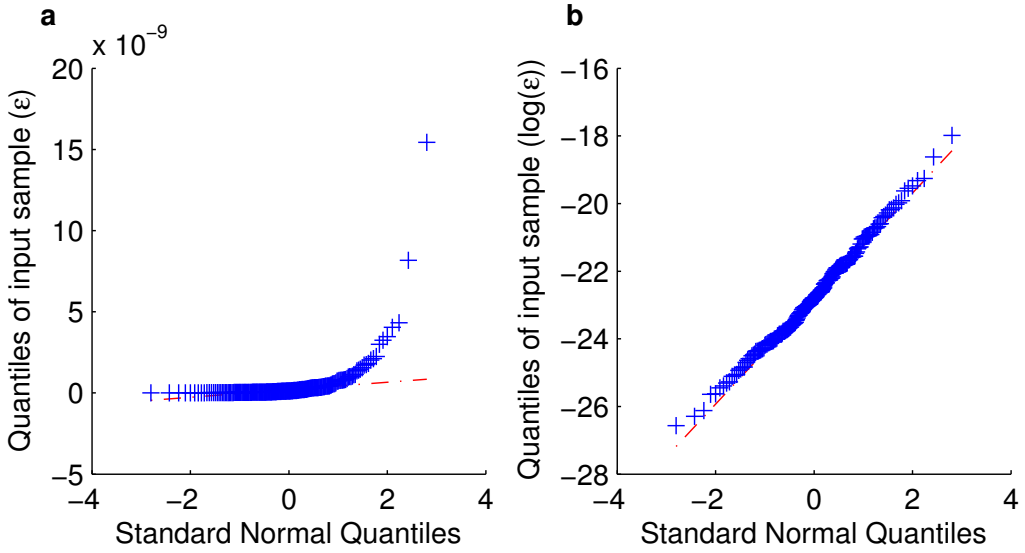

Figure 4.6: Q-Q plots of sample data (blue crosses) versus standard normal (red line) for (a) the dissipation rate and (b) logarithm of the dissipation rate at 1321 m, using all 914 profiles.

The distribution of the observed dissipation rate here is tested using the Lilliefors test, which determines the maximum deviation between the cumulative distribution function for the mixing data and that of a normal distribution with the mean and standard deviation estimated from the data (Glover et al., 2011). The mixing data from the EM-APEX floats fail the Lilliefors normality test and are not Gaussian. The plots of standard normal quantiles versus quantiles of input sample (Q-Q plots) show the sorted values from our data set against the expected values of the corresponding quantiles from the standard normal distribution. The quantiles here are points taken at regular intervals from the cumulative distribution function of the dissipation rate estimates. For a Gaussian data set, the points on a Q-Q plot should lie approximately on a straight line. Looking at the Q-Q plots of the dissipation

rate estimates, we see that it has a heavy-tail distribution (Figure 4.6 a) and that the logarithm of dissipation gives a good fit to a straight line, even if it has a higher probability at each end of the range than a log-normal distribution (Figure 4.6 b). Applying the Lilliefors test to the logarithm of the dissipation estimates confirms that at least the upper 500 m of the mixing data have a log-normal distribution (Figure 4.7). For further discussion on the statistical distribution of dissipation rate estimates, see Yamazaki and Lueck (1990) and Davis (1996).

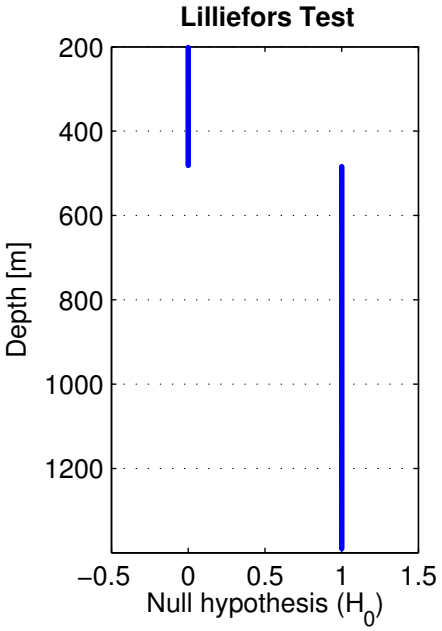

Figure 4.7: Lilliefors normality test where the null hypothesis H_0 is that the mixing data from the EM-APEX floats can not be distinguished from a normal distribution. H_0 of one implies the data are not normally distributed at the 5% significance level.

Different statistical methods can be applied to derive confidence intervals associated with the sampling of a data set. Here we apply both a standard deviation approach and a bootstrap method to the mixing data from the EM-APEX floats. In statistics, confidence intervals are often derived using the standard deviation when the data sample is large and likely to represent the true population (i.e. normally distributed). Since the mixing data

follows these assumptions for the upper water column, we estimate the 90% confidence intervals for the mixing variables by deriving the 1.644 standard deviations from the mean of the data (Figure 5.4, grey shading).

Next, we consider a bootstrap approach to derive confidence intervals for the mixing variables. The bootstrap method introduced by Efron (1979) is a simulation-based method as opposed to a probability distribution statistical approach that resamples the underlying data set to provide statistical confidence intervals. No assumptions are made about the underlying distribution of the data (Pol and Jermaine, 2005) and only independence of samples is a requirement, making this method mathematically simple and appropriate for almost any data set. Applying the bootstrap method, we estimate the confidence intervals for the mixing variables as the tenth largest and smallest value formed by randomly subsampling and averaging the data 100 times (Figure 5.4, red shading).

The standard deviation and bootstrap methods applied to the EM-APEX mixing data provide different estimates of the confidence intervals: the bootstrap method often used for mixing data sets (e.g. Thompson et al., 2007; Ledwell et al., 2011; Whalen et al., 2012; St. Laurent et al., 2012a; Waterman et al., 2013; Sheen et al., 2013) gives a confidence interval four to seven times more narrow than the standard deviation method. The apparent simplicity of the bootstrap method might mislead in the use of overly optimistic confidence intervals while the standard deviation approach is conservative. The true error associated with the sampling of the EM-APEX data is likely to be somewhere between the bootstrap and the standard deviation confidence intervals.

Limitations

At large vertical wavelengths ($\lambda > \lambda_c$) the net contributions of wave-wave interactions to a downscale energy cascade become smaller in relation to wave-mean interactions at larger vertical wavelengths (Polzin et al., 2013). The limitations of the finescale parameterization has a succinct answer in terms of the Froude number of the background flow: for large values of thermal

wind shear leads, the utility of the finescale parameterization as a diagnostic becomes limited. At smaller scales in near bottom regimes ($\lambda < \lambda_c$), internal wave scattering and reflection might interfere (Polzin et al., 2013). Non-local spectral transports due to wave breaking and resonant interactions will theoretically also decrease the effectiveness of the finescale parameterization. Certain environments such as stress-driven boundary layers, are dominated by processes that are not accounted for in the finescale parameterization. In such places, the parameterization is not expected to be accurate (for a thorough discussion, see Polzin et al., 2013).

There are many factors and theoretical assumptions that might lead to uncertainties in estimating ϵ from finescale parameterizations. However, the high vertical resolution of the EM-APEX data (3 m sample spacing) makes them much more suitable to use in finescale parameterisation techniques than traditional ADCP data (approximately 24 m sample spacing).

The uncertainty associated with the EM-APEX floats and with the sampling location using this finescale parameterization method to derive estimates of the dissipation rate and diffusivity is within a factor of ± 2 (Polzin et al., 1995, and as per personal communications).

Chapter 5

MIXING INTENSITY AND SOURCES

5.1 Mixing estimates from Thorpe-scale method

5.1.1 Distribution of turbulent overturns

The Thorpe-scale method is applied to 914 EM-APEX density profiles and detects a total of 3240 turbulent overturns. The largest mean number of turbulent overturns in each 3 m bin depth is found in the 100 to 400 m depth range, with as many as 25 turbulent overturns recorded at about 200 m (Figure 5.1a).

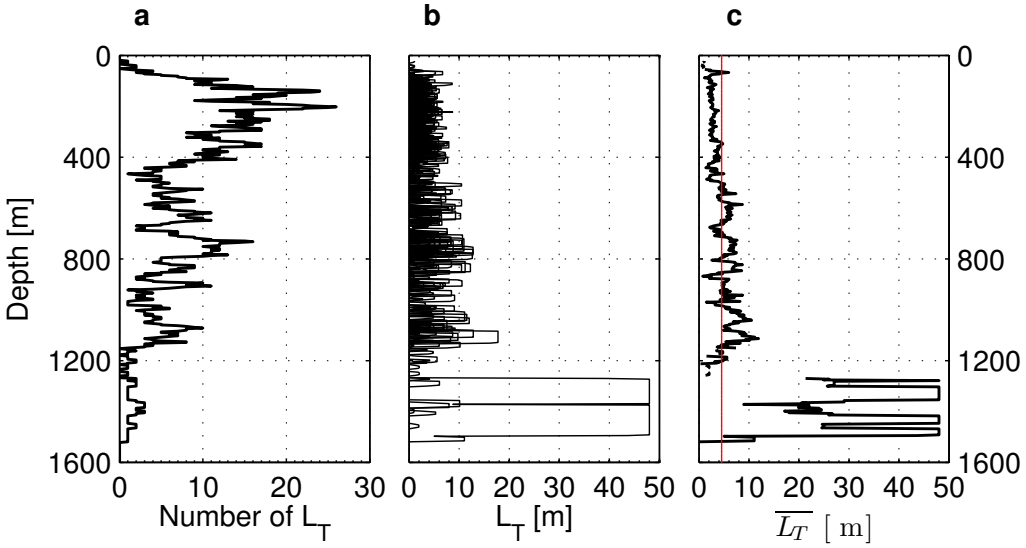

Figure 5.1: Vertical profiles as a function of depth of (a) the mean number of overturns in each bin depth; (b) the vertical distribution of all Thorpe scales; (c) the bin averaged profile of Thorpe scales (black line) and overall mean Thorpe scale value excluding Thorpe scales larger than 30 m (red line) for the Kerguelen Plateau.

On average for the Kerguelen region, the mean size of the Thorpe scales is 4.5 m (Figure 5.1c). The largest Thorpe scales are recorded in the deeper part of the data (1300 to 1600 m), which also corresponds to the depth range with a minimum of turbulent overturns detected (Figure 5.1a). The 48 m Thorpe scales observed twice in profile 289 (float 3761) are at a depth of 1500 m, which is the maximum depth of profiles (Figure 5.1b,c and 5.2). For that profile, the float is in the vicinity of a very shallow ridge with water depth

less than 1600 m. These profiles are taken in the bottom boundary layer and thus, the extreme Thorpe scales are most likely estimates of bottom boundary layer turbulence.

The evolution of the Thorpe scales (L_T) along the trajectory of the EM-APEX floats is shown in Figure 5.2, where L_T is plotted as a constant over the vertical extent of each turbulent overturn.

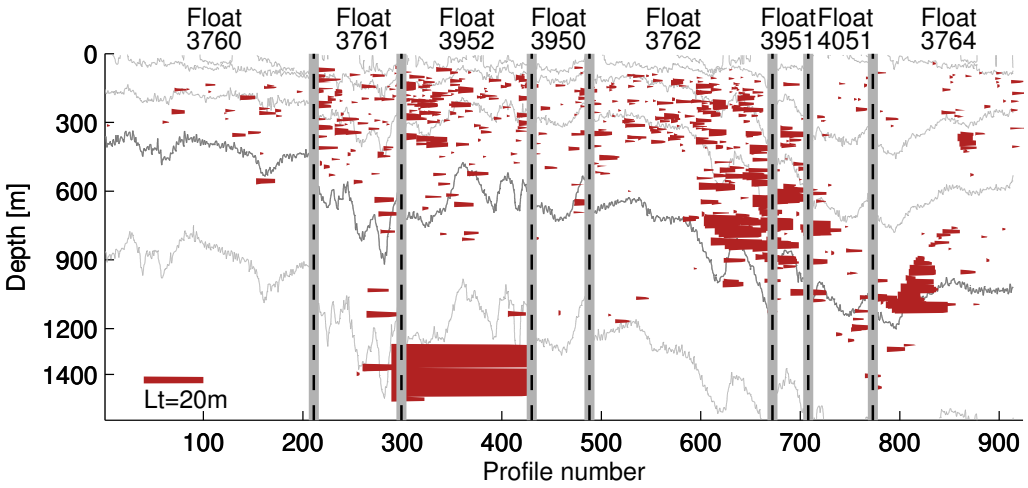

Figure 5.2: Estimates of Thorpe scales [m] derived from density with a noise level of 0.002 kg m^{-3} (red). Each spike corresponds to a turbulent patch where the horizontal length of the spike is equal to L_T. Potential density contours (σ_θ =26.1, 26.4, 26.7, 27.0, 27.3 in bold and 27.6 kg m^{-3}) are shown in grey. The vertical dashed lines separate floats.

Thorpe scale values range from 0.1 m to 48 m. The overall distribution is highly spatially variable, both in the vertical and horizontal, with some areas totally free of turbulent overturns and others with intense activity. Floats 3760 and 3950 show weak turbulent overturns while float 3952, 3762 and float 3764 have large turbulent overturns below 700 m.

5.1.2 Mixing intensity

The overall mean diapycnal diffusivity (K_ρ) for the region estimated with the Thorpe scale method is 9×10^{-5} m^2 s^{-1}. The spatial distribution of diapycnal diffusivity is highly variable. Diapycnal diffusivity values span approximately

four orders of magnitude ranging from 8×10^{-5} to $2 \times 10^{-1}\,\mathrm{m^2\,s^{-1}}$. Float 3761 shows evidence of enhanced mixing at depth (profile 289) with the highest diapycnal diffusivity values of this study, likely due to bottom boundary layer turbulence as explained previously. With overall mid-depth ocean interior diapycnal diffusivity values typically of O(10^{-5}) in the Southern Ocean (Ledwell et al., 2011), the estimated mixing rates are larger than typical open-ocean background levels. Yet the estimated mixing only occasionally exceed enhanced values ($K_\rho \geqslant 10^{-4}\ \mathrm{m^2\,s^{-1}}$) observed above rough topography elsewhere in the Southern Ocean (Ferron et al., 1998; Heywood, K. J. and Garabato, A. C. N. and Stevens, D. P., 2002; Naveira Garabato et al., 2004; Sloyan, 2005).

5.1.3 Resolution of Thorpe scales

Applying the Thorpe-scale method to estimate mixing requires either the presence of large density overturns or the use of precise instruments with high vertical resolution. Our ability to detect turbulent overturns in the density profiles is constrained by the vertical resolution of the CTD (sampling) and the density resolution of the CTD (instrument accuracy or noise level). The parameter R can be used to determine whether it is the density resolution or the vertical sampling resolution that limits the resolvable density inversions (Stansfield et al., 2001; Johnson and Garrett, 2004). R is defined as

$$R = \frac{d\rho}{dz}\frac{\triangle z_{inst}}{\triangle \rho_{inst}}, \tag{5.1}$$

where $d\rho/dz$ is the background density gradient, $\triangle z_{inst}$ is the vertical sampling resolution and $\triangle \rho_{inst}$ is the density resolution of the instrument. If $R > 1$, the vertical sampling resolution is the limiting factor while if $R < 1$, the instrument resolution limits the detection of density inversions. We assume a background density gradient $\frac{\overline{d\rho}}{\rho dz} \approx 7 \times 10^{-4}\ \mathrm{m^{-1}}$, an average vertical sampling resolution of 2.5 m and a density resolution of $0.0019\,\mathrm{kg\,m^{-3}}$. For the CTD on the EM-APEX, we find $R = 0.92$, which is very close to 1, suggesting that both the density resolution of the instrument and the vertical sampling resolution are equally limiting the detection of density inversions.

We investigate whether the resolution limitations of the EM-APEX lead to significant underestimates of the presence of density inversions and therefore biased mixing estimates. The distribution of the Thorpe scales is relatively lognormal (Figure 5.3a and 5.3b). This is expected since Thorpe scales are theoretically the result of a multiplicative series of independent events (Stansfield et al., 2001).

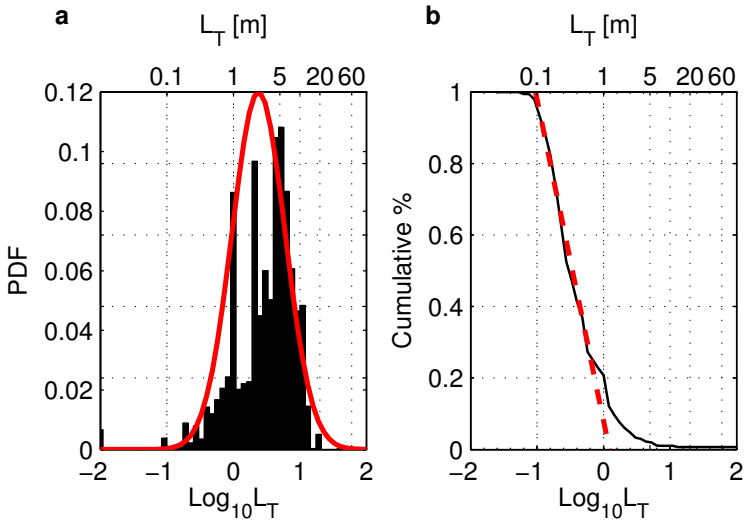

Figure 5.3: Thorpe-scales statistics for the EM-APEX profiles: (a) histogram of the probability density function of log Thorpe scale ($log_{10}(L_T)$) computed from all 3240 turbulent overturns identified in this study. Data are binned into 51 bins spanning $-2 \leqslant log_{10}(L_T) \leqslant 2$ m for this calculation. The red line is a Gaussian fit assuming a lognormal distribution. (b) cumulative probability plot of $log_{10}(L_T)$ integrating from large to small scales (black line). The dotted red line is an indication of the linearity of the cumulative probability. Note that the two extreme 48 m Thorpe scales observed near bottom boundary layer (Float 3761, profile 289) are not included in this statistical analysis since they are not representative of the true population, where true population is in stratified ocean only.

The comparison with a Gaussian fit (red curve on Figure 5.3a) suggests that the EM-APEX floats are resolving only 50% of the Thorpe scales. The occurrence of $L_T = 0$ has not been plotted in the histogram, or in the cumulative probability plots. The cumulative probability plot (Figure 5.3b), which would be linear if the Thorpe scale distribution was lognormal, shows

a linear distribution between 20% and 99% cumulative probability. The sampling and bin averaging of the CTD data prevents the CTD from resolving small Thorpe scales, which are thought to be more frequent in the normal distribution (Stansfield et al., 2001). As a result we do not sample the peak in the distribution, which takes place between 1 and $5m$.

Conclusion

The Thorpe-scale method is applied to estimate turbulent mixing north of the Kerguelen Plateau. In the upper 1600 m, the mean diapycnal diffusivity is estimated at $9 \times 10^{-5}\,\mathrm{m^2\,s^{-1}}$, suggesting that mixing rates around the Kerguelen Plateau are slightly enhanced compared to background diapycnal diffusivity in the Southern Ocean. Although this method provides an overview of the distribution of turbulent overturns north of the Kerguelen Plateau, it is limited by the instrument's resolution and sampling characteristics. We conclude that the application of the Thorpe-scale method to estimate ocean mixing is not appropriate for the EM-APEX data.

5.2 Mixing from shear-strain parameterization

In this section we present diapycnal mixing estimates from the shear-strain parameterization which combines finescale measurements of internal wave-scale shear and strain with theoretical models of energy transfer (see Chapter 4.1.2). Applying this technique to the EM-APEX float data we can analyse along stream variations in diapycnal mixing between 200 and 1400 m (see Section 4.2.3). By combining these mixing estimates with the hydrography we collected and other environmental parameters, we will provide insight into potential drivers of this mixing.

5.2.1 Spatial distribution and intensity of mixing

The overall mean dissipation rate determined by the shear-strain parameterization for the region is of $9 \times 10^{-10}\,\mathrm{W\,kg^{-1}}$ with a 90% confidence interval of $1 \times 10^{-11}\,\mathrm{W\,kg^{-1}}$ and $3 \times 10^{-9}\,\mathrm{W\,kg^{-1}}$ and the mean diapycnal diffusivity is $3 \times 10^{-5}\,\mathrm{m^2\,s^{-1}}$ with a 90% confidence interval of $4 \times 10^{-7}\,\mathrm{m^2\,s^{-1}}$ and $10 \times 10^{-5}\,\mathrm{m^2\,s^{-1}}$ using the standard deviation technique (Figure 5.4 a and b). It is generally assumed that the dissipation rate in the open ocean at mid- and low-latitudes is $\mathrm{O}(10^{-10})\,\mathrm{W\,kg^{-1}}$ (St. Laurent et al., 2012a), putting our mean dissipation rate at background levels.

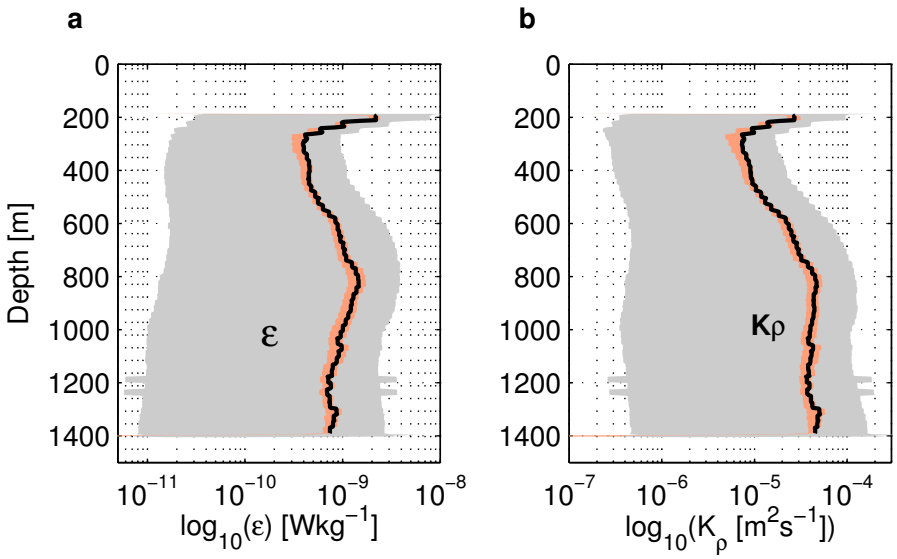

Figure 5.4: Mean vertical profiles of the EM-APEX data as a function of depth of (a) dissipation rate (ϵ) and (b) diapycnal diffusivity ($K\rho$) estimated using the shear-strain parameterization. Shaded area shows the 90% confidence intervals computed via standard deviation from the mean (grey) and via bootstrap sampling (red); see Section 4.2.3 for details.

We find that vertically averaged K_ρ north of the Kerguelen Plateau is highly spatially variable in the EM-APEX data and most intense over shallower bathymetry (Figure 5.5). These values are similar to other finescale parameterization observations in the Southern Ocean (Wu et al., 2011) and microstructure measurements in the area (Waterman et al., 2013).

For each EM-APEX profile, the topographic roughness is computed over a 0.1° longitude by 0.1° latitude box (Figure 5.6 bottom panel) using the Smith and Sandwell (Smith and Sandwell, 1997) topography data set (Section 2.3.1). Topographic roughness (var(H) m^2) is defined as the variance of bottom height (H) in a certain wavenumber range. Note that the spatial resolution of the topography data set is likely only resolving part of the scales of the internal wave generation radiative range (Nikurashin and Ferrari, 2011). Higher resolution topographic data would be more appropriate to derive topographic roughness for the purpose of this study.

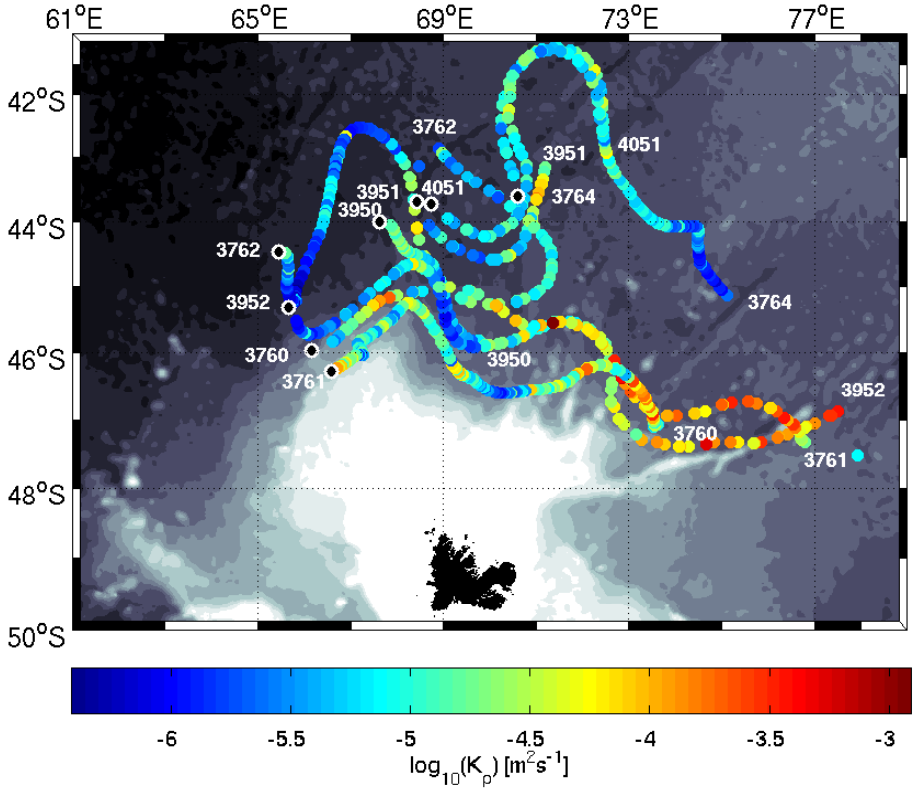

Figure 5.5: Horizontal distribution of the vertically averaged (200 to 1400 m) diapycnal diffusivity (K_ρ) from shear-strain parameterization. Topography contours range from 200 to 5000 m at 400 m intervals (grey). Float numbers are indicated as well as the first profile of each float (black dot).

Values of K_ρ also show large vertical variability (Figure 5.6) and diapycnal diffusivity can vary by as much as four orders of magnitude in one profile. A

few regions show particularly weak diapycnal diffusivities of $O(10^{-6}\ \mathrm{m^2\,s^{-1}})$, other regions show enhanced diapycnal diffusivity values of $O(10^{-3})\ \mathrm{m^2\,s^{-1}}$ below 600 m in the vicinity of rough topography (approximately profiles 170, 290, and 420) and the upper ocean of $O(10^{-4})\ \mathrm{m^2\,s^{-1}}$ (top 200 m, approximately profiles 700 to 840) (Figure 5.6).

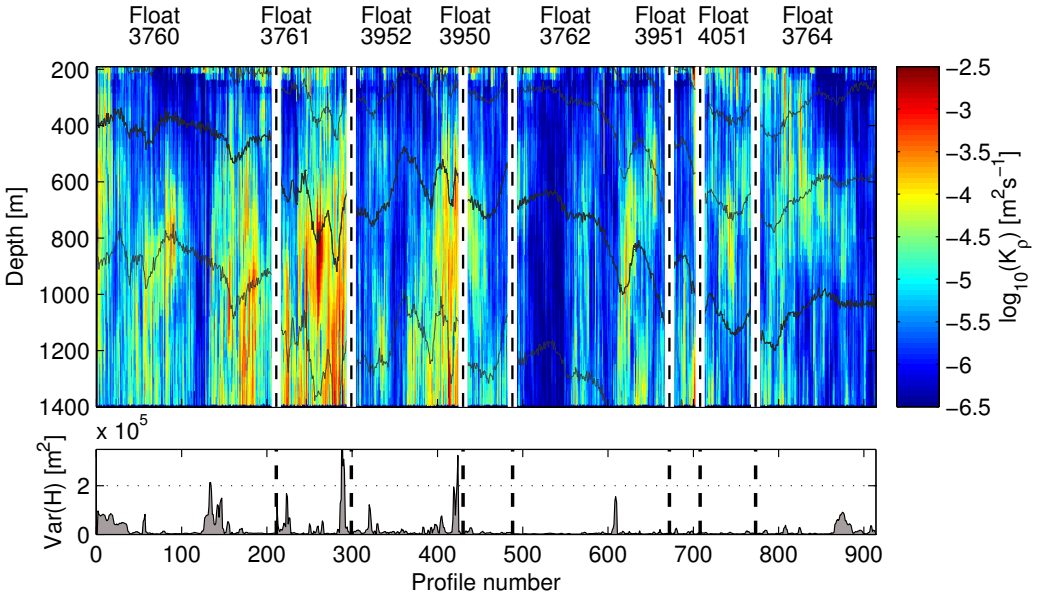

Figure 5.6: Vertical distribution of K_ρ (top) along the trajectories of the eight EM-APEX floats. Potential density contours (σ_θ =26.7, 27.0, 27.3 (bold) and 27.6 $\mathrm{kg\,m^{-3}}$) are shown in black. The vertical dashed lines separate floats. Bottom panel indicates the topographic roughness (var(H)).

5.2.2 Investigation of mixing sources

In this section, we investigate topographic roughness, current speed, eddy dynamics and wind speed as sources of mixing in the EM-APEX data north of the Kerguelen Plateau. To do so, we subsample the data into dynamical regions: profiles that are located in a region of geostrophic flow speed larger than $0.35\ \mathrm{m\,s^{-1}}$ are considered to be inside the SAF/STF front, hereinafter referred to as the Front. The rest of the profiles are assigned to either the region north of the Front (Subantarctic Zone), to the region south of the Front

(Polar Front zone) or to the eddy. About half of the profiles are labelled as in the Polar Front Zone (468 profiles), nearly a quarter are in the Front (208 profiles), 94 are in the Subantarctic Zone and 144 in the eddy.

Mixing and topography

To investigate the impact of topography on the mixing intensity and distribution, we estimate the topographic roughness for each profile (Figure 5.7 b) and the depth-integrated turbulent production, $\mathcal{P}$ [W m^{-2}]

$$\mathcal{P} = \rho_\theta (1 + R_f) \int \epsilon dz. \tag{5.2}$$

The dissipation rate (ϵ) is inferred from the observations using the shear-strain parameterization, $\rho_\theta = 1027$ kg m^{-3} is the background potential density and $R_f = 0.17$ is the flux Richardson number (Peltier and Caulfield, 2003). The turbulent production integrated over the total sampling depth range (200 to 1400 m) varies strongly from profile to profile (Figure 5.7 a).

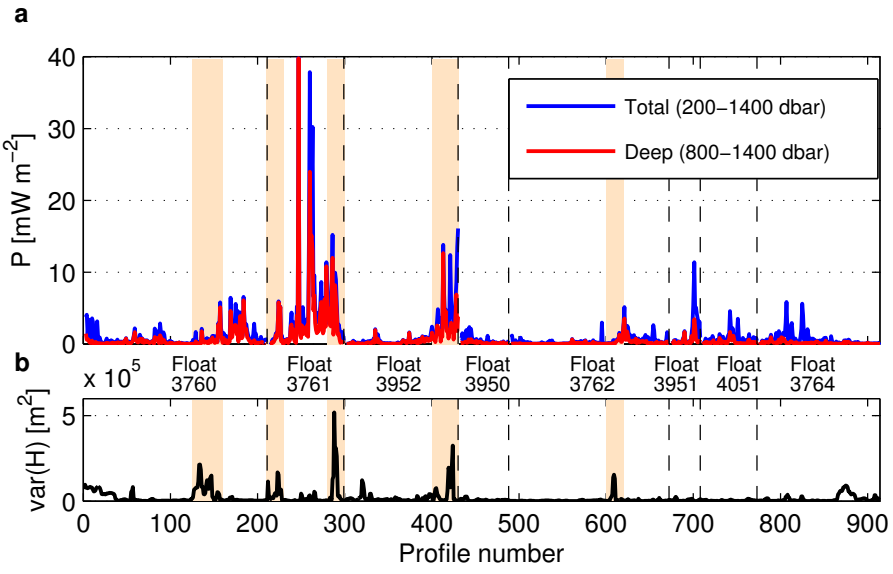

Figure 5.7: a) Depth integrated turbulent production ($\mathcal{P}$) for each profile with b) local topographic roughness, var(H), for each profile. Profiles with local topographic roughness larger than mean value are shaded (beige).

The regional mean value of turbulent production in the upper 1600 m (1.23 mW m^{-2}) fits in the range of 1-10 mW m^{-2} estimated by Waterman et al. (2013) in the same region for the upper 1500 m and larger than the equivalent background depth-integrated GM turbulent production (0.7 mW m^{-2}). Peaks in turbulent production in the total depth range are clustered in certain regions (profiles 220 to 300 and 380 to 420, for example). Regions showing enhanced production in the total depth range also show enhanced power in the deeper part of the profile (Figure 5.7a). Peaks in production in the deep depth range also often coincide with regions of enhanced topographic roughness (Figure 5.7b). The mean integrated turbulent production for profiles south of 46°S, closer to the Kerguelen Plateau, reaches 2.6 mW m^{-2}. This suggests that a significant amount of the enhanced turbulent production in the water column is due to intense energy dissipation at depth and that topographic roughness around the Kerguelen Plateau is a dominant driver of enhanced energy dissipation in the area. Areas of enhanced production that are not matched with rough topography (around profile 700 for example) will be investigated in subsequent sections.

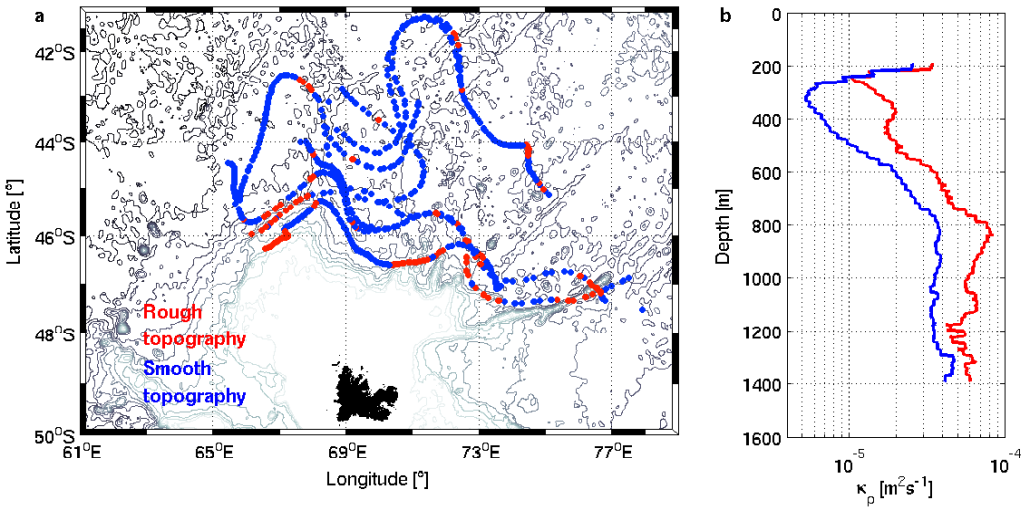

Figure 5.8: **a**, Map of profiles above rough topography (red) and smooth topography (blue). **b**, Mean vertical diapycnal diffusivity profile as a function of depth above rough topography (red) and smooth topography (blue).

To quantify the impact of the local topography on the mixing intensity,

we subsample the data set into profiles above smooth topography and profiles above rough topography (Figure 5.8 a). Smooth topography is defined as regions with values of roughness less than $1.72 \times 10^4\,\mathrm{m}^2$ and rough topography as regions with values of roughness larger than $1.72 \times 10^4\,\mathrm{m}^2$. This critical value that separates smooth and rough topography is the mean roughness for the EM-APEX data. The majority of the profiles sampled above rough topography are located south of $45°S$, closer to the Kerguelen Plateau (Figure 5.8a). The mean vertical stratification and horizontal velocity profiles are similar whether above smooth or rough topography (not shown). The mean vertical mixing profiles for each subsample show that diapycnal diffusivity is up to three times more intense above rough topography than above smooth topography (Figure 5.8 b). The rough profiles show enhanced diapycnal diffusivity from 240 m to 1400 m, with maximum near 800 m. The water column above rough topography in this study is on average 2900 m deep. This suggests that the impact of the topography on mixing in this study can reach up to 2000 m above the seafloor, as previously reported in the Brazil Basin (Polzin et al., 1997).

We observe a significant correlation of $R = 0.74$ ($P < 0.05$ at the 95% confidence interval) between the depth integrated diapycnal diffusivity over the total profile range and topographic roughness (Figure 5.9). This correlation is much higher than previous estimates for the Southern Ocean ($R = 0.51$ Wu et al., 2011). The linear fit between the diapycnal diffusivity and the topographic roughness has a slope of 0.58.

The enhanced mixing above topographic roughness is likely due to internal wave generation and dissipation where the strong quasi-steady flow of the ACC interacts with the topography (Bell, 1975). Recent studies have shown that geostrophic motions dominate energy conversion into internal waves in the Southern Ocean (Nikurashin and Ferrari, 2013), while global estimates of M_2 tidal energy dissipation from various data sources show little tidal dissipation north of the Kerguelen Plateau (Egbert and Ray, 2000). With most of our data sampled north of the Kerguelen Plateau in water deeper than 2000 m, it is likely that the geostrophic flow, rather than tidal motion, is the source of the internal waves. Similar cases of enhanced mixing above topo-

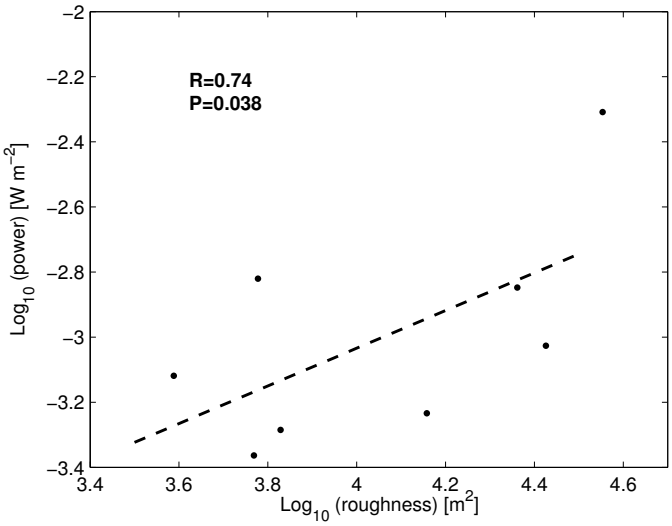

Figure 5.9: Depth integrated diapycnal diffusivity vs. topographic roughness with one data point for each float. The dashed line shows the linear fit. The correlation coefficient (R) and p-value (P) are indicated.

graphic roughness have been observed in the Southern Ocean: in the Drake Passage (Naveira Garabato et al., 2004) and Scotia Ridge (Naveira Garabato et al., 2004; Damerell et al., 2012; Sheen et al., 2013); but also in the South Atlantic Ocean Brazil Basin (Polzin et al., 1997), along the path of the ACC (Sloyan, 2005), in the Nordic seas (Naveira Garabato et al., 2004), in the northwestern Pacific (Jing and Wu, 2010) and in the Indian Ocean (Sloyan, 2006).

Mixing and the Subantarctic Front

A front is a region of sharp transitions of ocean properties and is therefore likely to have different mixing dynamics than surrounding regions. Previous studies in the Southern Ocean have shown frontal regions acting as a boundary between different mixing regimes (Thompson et al., 2007) as well as enhancing mixing along the ACC pathway (Sloyan, 2005).

Using the horizontal velocity data from the EM-APEX floats as well as available weekly surface geostrophic speed maps (not shown), we identify the location of each profile as either in the Subantarctic Zone, in the Front

(SAF/STF) or in the Polar Front Zone. The profiles in the eddy first described in Section 3.1, are not included because the eddy's dynamics differ from dynamics outside the eddy, as will be demonstrated in the Section 5.2.2.

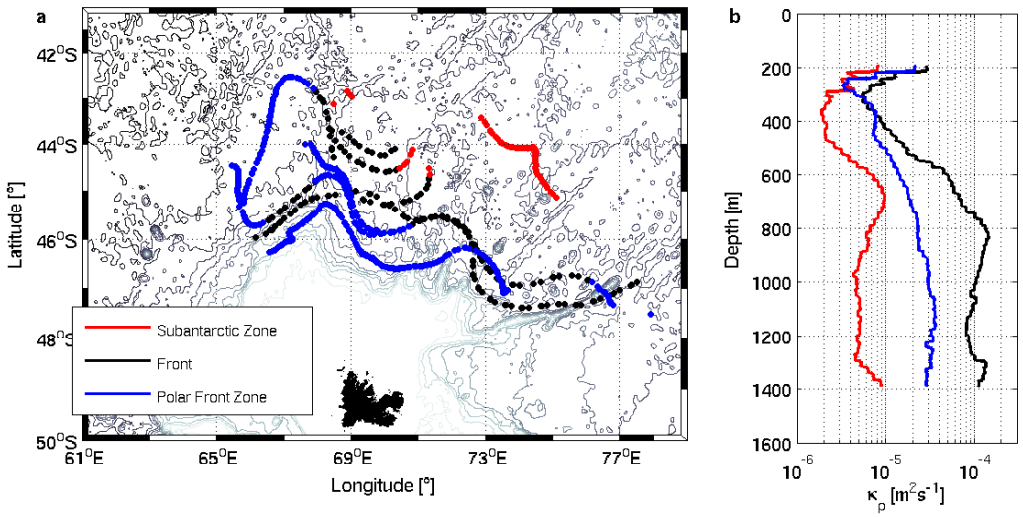

Figure 5.10: **a)** Map of profiles located in the Subantarctic Zone (red), in the Front (black) and in the Polar Front Zone (blue). **b)** Mean vertical diapycnal diffusivity profile as a function of depth in the Subantarctic Zone (red), in the Front (black) and in the Polar Front Zone (blue).

The mean mixing intensity and vertical distribution in the Subantarctic Zone, in the Polar Front Zone and within the Front differs by over an order of magnitude in most of the water column (Figure 5.10 b). Overall, mixing is much more intense within the Front than in the Subantarctic Zone or in the Polar Front Zone. While the weakest mixing is in the Subantarctic Zone, in the Polar Front Zone we observe slightly less enhanced mixing from that in the Front region. All three regions reach a maximum mixing value below 700 m, while subsurface minima are located between 250 and 450 m.

In terms of hydrography, the water in the Subantarctic Zone is warmer, more saline and lighter; the water in the Polar Front Zone is cooler, less saline and denser, while the water in the Front has intermediate characteristics (Figure 5.11 a). The mean stratification profile is very similar for all three regions. The current speed is greatly enhanced in the Front throughout the water column compared to the Subantarctic Zone and the Polar Front Zone

(Figure 5.11 b and c). Mean values of parameters in the Polar Front Zone, within the front and in the Subantarctic Zone are summarised in Table 5.1.

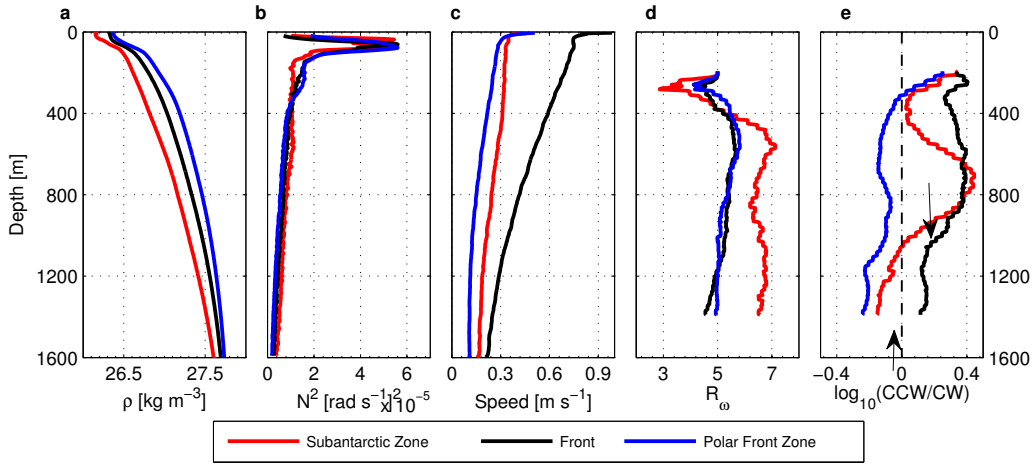

Figure 5.11: Mean vertical profiles as a function of depth of **a)** potential density (ρ_θ), **b)** stratification (N^2), **c)** current speed, **d)** shear-to-strain variance ratio (R_ω) and **e)** log of ratio of rotary with depth shear variance (ϕ_{CCW}/ϕ_{CW}) in the Subantarctic Zone (red), in the front (black) and in the Polar Front Zone (blue). The arrows represent the direction of energy propagation.

The mean shear-to-strain variance ratio (R_ω) profile is very similar in the Front and in the Polar Front Zone, but the mean R_ω values in the Subantarctic Zone below 400 m are higher (Figure 5.11 d). This suggests that near-inertial frequency waves dominate in the Subantarctic Zone (see Section 4.2.3). Finally, the ratio of rotary-with-depth shear variance (ϕ_{CCW}/ϕ_{CW}), which is used to distinguish upward from downward energy propagation (see Section 4.2.3), varies substantially from one region to another. In the Front, the ϕ_{CCW}/ϕ_{CW} ratio is greater than one throughout the water column, implying mostly downward propagating internal waves. In contrast, in the Polar Front Zone, with ϕ_{CCW}/ϕ_{CW} ratio values less than one below 300 m, most of the energy comes from upward propagating internal waves (Figure 5.11 e).

We identify two key parameters to explain the enhanced mixing observed in the Front: intense current speed and rough topography. In the Polar Front Zone, the upward propagating internal wave signature indicates that

Parameter	Polar Front Zone	Within Front	Subantarctic Zone
Diffusivity ($m^2\,s^{-1}$)	2×10^{-5}	6×10^{-5}	0.5×10^{-5}
Current speed ($m\,s^{-1}$)	0.17	0.44	0.15
Shear (s^{-1})	1.5×10^{-4}	3.5×10^{-4}	1×10^{-4}
topographic roughness (m^2)	1.9×10^4	2×10^4	1.8×10^4
shear-to-strain ratio	5.2	5.1	6.2
ϕ_{CCW}/ϕ_{CW} ratio	0.9	1.3	1.1
Wind stress ($N\,m^{-2}$)	1.33	1.54	1.97

Table 5.1: Mean parameter values in the Polar Front Zone, within the Front and in the Subantarctic Zone. Details about the wind stress estimates are provided in Section 2.3.2.

the source of the waves that generate mixing is mainly from the sea floor. We suggest that the main mixing mechanism in that region is the interaction of the current flow with topography, but lower current speeds give rise to smaller mixing than in the Front. Finally, the combination of higher wind stress values, downward propagating internal waves and inertial frequency waves (Table 5.1) implies that wind forcing is the primary driver of the mixing observed in the Subantarctic Zone. Wind as a source of mixing will be further investigated in Section 5.2.2.

To assess the quantitative impact of the Front on the mixing intensity, we estimate the correlation between the depth integrated diffusivity and the mean current speed in the upper 1400 m, assuming that higher mean current speed is a good proxy for the Front. Over the whole data set, the moderate positive correlation ($R = 0.36$) confirms that as current speed increases over rough topography, so does mixing. Since the enhanced mixing due to the Front is likely located closer to the seafloor, we expect stronger correlation in shallower regions of the study area where our data cover more of the water column. We choose the mean water depth (3546 m) over $41°S - 50°S$

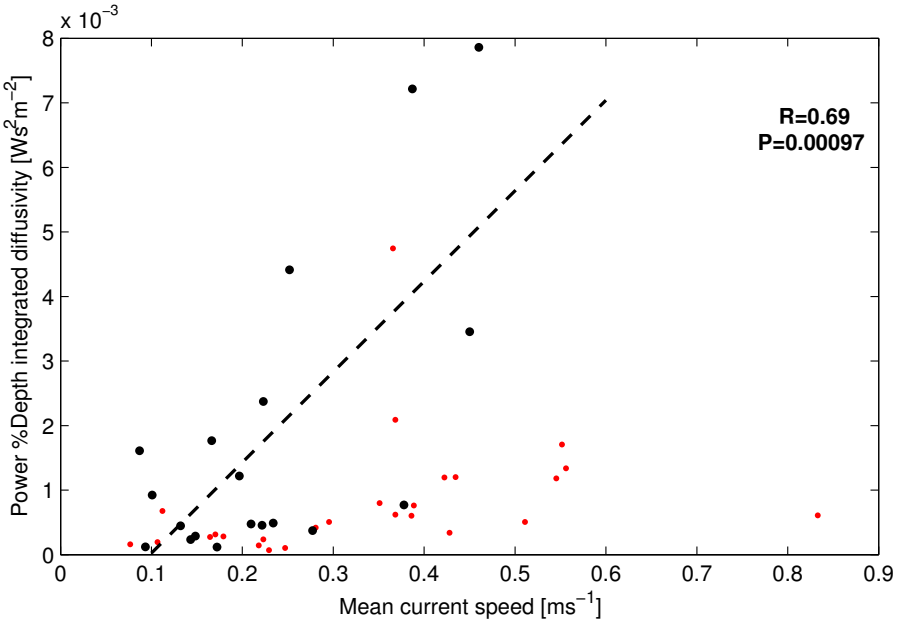

Figure 5.12: Depth integrated diffusivity vs. mean current speed in shallower water (black) and in deeper water (red). The dash line shows the linear fit for the shallower water data. The correlation coefficient (R) and p-value (P) are indicated.

and $61°E - 79°E$ as the threshold between shallower and deeper water and correlate current speed and depth integrated diffusivity only in the shallower water (Figure 5.12). The resulting correlation is much stronger $R = 0.69$ ($P < 0.0002$ at the 95% confidence interval), confirming the presence of enhanced mixing at depth when the current speed is high.

Mixing in the eddy

We identify profiles located along the rim of a cyclonic (clockwise) eddy (Section 3.1) using weekly surface geostrophic speed maps. These profiles are in a geostrophic flow with speed larger than $0.35\,\mathrm{m\,s^{-1}}$ but are not along the main axis of the Subantarctic Front (Figure 3.1). Strong mixing values in the top 400 m that are up to 20 times larger than mixing elsewhere in the area differentiates the eddy from the Front (Figure 5.15).

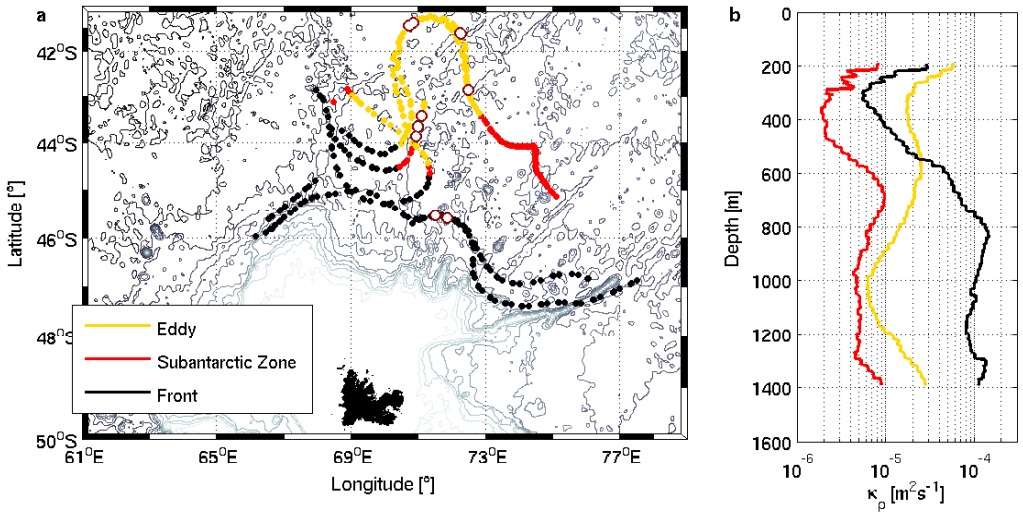

Figure 5.13: **a)** Map of profiles located in the eddy (brown), in the Subantarctic Zone (red) and in the Front (black). **b)** Mean vertical diapycnal diffusivity profile as a function of depth in the Subantarctic Zone (red), in the eddy (brown) and in the Front (black). Profiles with extremely high surface integrated diapycnal diffusivity values are highlighted (white dots).

Overall, the eddy rim has the same temperature, salinity and density characteristics as waters in the Subantarctic Zone, while its current speed is

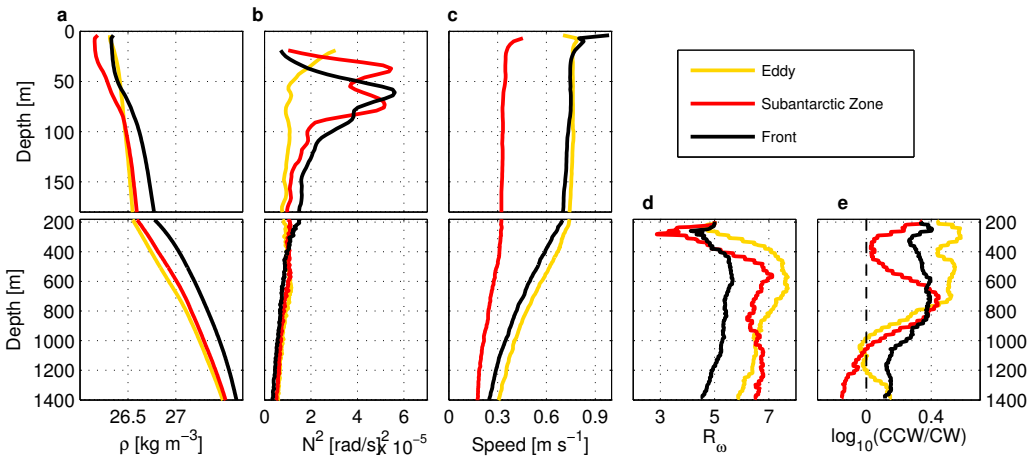

Figure 5.14: Mean vertical profiles as a function of depth for **a)** potential density (ρ_θ), **b)** stratification (N^2), **c)** current speed, **d)** shear-to-strain variance ratio (R_ω) and **e)** log ϕ_{CCW}/ϕ_{CW}, in the eddy (brown), in the Subantarctic Zone (red) and in the Front (black). Upper plot corresponds to mixed-layer; lower plot from mixed-layer to 1400 m

much higher than profiles in the Subantarctic Zone. Velocity shear is lower in the eddy than in the Front (Figure 5.14). The stratification in the top 200 m is lower in the eddy rim than in either the Front or in the Subantarctic Zone (Figure 5.14 b). The eddy exhibits high mean shear-to-strain variance ratio (R_ω) in the upper 1000 m (Figure 5.14 d) and high values of CW to CCW rotating shear variance in the upper 800 m (Figure 5.14 e). This suggests that near inertial frequency waves dominate the upper part of the water column and that there is downward internal wave energy propagation.

The evolution in time of parameters in the Front, in the eddy and in the Subantarctic Zone (Figure 5.15), shows that the high mean surface mixing (200 to 400 m) observed in the eddy is due to 12 profiles with extremely high surface integrated diapycnal diffusivity values (Figure 5.15 a). These profiles were sampled over a two week period by three different EM-APEX floats in different sections of the eddy (Figure 5.13). Lower stratification values are observed in some of the eddy profiles as well as in some of the Front profiles (Figure 5.15 b) but there is no apparent relationship between stratification and the profiles with high dissipation. The shear-to-strain variance ratio

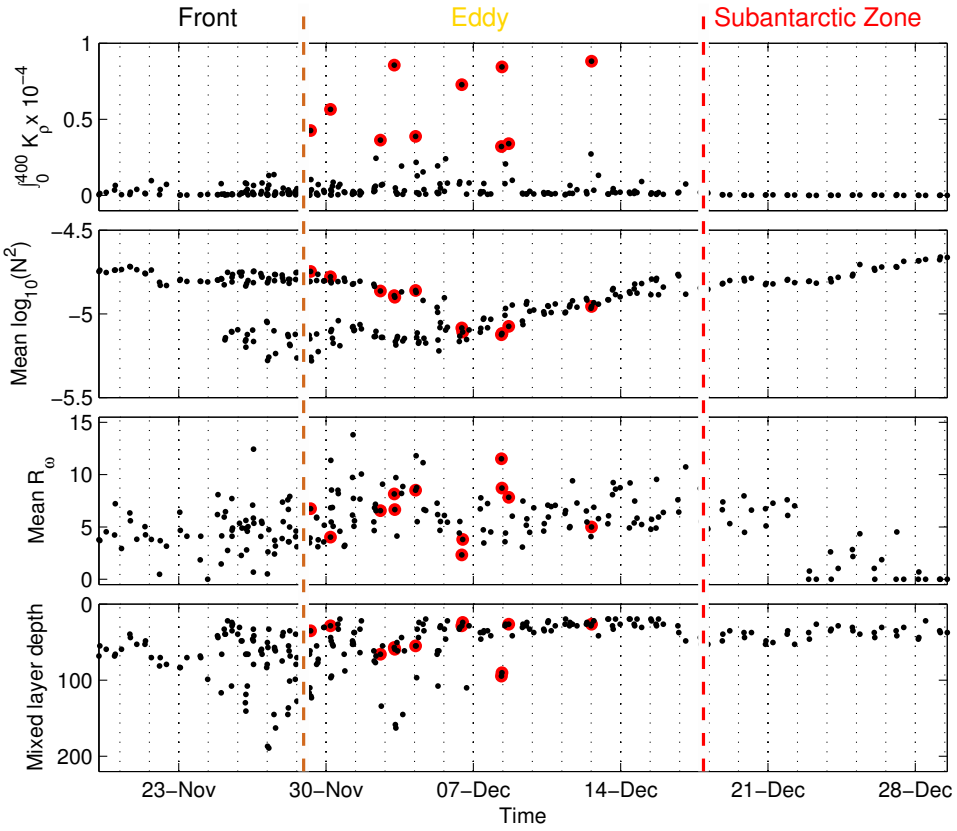

Figure 5.15: Time evolution of a profile subset sampled between 19/11/2008 and 30/12/2008 of **a)** vertically integrated diapycnal diffusivity ($K\rho$) between 200 and 400 m, **b)** vertical mean stratification (N^2) in top 400 m, **c)** mean shear-to-strain variance ratio (R_ω) in top 400 m and **d)** mixed-layer depth [m]. The two vertical dash lines separate profiles by regions in which they were sampled (front, eddy or Subantarctic Zone). 12 profiles with high surface integrated diapycnal diffusivity are highlighted (red points).

(R_ω) displays substantial variability amongst profiles in the Front and in the eddy (Figure 5.15 c). Enhanced mixing in the upper water column is often attributed to wind forcing. Under certain circumstances, wind stress generates vertical inertial motions at the ocean surface, which can propagate downwards before dissipating and releasing their energy as mixing. For wind stress to efficiently force inertial motions in the surface mixed-layer, wind variability must be at the inertial frequencies and aligned with the flow field.

In this study, strong wind forcing events could explain the change in stratification, the deepening of the mixed-layer and the larger magnitude of the variation of the shear-to-strain variance ratio observed prior to the peak in diffusivity in the upper part of the water column. It would also explain the presence of near inertial frequency waves in the upper part of the water column and the observed downward internal wave energy propagation (Figure 5.14).

Both observational (Elipot et al., 2010) and modelling (van Meurs, 1998; Balmforth and Young, 1999) studies have shown that near-inertial internal waves can decay more rapidly when exposed to strong relative vorticity gradients. Theory also suggests that wind-forced near-inertial internal waves are vertically amplified in regions of strong relative vorticity gradients, leading to a quick decay with time, wave breaking and enhanced local dissipation rate (Kunze, 1985). This "wave-trapping" can take place when internal waves are generated in eddies that have a large relative vorticity gradient. The fast vertical propagation is explained by the vertical group speed of the waves that depends inversely on the horizontal wavelength, shorter due to the strong relative vorticity gradient (Pedlosky, 2003). Jing and Wu (2013) found enhanced mixing particularly under anticyclonic eddies in the Northern Hemisphere, with dissipation rates twice as large in the upper 300 to 600 m. They invoked negative relative vorticity as the reason for the enhanced mixing. The depth at which the near-inertial internal waves are trapped and decay, called the critical-layer depth, depends on the intrinsic frequency of the near-inertial waves as well as the structure of the eddies. Brearley et al. (2013) also observed significant transfers of energy between eddies and internal waves resulting in enhanced dissipation rates.

Here we speculate that wind forcing events excited the generation of near-inertial waves at the ocean surface in both the Front and the eddy. The near-inertial internal waves generated by the wind in the eddy would be affected by the local relative vorticity gradient (Figure 3.8), leading to faster vertical propagation of those waves and therefore enhanced local dissipation rate. In contrast, the near-inertial internal waves generated by the wind in the Front would tend to be advected by the current and would therefore not result in enhanced local dissipation rate.

Wind driven mixing

The main mechanism to transfer energy from the wind to the ocean is the generation of near-inertial internal waves that radiate downward, break and release their energy as mixing. In this study, since we estimate mixing below 200 m, we can only identify wind-driven mixing below the mixed-layer depth. While the EM-APEX floats were sampling the Kerguelen Plateau region, atmospheric low-pressure systems associated with strong wind speeds came through the region (Figure 5.16).

To identify likely wind driven mixing areas, we first look at the ratio of rotary-with-depth shear variance, ϕ_{CCW}/ϕ_{CW} and the shear-to-strain variance ratio, R_ω. Higher values of ϕ_{CCW}/ϕ_{CW} suggest downward-propagating internal waves and higher R_ω values imply the presence of near-inertial waves (see Section 4.2.3 and 4.2.3).

The mean vertical distribution of ϕ_{CCW}/ϕ_{CW} ratio for profiles with high upper-layer turbulent production values shows that downward energy propagation prevails in the upper 1200 m (Figure 5.17 b). The mean vertical distribution of R_ω for profiles with high upper-layer turbulent production values shows enhanced values of R_ω in the top 600 m (Figure 5.17 c). This suggests that regions with high dissipation rate in the upper water column coincide with an increase in downward propagating energy and near-inertial waves. Next we compute the maximum wind area (A_{wind}) as a diagnostic for intense surface mixing events. A_{wind} is defined as the surface area [km^2] with wind speeds larger than 15 m s^{-1} within $41°S-48°S$ and $65°E-77°E$. The 15 m s^{-1}

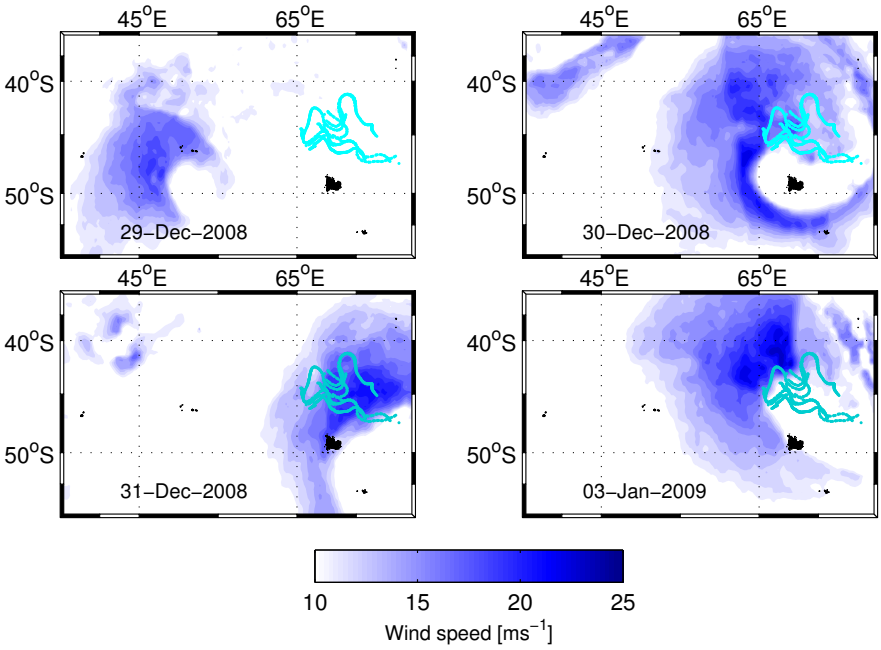

Figure 5.16: Evolution of an atmospheric frontal zone. Surface wind speed maps (colour scale) on four different days in the Kerguelen Plateau region with EM-APEX float trajectories (cyan). To identify atmospheric frontal zones, surface wind speeds below $10\,\mathrm{m\,s^{-1}}$ are not shown. Wind speed from blended CERSAT satellite data (Section 2.3.2).

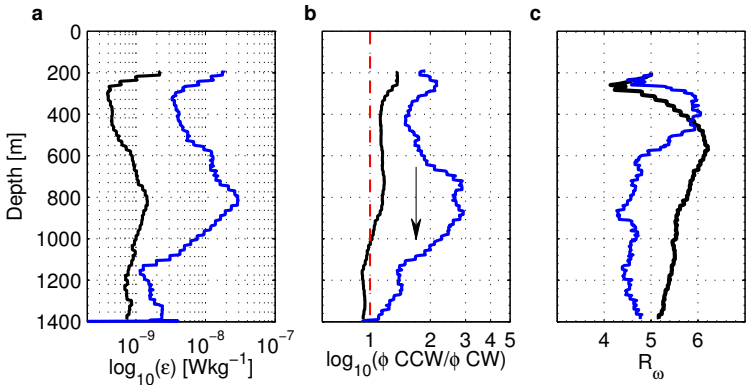

Figure 5.17: Mean vertical profiles as a function of depth of (a) dissipation rate ϵ, (b) ϕ_{CCW}/ϕ_{CW} and (c) shear-to-strain variance ratio (R_ω) as a function of depth over whole data set (black) and for profiles with high upper-layer turbulent production values (blue). ϕ_{CCW}/ϕ_{CW} values larger than one suggest downward energy propagation as indicated by the arrow.

threshold corresponds to the 99^{th} percentile of the wind field. Large values of A_{wind} should be associated with significant atmospheric frontal events passing through the region.

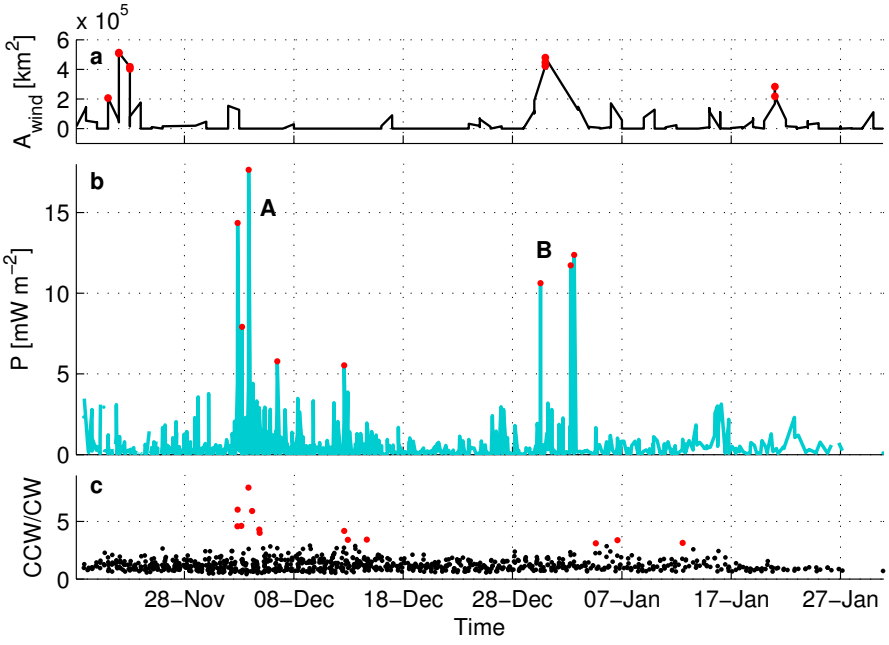

Figure 5.18: Subset time series between 18^{th} November 2008 and 31^{st} January 2009 of (a) maximum wind area (A_{wind}), (b) absolute value of the depth integrated dissipated upper water column turbulent production $\mathcal{P}$ (200 to 800 m) per unit area and (c) corresponding mean vertical ϕ_{CCW}/ϕ_{CW}. 'A' and 'B' identify events of intense depth integrated dissipated upper water column turbulent production. Values above the overall mean are highlighted (red).

Two main atmospheric frontal zones are observed, the first one taking place around the 23^{nd} November 2008, 9 days before a major peak in surface turbulent production (peak A) and the second taking place around the 31^{st} December 2008, just 3 days before peak B in surface turbulent production (Figure 5.18a). Peak A has already been identified and discussed in Section 5.2.2 where we speculated that near-inertial internal waves generated in the Front by a strong wind event are advected until they reach the eddy where the strong relative vorticity gradient triggers their local dissipation.

The observed delay (9 days) between the first atmospheric frontal zone

and peak A is consistent with this hypothesis. The second atmospheric frontal zone which triggered near immediate enhanced mixing in the surface layer is a cyclonic low pressure system (Figure 5.16). Note that the derived mean direction of each wind event is westward (not shown). After the passage of both atmospheric frontal zones, upper water column turbulent production reaches values well above average levels (Figure 5.18 b peaks A and B). The mean vertical ϕ_{CCW}/ϕ_{CW} ratio shows that turbulent production peaks (A and B) are associated with enhanced downward internal wave propagation (Figure 5.18c). The observed upper water column turbulent production ($O(1-10)$ mW m^{-2}) is similar in magnitude to regional estimates by Alford (2003) of wind energy into near-inertial motions.

To confirm the peaks in turbulent production are wind generated, we would ideally use local wind observations correlating wind stress or wind work with mixing observed in the upper ocean. Due to the lack of direct wind observations (from the floats, ship or flux mooring), we use satellite derived wind data (Section 2.3.2) that impose significant temporal and spatial limitations on our analysis. When comparing turbulent production in the surface depth range to the corresponding wind stress (τ_w), we find no direct correlation. The wind events responsible for enhanced mixing in the upper water column are not necessarily taking place in the time and space range that we correlate. Also, the six hourly time resolution of the wind data might not be resolving all the wind events variability.

We suggest some evidence of wind driven mixing below the mixed-layer and in the upper 600 m, in the form of downward propagating near-inertial internal waves. Work by Thompson et al. (2007); Sloyan et al. (2010) also found enhanced upper-ocean mixing north of the Front. These surface mixing events are attributed to large atmospheric frontal events, of which we identify two over the ten weeks of observations. The resolution of wind work estimates from satellite derived wind data is too coarse for correlations between wind work and mixing estimates.

5.3 Discussion

5.3.1 Method comparison

Comparison with direct observations of mixing

We compare the dissipation rate estimates from the EM-APEX floats with measurements from a microstructure profiler. Free-falling vertical microstructure profiler (VMP) measurements were collected during the SOFine survey in conjunction with the deployment of the EM-APEX floats. The microstructure data processing, dissipation rate and diapycnal diffusivity derived from the microstructure data are presented in Waterman et al. (2013).

EM-APEX and VMP dissipation rate profiles are within an order of magnitude and have a similar vertical structure indicating that the finescale parameterization applied to the EM-APEX data is appropriate (Figure 5.19). Note that the floats sampled water further north than the VMP, which was deployed along the cruise track (see Figure 2.3). Also, there are over 20 times more dissipation profiles in the finestructure mean profile than in the microstructure mean profile. The microstructure measurements, which make no assumption about mixing sources, and finescale parameterization estimates, which infers internal wave driven mixing only, agree well. Sources of mixing other than internal waves such as thermohaline intrusions (Ruddick and Richards, 2003) and double diffusion processes, might only play a minor role around the Kerguelen Plateau. In strong flows such as the flow we sampled, double diffusion cannot develop sufficiently to impact mixing. Taking into account the sampling differences and the uncertainties associated with the shear-strain finescale parameterization, it is remarkable that the dissipation rate estimates match as well as they do.

Potential limitations of the finescale parameterization method were identified by Waterman et al. (2013), where finestructure estimates from shipboard LADCP data over-predicted dissipation rates compared to microstructure rates within the bottom one kilometer in regions of internal wave generation. In our study, the EM-APEX data have a much higher vertical resolution (3 dbar) than LADCP data (20 dbar), making them more suitable for esti-

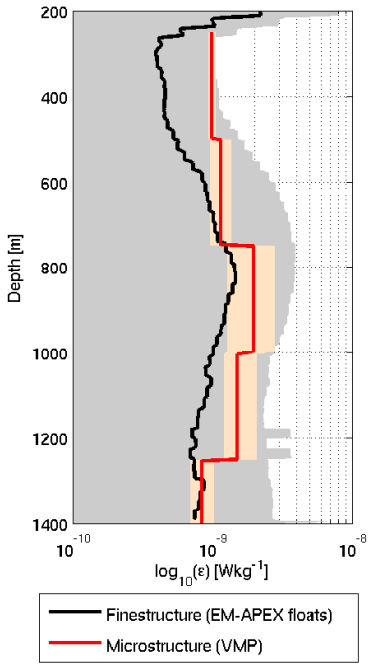

Figure 5.19: Mean vertical profile as a function of depth of finestructure (black) and microstructure (red) measurements of the dissipation rate (ϵ) as a function of depth. The shaded area denotes the 90% confidence intervals derived as the 1.644 standard deviations from the mean (grey) and by bootstrapping (red) respectively.

mating mixing rates. We resolve the cutoff wavenumber of the spectra used to estimate mixing and are therefore able to integrate the variance of the shear and strain at the correct wavelengths (Section 4.2.3). Also, the EM-APEX profiles are on average 2000 m off the seafloor, giving confidence in our mixing estimates.

Thorpe-scale method vs. shear-strain parameterization

As explained in Section 4.2.1, on large spatial and time scales, both the Thorpe scale and shear-strain parameterization methods should yield similar results. Turbulent mixing estimates from Thorpe scales and microstructure instruments have been shown to agree in previous studies (Ferron et al., 1998; Klymak et al., 2008). In this study however, mixing estimates from the Thorpe-scale method are limited by the instrument and small Thorpe scales are likely under-sampled. Even with the under-sampling of small Thorpe scales, we still obtain a similar overall mixing estimate with both methods ($9 \times 10^{-5}\,\mathrm{m^2\,s^{-1}}$ with Thorpe-scales and $3 \times 10^{-5}\,\mathrm{m^2\,s^{-1}}$ with shear-strain parameterization), which suggests that large Thorpe scales dominate the overall mean (Stansfield et al., 2001).

Both methods show a different mean vertical profile of turbulent diapycnal diffusivity (Figure 5.20a) and care needs to taken when interpreting those differences. There are only 2187 diffusivity estimates that go into estimating the mean diffusivity profile from Thorpe-scales while there are 500140 estimates of diffusivity to estimate the mean diffusivity profile from shear-strain parameterization. Since the Thorpe scales are not distributed randomly in the sample field (Figure 5.2b), the mean diffusivity profile from Thorpe-scales is biased towards regions where large Thorpe scales dominate. Throughout much of the water column, diapycnal diffusivity values derived using the Thorpe-scale method are larger by a factor of two than values derived using shear-strain parameterization. The difference between the two methods is greatest between 200 and 800 m and below 1200 m (Figure 5.20b). The Thorpe-scale method overestimate diapycnal diffusivity above 800 m with respect to the finescale parameterization, while between 800 and 1200 m, the

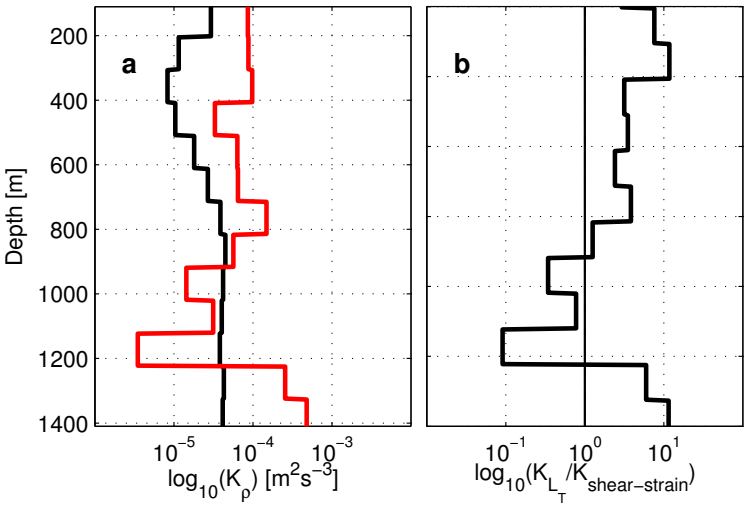

Figure 5.20: (a) Depth averaged profiles as a function of depth of diapycnal diffusivity (K_ρ) from the EM-APEX data using shear-strain parameterization (black) and Thorpe-scale parameterization (red). (b) Depth average profile of the ratio of diapycnal diffusivity derived from Thorpe-scales to those derived from shear-strain. Note that the shear-strain parameterization method limits the data to a range between 200 and 1400 m.

Thorpe-scale method underestimates diapycnal diffusivity. It might be that below 1200 m, the number of density overturns detected is too low to accurately represent the mean diapycnal diffusivity distribution (Figure 5.1a). We cannot tell how much of the difference between the mean diffusivity profiles is driven by potential limitations in the physics of the shear-strain parameterization method or by the resolution limitations of the Thorpe-scale method.

Even though the Thorpe-scale method has limitations in this data set due to instrument and vertical sampling resolution, both methods estimate similar mixing magnitude. Interpretations of the Thorpe-scale derived mixing values must take into account that the density data collected by the floats are biased in favour of larger turbulent overturns.

5.3.2 Topographic roughness vs. wind forcing

Overall, we identify roughness of the seafloor as the primary control of the mixing at depths deeper than 300 m. Wind forcing also plays a role in the mixing distribution, with evidence of wind driven mixing observed in the upper 600 m of the water column. In an attempt to separate the relative contributions to mixing by wind forcing and topographic roughness, we identify regions where upward and downward energy propagation dominates using $log_{10}(\phi_{CCW}/\phi_{CW})$ larger than 0.30 for downward energy propagation and $log_{10}(\phi_{CCW}/\phi_{CW})$ smaller than -0.25 as a threshold for significant upward energy propagation (Figure 5.21).

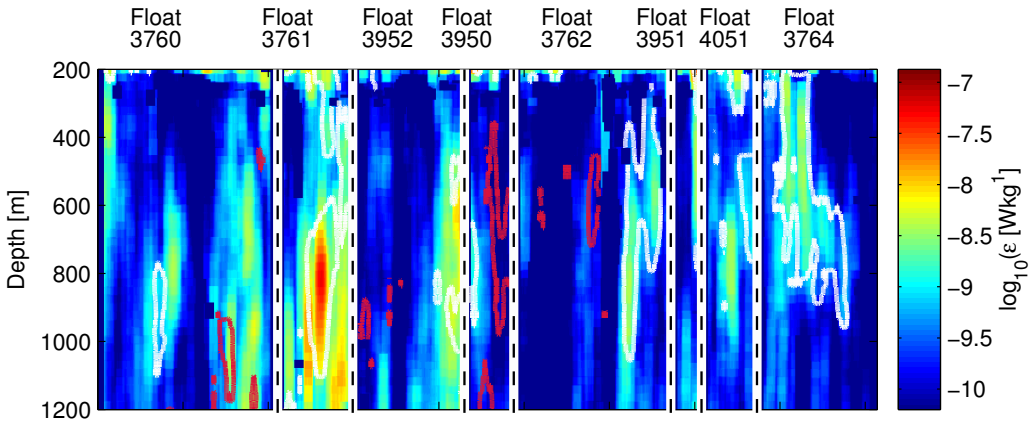

Figure 5.21: Vertical distribution of the smoothed dissipation rate (ϵ) along the floats' trajectories (colour scale) and contours of downward propagation (white contours) and upward propagation (red contours) ϕ_{CCW}/ϕ_{CW} values. The vertical dashed lines separate floats.

In the EM-APEX data, we find a total vertical area of 900 m^2 associated with downward energy propagation and a vertical area of 700 m^2 associated with upward energy propagation. Assuming that (1) dissipation associated with downward energy propagation is the result of surface generated internal wave breaking and (2) dissipation associated with upward energy propagation is the result of breaking internal wave generated over rough topography, we find that 37% of the dissipation rate observed has its origins at the surface while 6% originates at the seafloor. The remaining 57% of the estimated dis-

sipation rate is not within the thresholds for significant upward or downward energy propagation and we therefore cannot attribute it to either surface or seafloor origins. Note that this approach ignores other sources of downward and upward propagating internal waves as well as ignoring surface reflection and the given percentages are only indicative.

Regions with large values of ϕ_{CCW}/ϕ_{CW} match areas of high dissipation rate while regions with low ϕ_{CCW}/ϕ_{CW} values fail to overlap areas of enhanced dissipation rate (Figure 5.21). We suggest that low ϕ_{CCW}/ϕ_{CW} values as a diagnostic of upward propagating energy is not adequate for this upper-ocean (200-1400 m) data.

5.3.3 Shear-to-strain variance ratio

The value of the shear-to-strain variance ratio (R_ω) is of particular relevance when estimating turbulent mixing rates globally. Temperature and salinity measurements providing strain estimates are more readily available with the advent of the Argo program than velocity data which provide shear estimates. As a result, many studies use strain-only finescale parameterizations rather than shear-strain parameterizations to estimate mixing (Sloyan, 2005; Thompson et al., 2007; Wu et al., 2011; Whalen et al., 2012). These strain-only parameterizations are based on assumptions about the local shear-to-strain variance ratio, where the choice of R_ω is based on observed R_ω from previous studies (Table 5.2).

In this study, R_ω ranges from 1 to 19 with a mean value of 5.6. R_ω is similar in the Front and in the Polar Front Zone ($R_\omega \simeq 5$) but is overall higher in the Subantarctic Zone ($R_\omega \simeq 6$)(Figure 5.22). We estimate the sensitivity of the strain-only parameterization to the choice of R_ω by applying a strain-only finescale parameterization to the EM-APEX data and comparing the resulting mean mixing profiles (Figure 5.23). We apply three constant R_ω values: GM $R_\omega = 3$, Kunze et al. (2006) mean $R_\omega = 7$ and our survey mean $R_\omega = 5$. Below 600 m, the resulting mean dissipation rate differs by a factor of three depending on the choice of R_ω. This is moderate since the finescale parameterization is only expected to reproduce microstructure

Whalen et al. (2012)	Global	-	3

Reference	**Location**	**Measured R_ω**	**Assumed R_ω**
Garrett and Munk (1975)	North Atlantic Ocean	3 (mean)	-
Polzin et al. (2003)	Mid-latitude	5-11 (range)	-
Naveira Garabato et al. (2004)	Nordic Seas	8-14 (range)	-
Sloyan (2005)	Southern Ocean	-	3
Kunze et al. (2006)	Global abyssal mean	7	-
Thompson et al. (2007)	Drake Passage	-	10
Fer et al. (2010)	Arctic	11 (mean)	-
Wu et al. (2011)	Southern Ocean	-	7
EM-APEX floats	Plateau	5.6 (mean)	

Table 5.2: Measured and assumed range and mean value for the shear-to-strain variance ratio (R_ω) used in previous studies.

measurements within a factor of two (Polzin et al., 1995). The difference between applying the shear-strain parameterization and the strain-only parameterization on the EM-APEX data assuming $R_\omega = 3$ is substantial: over an order of magnitude (factor of 11) for the mean dissipation rate. Overall, the mixing estimated with the shear-strain parameterization larger than the mixing estimated with the strain-only parameterization, even when using the mean R_ω value from the data set as the constant R_ω. This is likely a product of the variations in R_ω from point to point and profile to profile. Using the overall mean R_ω as a constant in the strain-only parameterization averages both the horizontal and vertical variability of R_ω, and impacts the resulting mixing estimates.

These results suggests that improved knowledge of the spatial distribution of the shear-to-strain variance ratio would considerably improve strain-based parameterizations of the dissipation rate. Also, the uncertainties associated with the strain-based parameterization with no R_ω observations might be higher than previously estimated (Wu et al., 2011).

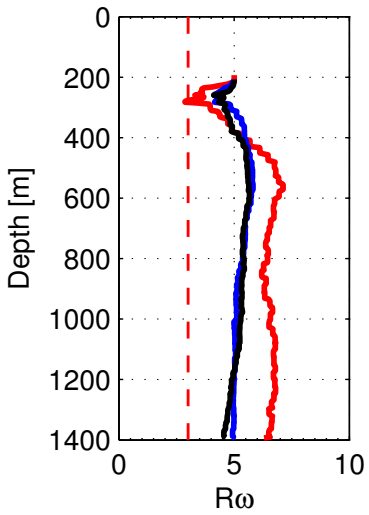

Figure 5.22: Mean vertical profiles as a function of depth of the shear-to-strain ratio (R_w) in the Front (black), the Polar Front Zone (blue) and the Subantarctic Zone (red). The vertical red dotted line indicate the GM value.

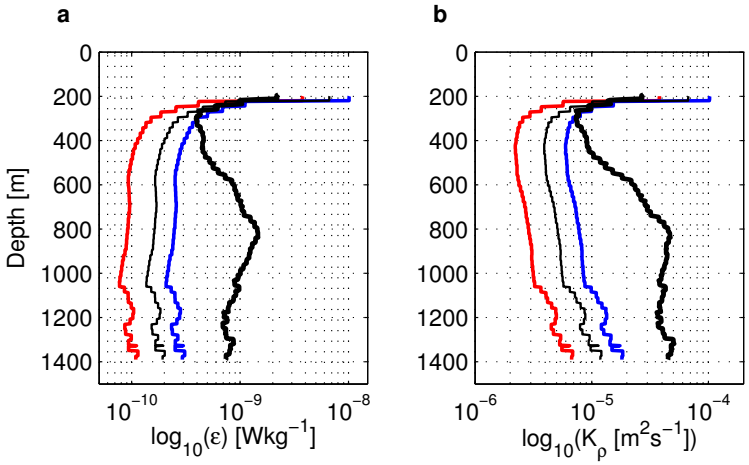

Figure 5.23: Mean vertical profiles as a function of depth of the (a) dissipation rate (ϵ) and (b) diapycnal diffusivity (K_ρ) for $R_\omega = 5$ (black), $R_\omega = 3$ (red), $R_\omega = 7$ (blue) from strain-only parameterization, and from shear-strain parameterization (thick black line).

5.3.4 Water masses and mixing

There is growing evidence that enhancement of turbulent mixing over regions of rough topography is affecting the abyssal stratification and circulation in the Southern Ocean. Transformation of deep water in the Southern Ocean closes the global overturning circulation (Sloyan and Rintoul, 2001). Quantifying the impact of internal wave breaking, and therefore turbulent mixing, on water mass transformation is key to understanding the global overturning (Nikurashin and Ferrari, 2013). In the EM-APEX depth-range (upper 1600 m), dissipation is largest at depths corresponding to AAIW. Nearly 50% of the total dissipation rate estimated in the EM-APEX data occurs in AAIW, while 20% is in SAMW and 31% in UCDW.

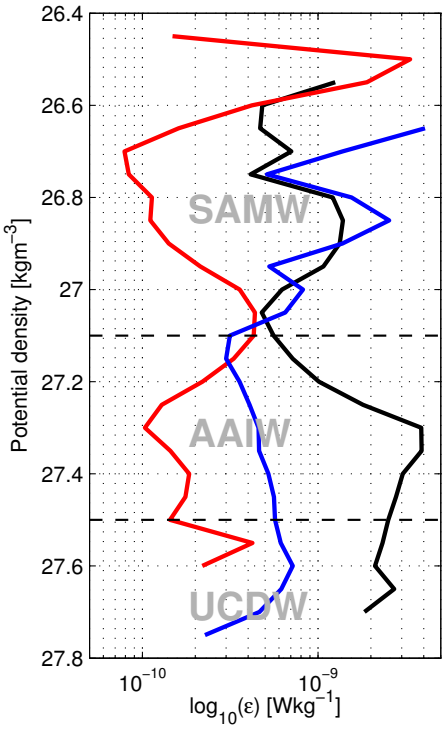

Figure 5.24: Mean vertical profiles as a function of depth of the dissipation rate (ϵ) in the Front (black), the Polar Front Zone (blue) and the Subantarctic Zone (red) in function of potential density (ρ_θ). The horizontal dotted lines indicate ranges of water mass labelled in grey as defined in Section 3.1.

We investigate the impact of the dissipation rate on local water masses by

estimating the dissipation rate distribution in terms of potential density for each dynamical region (Figure 5.24). Overall, the Front is the region where most of the mixing of the water mass takes place: 70% of dissipation rate associated with AAIW is found in the Front. The Polar Front Zone also plays an important role for all water masses: 25% of dissipation rate associated with AAIW, 22% for SAMW and 45% for UCDW is found in the Polar Front Zone. The Subantarctic Zone plays a small role for AAIW and has no associated dissipation with UCDW, due to the depth range of instrument (200-1400 m). The Front and Polar Frontal zone are clearly dominating in terms of water mass mixing, in particular for AAIW and UCDW.

5.3.5 Summary

Robust mixing patterns associated with varied dynamical processes are identified. Overall, the mean diapycnal diffusivity in the Kerguelen Plateau area is moderate, but local mixing intensities reach considerably high values (10^{-3} $m^2\,s^{-1}$) and show strong spatial and temporal variability. Rough topography is associated with mixing values typically three times higher than with smooth topography. The most intense mixing is observed in the frontal jets. We suggest that this enhanced mixing is the result of breaking internal waves generated at the seafloor by the interaction of the Front with the topography on the northern edge of the Kerguelen Plateau. Most of the mixing of water masses takes place in the frontal jets and Polar Front Zone regions. The observation of intense bursts of mixing in an eddy highlights the role of relative vorticity on the dynamics of internal waves. In the Subantarctic Zone, large atmospheric frontal zones seem to generate substantial amounts of wind driven mixing in the upper 600 m of the ocean.

Chapter 6

CHARACTERIZING THE INTERNAL WAVE FIELD

6.1 Introduction

Oceanic internal waves are ubiquitous, with typical scales of kilometres and hours. They are the result of the restoring action of buoyancy forces on water parcels displaced from their equilibrium position (Kantha and Clayson, 2000, Chapter 6). Internal waves propagate both horizontally and vertically through the ocean interior. The source of the disturbance to the density field is typically at the surface of the ocean (wind forcing) or at the bottom of the ocean (flow and topography interaction). Along their pathway, wave-wave interactions and other processes cascade the internal wave's energy to smaller scales, until they break and dissipate (see Section 4.2.1).

Importantly, internal waves provide a link between large scale forcing and small scale dissipation. The transport of momentum and energy within the ocean by internal waves is likely a key in the meridional overturning circulation (Osborn and Burch, 1980). Garrett and Munk (1979) once said that "A full understanding of internal wave dynamics may be essential for a comprehensive understanding of the mean ocean circulation", and it is with this statement in mind that we analyse horizontal velocity observations from the Kerguelen Plateau region and describe the local internal wave field.

Coherent features are identified in the EM-APEX velocity profiles and interpreted in terms of internal wave kinematics. Doing so, we make the assumption that observed coherent features are internal waves as previously done by Polzin (2008); Müller et al. (1978).

6.2 Internal wave theory

6.2.1 Governing equations

Momentum equations

The momentum equations in Cartesian coordinates on the f plane (Vallis, 2006, Chapter 2, Section 3) are

$$\frac{\partial u}{\partial t} + \left[u\frac{\partial u}{\partial x} + v\frac{\partial u}{\partial y} + w\frac{\partial u}{\partial z} \right] = -\frac{1}{\rho}\frac{dp}{dx} + 2\Omega v sin(\phi) + F_x, \qquad (6.1)$$

$$\frac{\partial v}{\partial t} + \left[u\frac{\partial v}{\partial x} + v\frac{\partial v}{\partial y} + w\frac{\partial v}{\partial z}\right] = -\frac{1}{\rho}\frac{dp}{dy} - 2\Omega u sin(\phi) + F_y, \tag{6.2}$$

$$\frac{\partial w}{\partial t} + \left[u\frac{\partial w}{\partial x} + v\frac{\partial w}{\partial y} + w\frac{\partial w}{\partial z}\right] = -\frac{1}{\rho}\frac{dp}{dz} + [2\Omega u cos(\phi)] - g + F_z, \tag{6.3}$$

where $\mathbf{u} = (u, v, w)$ are respectively the position vector $\mathbf{r} = (x, y, z)$ components of the velocity in Cartesian directions, z is measured vertically upward, p and ρ are the pressure and the density of the fluid respectively, Ω is the rate of rotation of the Earth about its axis and g is the gravity. Assuming that the Rossby number is small and since $2\Omega u cos(\phi)$ is much smaller than g, the terms in square brackets [ ] can be ignored.

When defining the Coriolis frequency as $f = 2\Omega sin(\phi)$ and removing the friction terms (F_x, F_y, F_z), (6.1), (6.2) and (6.3) become

$$\frac{\partial u}{\partial t} - fv = -\frac{1}{\rho}\frac{dp}{dx}, \tag{6.4}$$

$$\frac{\partial v}{\partial t} + fu = -\frac{1}{\rho}\frac{dp}{dy}, \tag{6.5}$$

$$\frac{\partial w}{\partial t} = -\frac{1}{\rho}\frac{dp}{dz} - g. \tag{6.6}$$

From the conservation of mass, a compressible fluid must satisfy the continuity equation

$$\frac{\partial \rho}{\partial t} + \frac{\partial(\rho u)}{\partial x} + \frac{\partial(\rho v)}{\partial y} + \frac{\partial(\rho w)}{\partial z} = 0, \tag{6.7}$$

which is equivalent to

$$\frac{1}{\rho}\frac{D\rho}{Dt} + \frac{\partial u}{\partial x} + \frac{\partial v}{\partial y} + \frac{\partial w}{\partial z} = 0. \tag{6.8}$$

In the context of an incompressible fluid where the density equation is

$$\frac{1}{\rho}\frac{D\rho}{Dt} = 0, \tag{6.9}$$

we rewrite (6.8) as

$$\frac{\partial u}{\partial x} + \frac{\partial v}{\partial y} + \frac{\partial w}{\partial z} = 0. \tag{6.10}$$

Next, we consider a pressure and density perturbation from the state of rest. The equation for fluctuating components of the density equation is

$$\frac{\partial \rho}{\partial t} + u\frac{\partial \rho}{\partial x} + v\frac{\partial \rho}{\partial y} + w\frac{\partial \bar{\rho}}{\partial z} + w\frac{\partial \rho}{\partial z} = 0, \tag{6.11}$$

where the overbar indicates the mean state. The nonlinear terms $u(\partial\rho/\partial x)$, $v(\partial\rho/\partial y)$ and $w(\partial\rho/\partial z)$ can be ignored for small amplitude motions and (6.18) then becomes

$$\frac{\partial \rho}{\partial t} + w\frac{\partial \overline{\rho}}{\partial z} = 0. \tag{6.12}$$

To summarise, the momentum equations of a continuously stratified, incompressible, homogeneous fluid on the f plane with density ρ and subject to small perturbations about the background state of rest are

$$\frac{\partial u}{\partial t} - fv = -\frac{1}{\rho_0}\frac{\partial p}{\partial x}, \tag{6.13}$$

$$\frac{\partial v}{\partial t} + fu = -\frac{1}{\rho_0}\frac{\partial p}{\partial y}, \tag{6.14}$$

$$\frac{\partial w}{\partial t} + g\frac{\rho}{\rho_0} = -\frac{1}{\rho_0}\frac{\partial p}{\partial z}, \tag{6.15}$$

$$\frac{\partial u}{\partial x} + \frac{\partial v}{\partial y} + \frac{\partial w}{\partial z} = 0, \tag{6.16}$$

$$\frac{\partial \rho}{\partial t} + w\frac{\partial \overline{\rho}}{\partial z} = 0, \tag{6.17}$$

where (u, v, w) are the (x, y, z) components of the velocity, p is the pressure, $f = 2\omega \sin\phi$ is the Coriolis frequency, where ϕ is latitude and ω is the rotation rate of the earth, and ρ is the density defined as

$$\rho = \rho_0 + \overline{\rho}(z) + \rho'(x, y, z, t) \tag{6.18}$$

where ρ_0 is the reference density and the overbar indicates the mean state. Defining the buoyancy as $b = -g\rho/\rho_0$, equation (6.15) can be re-written as

$$\frac{\partial w}{\partial t} = -\frac{1}{\rho_0}\frac{\partial p}{\partial z} + b. \tag{6.19}$$

Using the Boussinesq approximation (Cushman-Roisin and Beckers, 2006, Section 3.7), we approximate ρ by a constant reference density ρ_0 unless it is coupled with gravity. A more detailed discussion on the derivation of the momentum equations can be found in Vallis (2006).

Buoyancy oscillations

In the case of $u = v = p = \partial w/\partial z = 0$, we can combine (6.17) and (6.15) to give

$$\frac{\partial^2 w}{\partial t^2} + N^2 w = 0, \tag{6.20}$$

where we have defined the buoyancy frequency as the frequency at which vertical motions oscillate in the fluid

$$N = \sqrt{\frac{\partial \bar{b}}{\partial z}} = \sqrt{-\frac{g}{\rho_0}\frac{\partial \bar{\rho}}{\partial z}}. \tag{6.21}$$

Dispersion relation

The direction of a plane wave's phase propagation is the three-dimensional wave vector $\mathbf{p} = (k, l, m)$, where m is the vertical plane component, also called the vertical wavenumber and where k and l combine as the horizontal wave vector $\mathbf{k} = (k, l)$. The azimuth (φ) of the horizontal wave vector is $\varphi = tan^{-1}(\frac{l}{k})$, while its magnitude, the horizontal wavenumber $k_h = |\mathbf{k}| = (k^2 + l^2)^{1/2}$ (Figure 6.1).

To obtain the dispersion relation Phillips (1977), assumed that the background stratification was constant. The internal wave variables can then be written in the form of plane wave solutions

$$w = w_0 e^{ikx+ily+imz-i\omega t} = w_0 e^{i[\mathbf{r}.\mathbf{p}-\omega t]}, \tag{6.22}$$

where ω is the observed frequency. The observed frequency ω, often referred to as the "Eulerian" frequency, is the Doppler shifted frequency measured by a stationary observer as opposed to the intrinsic frequency (ω_0) measured while moving with the mean flow ($\bar{U}$)

$$\omega_0 = \omega - \mathbf{k} \cdot \bar{\mathbf{U}}. \tag{6.23}$$

Note that in the absence of a mean flow, both frequencies are equal.

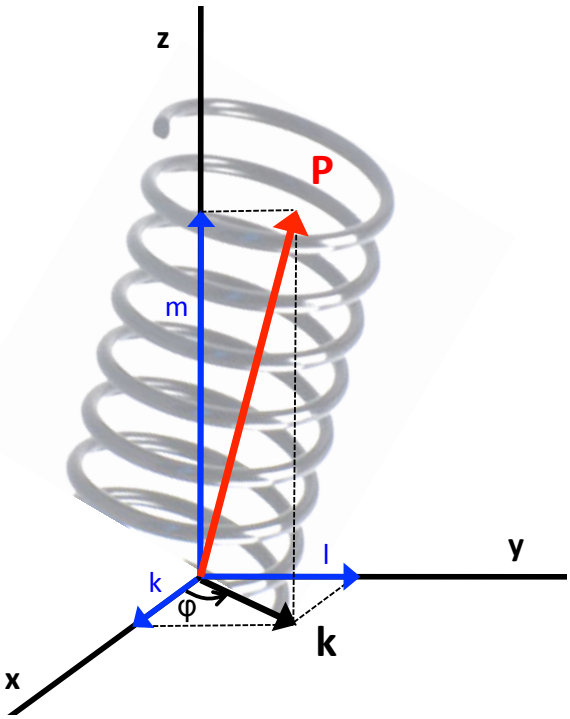

Figure 6.1: Coordinate system used to describe internal waves. The wave vector $\mathbf{p}$ is given by $\mathbf{p} = (k, l, m)$ while the horizontal wave vector ($\mathbf{k}$) is $\mathbf{k} = (k, l)$ in the direction of increasing (x,y,z). The horizontal azimuth (φ) of the horizontal wave vector determines the orientation of the wave vector in the horizontal plane.

In the linearised momentum equations (6.13), (6.14), (6.15), (6.16), and (6.17), the independent variables, which are the vorticity and pressure terms, can

be eliminated to obtain the internal wave equation in vertical velocity (see Appendix C for details)

$$\left(\frac{\partial^2}{\partial t^2} + f^2\right)\frac{\partial^2 w}{\partial z^2} + \nabla^2{}_h w\left(N^2 + \frac{\partial^2}{\partial t^2}\right) = 0, \tag{6.24}$$

where $\nabla^2{}_h = \partial/\partial x^2 + \partial/\partial y^2$ is the horizontal Laplacian operator.

Substituting the plane wave solution (6.22) into the internal wave equation (6.24) yields the dispersion relation

$$\omega_0^2 = \frac{f^2 m^2 + N^2 k_h^2}{m^2 + k_h^2}, \tag{6.25}$$

which can be rewritten as

$$\frac{k_h^2}{m^2} = \frac{f^2 - \omega_0^2}{\omega_0^2 - N^2}. \tag{6.26}$$

Polarisation relations

Assuming a constant stratification and plane wave solutions where the variables are proportional to $e^{i(\mathbf{p}.\mathbf{r}-\omega t)}$, the dependent variables can be expressed in terms of wave amplitude (a) (see Polzin and Lvov (2011) for equations). These polarisation relations lead to three diagnostics that we will be using in Section 6.2.2.

The first diagnostic provides an estimate of the ratio of horizontal kinetic energy (E_k) to potential energy (E_p) for a single internal wave

$$\frac{E_k}{E_p} = \frac{\omega_0^2 + f^2}{\omega_0^2 - f^2}. \tag{6.27}$$

The second diagnostic allows us to estimate the ratio of velocity variance in the clockwise (E_{cw}) and counterclockwise (E_{ccw}) rotating components (rotary ratio) using the near inertial rotation of the velocity vector ($\mathbf{u}$) due to the rotation of the Earth. The velocity vector draws an elliptical helix with depth, in which the ratio of velocity variance in the E_{cw} and in the E_{ccw} rotating component is

$$\frac{E_{cw}}{E_{ccw}} = \frac{(\omega_0 + f)^2}{(\omega_0 - f)^2}, \tag{6.28}$$

where the convention is that a positive intrinsic frequency implies downward phase (and therefore upward energy) propagation of the internal wave, which corresponds to CW dominance in the Southern Hemisphere (Polzin and Lvov, 2011).

The third diagnostic provides an estimate of the horizontal azimuth (φ) of the wave vector ($\mathbf{k}$). This diagnostic estimates the phase between the rotary velocity components ($CW = u - iv$ and $CCW = u + iv$) and the buoyancy perturbation b. Note that u, v, b, CWW and CW are Fourier coefficients and therefore are complex. In the Southern Hemisphere, the observed phase (φ_0) depending on which rotary velocity component (CCW or CW) dominates is

$$\varphi_0 = CWb^* = \tan^{-1}(\frac{-k}{-l}) and \tag{6.29}$$

$$\varphi_0 = CCWb^* = \tan^{-1}(\frac{k}{-l}), \tag{6.30}$$

where ($*$) represents the complex conjugate of b. Both (6.29) and (6.30) are coherence estimates in the spectral domain. The observed phase (φ_0) of the rotary velocity component can be interpreted as the horizontal azimuth (φ) of the horizontal wave vector in polar coordinates as

$$\varphi = \tan^{-1} \frac{-\cos(\varphi_0)}{\sin(\varphi_0)} \tag{6.31}$$

for waves with a velocity vector rotating CCW and

$$\varphi = \tan^{-1} \frac{-\cos(\varphi_0)}{-\sin(\varphi_0)} \tag{6.32}$$

for waves with a velocity vector rotating CW. See Appendix C.1 for derivations.

6.2.2 Properties of internal waves

Vertical wavenumber

By re-arranging the dispersion relation equation (6.26), we obtain an equation for the vertical wavenumber (m)

$$m = \pm k_h \left[\frac{N^2 - \omega_0^2}{\omega_0^2 - f^2} \right]^{1/2}. \tag{6.33}$$

Equation (6.33) implies that for $\omega_0 > f$, we have $m > 0$. Consequently, in the Southern Hemisphere, if the intrinsic frequency of the internal wave (ω_0) is larger than the inertial frequency (f), the horizontal velocity vector is rotating in a counterclockwise manner.

Group velocity

The group velocity (C_g) is the gradient of the intrinsic frequency in the vertical wavenumber space:

$$\mathbf{C}_g = \left[\frac{\partial \omega_0}{\partial k}, \frac{\partial \omega_0}{\partial l}, \frac{\partial \omega_0}{\partial m} \right], \tag{6.34}$$

$$\mathbf{C}_g = \left[\frac{k(N^2 - \omega_0^2)^2}{\omega_0 m^2 (N^2 - f^2)}, \frac{l(N^2 - \omega_0^2)^2}{\omega_0 m^2 (N^2 - f^2)}, -\frac{(\omega_0^2 - f^2)(N^2 - \omega_0^2)}{\omega_0 m (N^2 - f^2)} \right], \tag{6.35}$$

which we can reformulate (see Appendix C.2 for details) under the hydrostatic approximation ($\omega_0 \simeq f$ and $\omega_0 \leqslant N$) as

$$\mathbf{C}_g \simeq \left[\frac{kN^2}{\omega_0 m^2}, \frac{lN^2}{\omega_0 m^2} \right], \tag{6.36}$$

and therefore the magnitude C_g of the vector $\mathbf{C}_g$ is

$$C_g = \sqrt{\left(\frac{kN^2}{\omega_0 m^2} \right)^2 + \left(\frac{lN^2}{\omega_0 m^2} \right)^2}. \tag{6.37}$$

The parameters and diagnostics described in this section are summarized in Table 6.1.

6.3 Internal wave analysis method

Identifying internal waves and extracting their properties from observations is challenging. In this section, we explain how we obtained the properties of

Local Coriolis frequency	$f_0 = 1 \times 10^{-4}$	$[s^{-1}]$
Intrinsic frequency	$\omega_0 = \omega - \mathbf{k} \cdot \mathbf{u}$	$[s^{-1}]$
Wave vector	$\mathbf{p} = (k, l, m)$	
Horizontal wavenumber	$k_h = (k^2 + l^2)^{1/2}$	[cpm]
Dispersion relation	$\frac{k_h^2}{m^2} = \frac{f^2 - \omega_0^2}{\omega_0^2 - N^2}$	
Energy ratio	$\frac{E_k}{E_p} = \frac{\omega_0^2 + f^2}{\omega_0^2 - f^2}$	
Rotary ratio	$\frac{E_{cw}}{E_{ccw}} = \frac{(\omega_0 + f)^2}{(\omega_0 - f)^2}$	
Vertical wavenumber	$m = \pm k_h \left[\frac{N^2 - \omega_0^2}{\omega_0^2 - f^2} \right]^{1/2}$	[cpm]
Group velocity	$C_g = \left[\left(\frac{kN^2}{\omega_0 m^2} \right)^2 + \left(\frac{lN^2}{\omega_0 m^2} \right)^2 \right]^{1/2}$	$[ms^{-1}]$

Table 6.1: Parameters and relations based on single plane wave solutions of the form $e^{ikx+ily+imz-i\omega t}$ to the linearized equations of motion (Section 6.2.1).

46 internal waves in the region of the Kerguelen Plateau applying linear wave theory to coherent features in vertical profiles of horizontal velocity. The velocity profiles were collected over two and a half months by eight EM-APEX profiling floats. This analysis is restricted to depths at which the theory can be applied and where velocity observations are available (200 to 1600 m). Diagnostics for this analysis are based on linear internal wave kinematics summarised in Table 6.1. In this Section we demonstrate the method by presenting the analysis of one of the 46 coherent feature identified as "coherent feature number 5". The same method was applied to all identified coherent features.

6.3.1 Identifying coherent features

The time-depth series of the velocity profiles shows the presence of many coherent features. We define 'feature number 5' as the coherent feature that ranges from approximately profile 64 to profile 76 between 600 and 1000 m in float 3761 velocity data (Figure 6.2). Altogether, coherent features are found in 400 profiles out of 914 velocity profiles available.

The horizontal velocity anomaly profiles help identify the coherent feature

location and carry information about the phase propagation of the associated internal wave. By tracking the peaks in velocity anomalies, we can determine the direction of rotation of the velocity vector and deduce the phase propagation (Figure 6.3). Connecting each point on the horizontal plane either gives a CW or CCW rotation. Here, the CCW motion indicates downward energy propagation that corresponds to upward phase propagation of the observed coherent feature (Figure 6.3b).

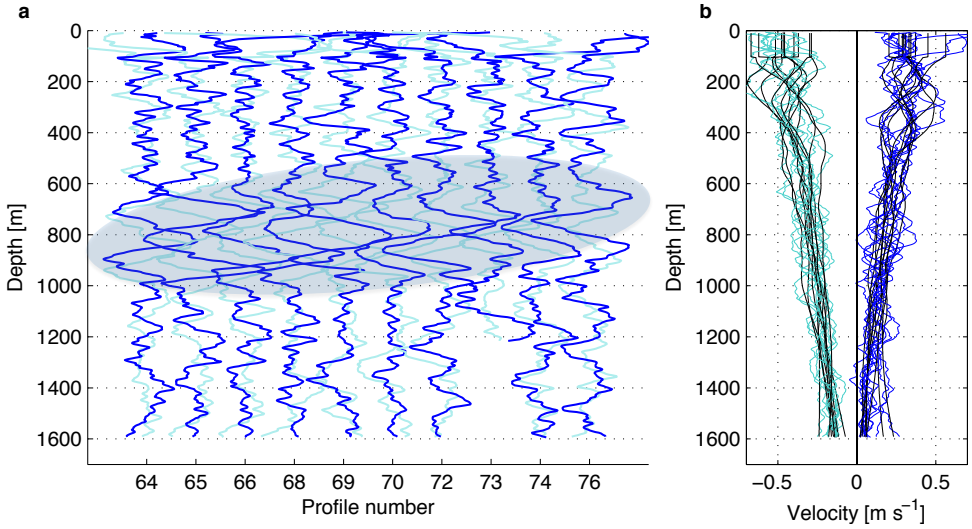

Figure 6.2: **a)** Time series of profiles of horizontal velocity anomaly (float 3761): eastward horizontal velocity u' (dark blue) and northward horizontal velocity v' (cyan). Feature 5 is identified by the coherence in velocity anomaly (blue shading). Missing profile numbers are the results of the float's sampling strategy (Figure 2.4). **b)** East horizontal velocity profiles u (dark blue), north horizontal velocity v (cyan) and corresponding smoothed profiles (black).

6.3.2 Wavelength, frequency and period

Next we consider the vertical wavenumber and energy spectra for the profiles in which coherent feature number 5 is identified. Kinetic energy, matched by downward (CCW) motions exceeds potential and upward (CW) energy at the internal wave frequencies (Figure 6.4). A major downward energy peak matched by a kinetic energy peak with a vertical wavenumber $m = 0.01$ cpm is identified as the spectral signature of coherent feature number 5. The

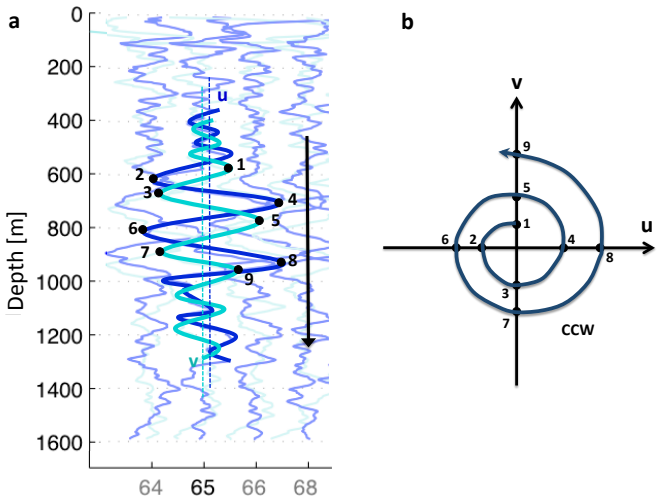

Figure 6.3: (a) As Figure 6.2a, but the vertical dotted lines indicate the mean horizontal velocity value of u (dark blue) and v (cyan) for profile 65, while the arrow indicates the sampling direction. (b) The equivalent location in polar coordinates of each velocity peak are plotted and linked indicating a CCW propagation of the horizontal wave vector.

downward energy peak on the spectra confirms the earlier finding of upward phase propagation (Figure 6.3b).

From the vertical wavenumber (m) of the feature, we estimate the coherent feature vertical wavelength $\lambda = 1/m = 206$ m. We also estimate the feature intrinsic frequency (ω_0) by re-arranging the energy ratio equation $\omega_0 = f_0[(E_p + E_k)/(E_k - E_p)]^{1/2} = 1.09 \times 10^{-4}\,\mathrm{rad\,s^{-1}}$ (Table 6.1, see Appendix C for details) where we use the observed energy ratio estimates from the spectra. Subsequently, we estimate the coherent feature's period (T) $T = 1/\omega_0 = 5.7 \times 10^4$ s=15.9 hours.

We apply a"WKB scaling" of the vertical coordinates (e.g. Müller et al., 1986; Henyey et al., 1986; Alford, 2001; Polzin, 2008; Sun and Pinkel, 2012; Klymak et al., 2013), where a mean profile of the buoyancy frequency (N) defines the scaled coordinates

$$z_{WKB} = \frac{1}{N_0}\int_0^z N(z')dz', d, \tag{6.38}$$

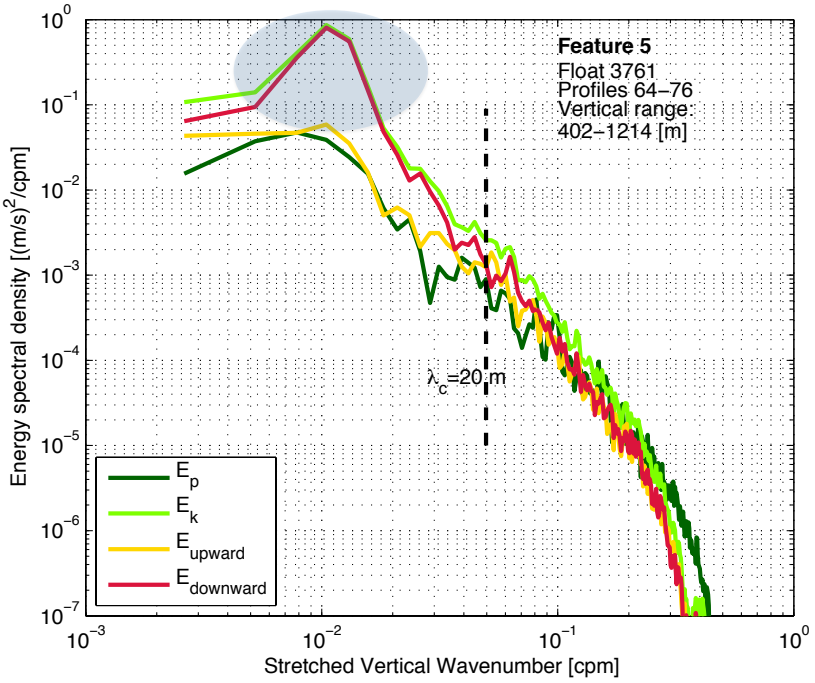

Figure 6.4: Potential (E_p) and kinetic (E_k) energy as well as CW (E_{upward}) and CCW ($E_{downward}$) rotary spectra in terms of stretched vertical wavenumber of horizontal velocity profiles 64 to 76 (float 3761) computed using data between 402 to 1126 m. The vertical black dashed line indicates the cut-off wavenumber position and its corresponding cut-off wavelength (λ_c) is given. Feature number 5 is identified by the peak in both kinetic and downward (CCW) energy at vertical wavenumber $\sim 1 \times 10^{-2}$ cpm (blue shading).

where $N_0 = 3$cph is the reference N (Garrett and Munk, 1972). The scaling of N results in 'stretched' variables such as depth, wavenumber, wavelength in WKB coordinates (Figure 6.4).

The Wentzel-Kramers-Brillouin (WKB) approximation is a semi-classical calculation in quantum mechanics. It is used to obtain an approximate solution to a time-independent one-dimensional differential equation (here a linear wave equation). It involves recasting the wave function as an exponential power series to recover approximate solutions for the wave phase and slowly varying amplitude. Slowly varying refers to the fact that within a small area, the wave function is well approximated by a plane wave and that the wavelength only varies over distances much larger than the wavelength. The problem was first solved by Lord Rayleigh (1912) who solved the connection of solutions on opposite sides of a turning point. Subsequently, the solution was re-discovered almost simultaneously by Wentzel (1926), Kramers (1926) and Brillouin (1926), who published applications of this theory to the Schrödinger equation.

6.3.3 Horizontal wavenumber

The horizontal wavenumber (k_h) of the coherent feature can be estimated using the dispersion relation (see Table 6.1) where the hydrostatic approximation ($\omega_0^2 \ll N^2$) has been applied such that $k_h = \pm m/N(\omega_0^2 - f^2)^{1/2} = 5.7 \times 10^{-4}\,\mathrm{rad\,m^{-1}}$. Here we use $N = N_0 = 0.00524\ \mathrm{s}^{-1} = 3$ cph to match the stretched coordinates (Equation 6.38). We then estimate the horizontal wavelength of feature number 5 $\lambda_h = 2\pi/k_h = 1.5 \times 10^4\,\mathrm{m}$=15 km.

6.3.4 Horizontal wave vector azimuth and group velocity

From the spectral coherence we can examine the relation between the rotary (either CCW or CW) and buoyancy perturbations. The analysis of the coherence between the rotary (CCW in this case) and the buoyancy perturbations shows a peak in the rotary coherence that matches the peak in

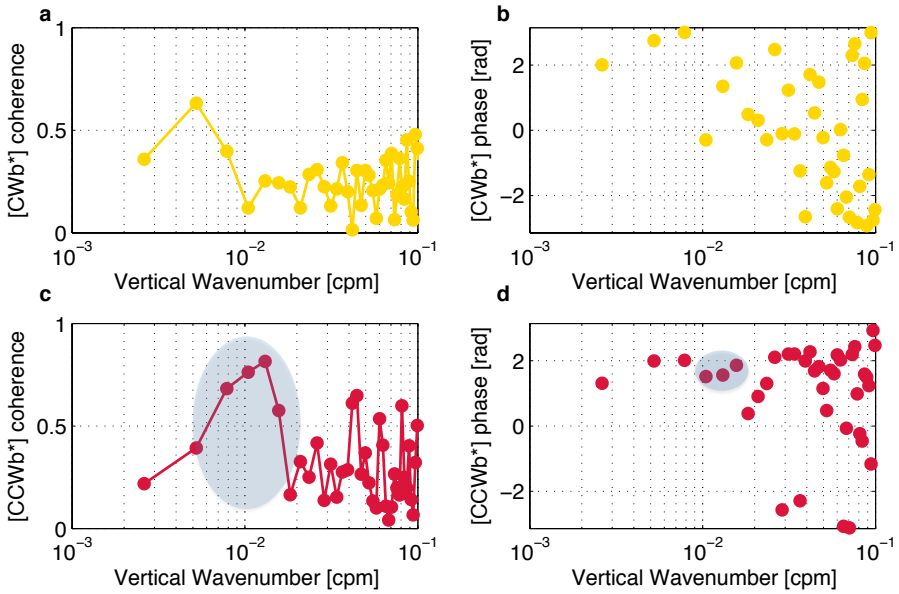

Figure 6.5: Rotary-buoyancy coherence (a) $[CWb^*]$, (c) $[CCWb^*]$ and phase (b) $[CWb^*]$, (d) $[CCWb^*]$ estimates for feature number 5 (profiles 64 to 76, float 3761). Feature number 5 peak in coherence and corresponding phase points are shaded in blue.

the energy spectrum at approximately 0.01 cpm (Figure 6.5c). The peak in the rotary coherence corresponds to a mean phase $\varphi_0 = 1.7$ rad (Figure 6.5d). From the peak in the phase coherence, we estimate the horizontal wave vector ($\mathbf{k}$) components (k, l) where $k = -K_h cos(\varphi_0) = 4 \times 10^{-4}$ and $l = -K_h sin(\varphi_0) = -5 \times 10^{-5}$ (when CCW rotation). For a feature with a peak in the CW, $k = K_h cos(\varphi_0)$ and $l = -K_h sin(\varphi_0)$.

The horizontal azimuth ($\varphi = 173°$) of the horizontal wave vector of the coherent feature can be estimated as the angle between the vectors k and l. A horizontal azimuth $\varphi = 173°$ indicates that feature number 5 is propagating westward.

The intrinsic group velocity of feature number 5 ($C_g = 0.023\,\mathrm{m\,s^{-1}}$) is estimated using equation 6.37, using the k and l vectors derived above. We set $N = N_0 = 0.00524$ s^{-1} to account for stretched coordinates.

6.3.5 Wave-mean interactions

Some properties of the coherent features with regards to the flow field can also be estimated: the Doppler shift associated with advection by the mean flow as well as wave-mean interaction timescales.

Doppler shift

The Doppler shift is defined as $\mathbf{k} \cdot \mathbf{u} = k\bar{u} + l\bar{v}$ where $\bar{u}$ and $\bar{v}$ are the mean absolute velocity estimates for the selected profiles at the depth of the coherent feature ($(\bar{u}, \bar{v}) = (0.2, -0.3)\mathrm{m\,s^{-1}}$ see Figure 6.2b). A positive Doppler shift works against the flow and vice-versa, a negative Doppler shift works with the flow field. In the case of feature number 5, the Doppler shift, $\mathbf{k} \cdot \mathbf{u}$ $=9.5 \times 10^{-5}\,\mathrm{rad\,s^{-1}}$, is similar to the local inertial frequency f $=-1.05 \times 10^{-4}\,\mathrm{s^{-1}}$. Note that confidence in Doppler shift estimates depends on the accuracy of the horizontal wave vector azimuth and therefore the rotary phase estimate.

Interaction timescales

We consider a dissipation timescale (τ_ϵ)

$$\tau_\epsilon = \frac{2E}{\epsilon_{GM}} \left(\frac{\lambda_{cGM}}{\lambda_c} \right)^2, \tag{6.39}$$

where $E = \int E_P + E_K = 0.0011\,\mathrm{m^2 s^{-2}}$ is the total energy contained in the peak associated with the coherent feature on the energy spectrum, $\epsilon_{GM} = 8 \times 10^{-10}\ \mathrm{m^2 s^{-1}}$ is the GM76 reference dissipation rate, $\lambda_{cGM} = 10\,\mathrm{m}$ is the GM76 reference critical wavenumber and $\lambda_c = 20\,\mathrm{m}$ is the observed critical wavenumber for internal wave (5). We find $\tau_\epsilon = 7.0 \times 10^5\,\mathrm{s} = 8\,\mathrm{days}$ for internal wave (5).

We also consider a propagation timescale (τ_{prop}) that estimates the time it would take for the internal wave to propagate away from the flow field

$$\tau_{prop} = \frac{L_{Ro}}{C_g}, \tag{6.40}$$

where we approximate the local Rossby radius of deformation to $L_{Ro} = 15000$ m. The propagation timescale for feature number 5 is τ_{prop} =6.4×10^5 s=8 days. A coherent feature with a dissipation timescale shorter than its propagation timescale indicates local dissipation of the feature. If the propagation timescale is shorter, then the coherent feature dissipates elsewhere.

Summary

This method is applied to 46 identified coherent features and the resulting properties are presented in the next section. All the coherent features and their properties are individually listed in Table 6.2 and Table **??**. Note that this analysis only applies to single linear internal waves.

	Float	**Profiles**	**Peak**	**Depth**	λ	$\lambda_{\mathbf{h}}$	**m**	ϕ	**Dshift** $\times 10^{-3}$	$\mathbf{C_g}$	**T**	τ_ϵ	$\tau_{\mathbf{prop}}$
3	3761	38-44	E_k down	800	101	6.3	0.02	-5°	0.31	1.4	15.7	0	12
5	3761	64-76	E_k down	800	205	15.0	0.01	173°	0.09	2.3	15.9	8	7
6	3761	80-84	E_k up	350	162	4.4	0.01	42°	-0.40	3.3	13.1	20	5
7	3761	105-114	E_k down	400	321	31.9	0.006	-92°	0.03	3.1	15.9	16	6
8	4051	5-10	E_k	700	188	19.8	0.009	114°	-0.12	2.6	16.6	4	7
9	4051	29-48	E_k down	900	214	14.7	0.009	47°	0.08	3.2	16.2	30	5
10	4051	46-53	E_k up	300	255	32.3	0.007	134°	-0.07	2.6	17.3	9	7
11	4051	54-64	E_k down	500	161	11.2	0.01	70°	0.28	3.1	16.5	5	6
12	4051	73-86	E_k down	600	182	19.2	0.009	14°	0.001	2.6	17.2	10	7
13	4051	64-78	E_k down	600	90.3	13.3	0.02	22°	0.12	0.9	17.7	5	18
15	3951	40-46	E_k down	500	97.1	12.9	0.02	-27°	0.04	1.1	16.9	7	16
16	3951	34-40	E_k down	300	196	30.9	0.008	-43°	0.09	2.0	16.9	68	9
17	3951	4-11	E_k down	400	64.8	5.2	0.025	-54°	0.74	1.3	16.0	9	14
18	3950	4-20	E_k down	800	198	11.9	0.011	-119°	0.05	2.8	16.0	80	6
19	3950	20-24	E_k down	800	258	12.4	0.008	-156°	0.002	4.5	15.3	14	4
20	3950	25-30	E_k up	1000	227	11.3	0.009	-152°	0.031	4.1	15.3	16	4
21	3950	30-37	E_k up	1000	138	7.8	0.017	-102°	-0.02	1.8	15.9	10	10
22	3950	49-54	E_k up	1000	313	21.6	0.007	-38°	-0.03	3.5	16.2	8	5
23	3950	66-77	E_k up	700	218	14.4	0.010	23°	-0.06	2.8	15.8	20	6
24	3764	5-14	E_k down	400	78.3	13.5	0.023	-171°	0.003	0.6	17.2	1	29
25	3764	14-22	E_k Up	800	193	19.2	0.009	10°	-0.07	2.5	17.0	11	7
26	3764	22-33	E_k down	700	192	19.3	0.009	-144°	-0.10	2.9	17.1	10	6
27	3764	52-80	E_k down	600	123	13.1	0.014	128°	-0.06	1.7	17.1	1	10
28	3764	65-70	E_k down	400	163	19.9	0.012	126°	-0.03	1.6	17.2	20	11
29	3764	112-122	E_k down	600	118	9.5	0.015	138°	-0.05	1.9	16.2	1	9
30	3764	148-154	E_k down	700	136	21.3	0.015	141°	0.0002	0.9	16.9	10	19
31	3952	74-81	E_k up	500	338	18.0	0.006	13°	-0.05	6.3	15.1	3	3
32	3952	84-93	E_k up	1000	181	11.6	0.015	-57°	-0.03	1.6	16.0	1	11
33	3952	102-110	E_k up	1000	122	7.4	0.020	40°	-0.17	1.3	15.8	1	13
34	3952	134-138	E_k up	900	180	24.8	0.013	-54°	-0.09	1.0	16.2	13	18
35	3952	146-150	E_k up	600	141	14.0	0.014	153°	0.20	1.4	15.8	18	13
36	3952	160-166	E_k down	600	359	14.7	0.006	-28°	0.18	7.1	14.1	53	2
37	3952	169-174	E_k down	700	200	12.3	0.011	6°	0.22	2.8	15.3	109	6
38	3760	87-94	E_k down	700	255	16.2	0.008	-16°	0.08	3.4	15.8	32	5
39	3760	95-99	E_k down	900	198	20.6	0.013	-77°	0.06	1.2	16.4	118	15
40	3760	116-126	E_k up	800	226	12.2	0.011	-24°	-0.06	2.8	15.5	81	6
41	3760	186-191	E_k up	800	298	15.2	0.008	-15°	-0.03	4.0	15.2	12	4
42	3760	204-210	E_k up	1100	173	8.4	0.017	-44°	-0.03	1.6	15.6	87	11
43	3760	234-239	E_k up	600	135	13.9	0.015	41°	0.04	1.2	16.0	34	14
44	3762	4-21	E_k up	600	165	9.5	0.012	-30°	-0.04	2.6	15.7	21	7
45	3762	85-90	E_k down	900	329	13.4	0.007	38°	0.12	6.0	14.8	24	3
46	3762	176-180	E_k down	900	208	14.6	0.010	-41°	0.18	2.8	16.2	31	6
47	3762	190-194	E_k down	600	171	11.3	0.012	-122°	-0.28	3.0	15.5	80	6
48	3762	208-210	E_k down	600	159	-	0.012	144°	-	-	-	47	-
49	3762	216-220	E_k down	500	216	14.1	0.008	-25°	-0.21	4.3	15.6	25	4
50	3762	240-244	E_k down	300	131	20.2	0.014	58°	0.04	1.0	17.3	212	17

Table 6.2: Properties of internal waves (1 to 50) from the EM-APEX data set: internal wavenumber, float number, profiles in which the coherent feature was identified, spectral peak and energy propagation, depth of feature [m], vertical wavelength (λ) [m], horizontal wavelength (λ_h) [km], vertical wavenumber (m) [cpm], horizontal azimuth (ϕ) [°], Doppler Shift [rad s^{-1}], group velocity (C_g) [cm s^{-1}], period (T) [hour], dissipation time-scale (τ_ϵ) [day] and propagation time-scale (τ_{prop}) [day].

6.4 Internal wave results

6.4.1 General properties of the internal waves

In the EM-APEX float data set we observe 50 coherent internal wave features, 4 of which have ambiguous spectral signals and are discarded. In the remaining 46 coherent features, 20 have energy propagating upwards and 26 energy propagating downwards (Table 6.2 and **??**). On average, 8 vertical profiles of horizontal velocity are considered in the analysis of each coherent feature. The location of the identified coherent features in the water column is relatively evenly distributed between 200 and 1000 m with the maximum number of coherent features observed at 600 m depth. Features are scarce above 200 and below 1000 m (Figure 6.6a).

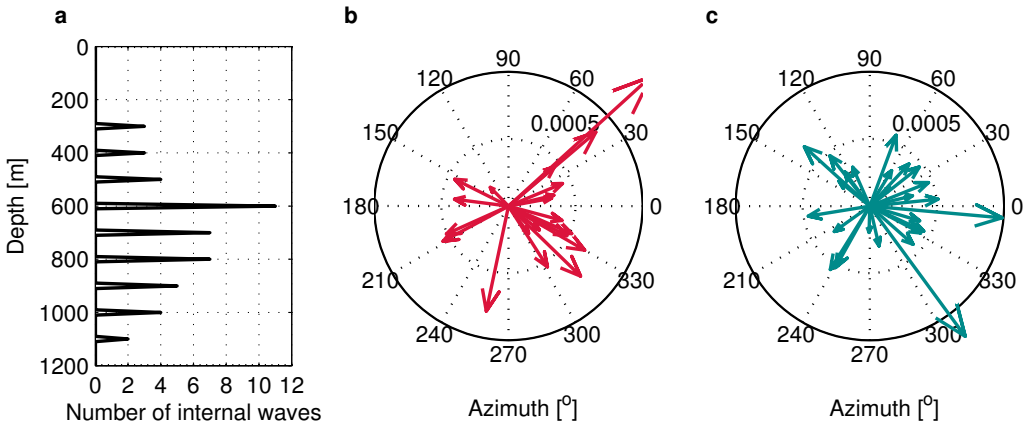

Figure 6.6: (a) Number of coherent features observed as a function of depth. (b) and (c) Azimuth in polar coordinates of observed coherent features on the horizontal plane for upward propagating coherent features (red) and downward propagating features (blue). The length of the vector is proportional to the group velocity of each feature. The azimuth is positive CCW from the x-axis.

The identified coherent internal waves features in the vicinity of the Kerguelen Plateau have approximately a mean vertical wavelength of 200 m and a mean horizontal wavelength of 15 km. The average period (T) is 16 hours, which is close to the local inertial period (17 hours at 45°S) and the mean horizontal group velocity (C_g) is 3 cm s^{-1}. Coherent features with smaller

period (higher frequency) typically have higher group velocity (Figure 6.7a). The aspect ratio of ocean surface waves is usually one. Here, we find that the average aspect ratio (λ_h/λ) of the coherent features is 0.015 (Figure 6.7b).

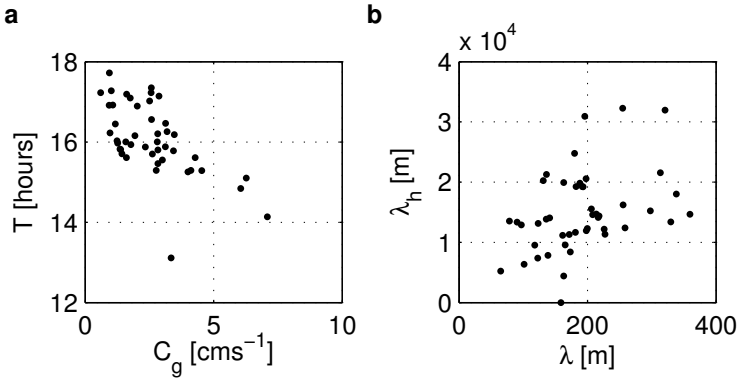

Figure 6.7: (a) Relation between the horizontal group velocity (C_g) and the period (T) of each coherent feature and (b) relation between the vertical wavelength (λ) and the horizontal wavelength (λ_h).

The mean dissipation timescale ($\tau_\epsilon = 30$ days) for the coherent features is larger than the mean propagation timescale ($\tau_{prop} = 9$ days) by a factor of three. Deeper features (where deep is defined as between 750 and 1200 m) propagate 25% faster than shallow features (above 550 m). Overall, downward propagating coherent features travel in all directions but upward propagating features have a tendency to propagate southeast on the horizontal plane (Figure 6.6 b and c). Upward propagating and downward propagating coherent features have similar horizontal and vertical wavelengths, periods and propagation timescales (Table 6.3).

6.4.2 Distribution of the internal waves with regard to the flow field

The coherent features are scattered along the trajectories of the floats, with most features located near the northern edge of the Kerguelen Plateau, in the Front and in the eddy (Figure 6.8).

Coherent features with upward energy propagation are on average 100 m

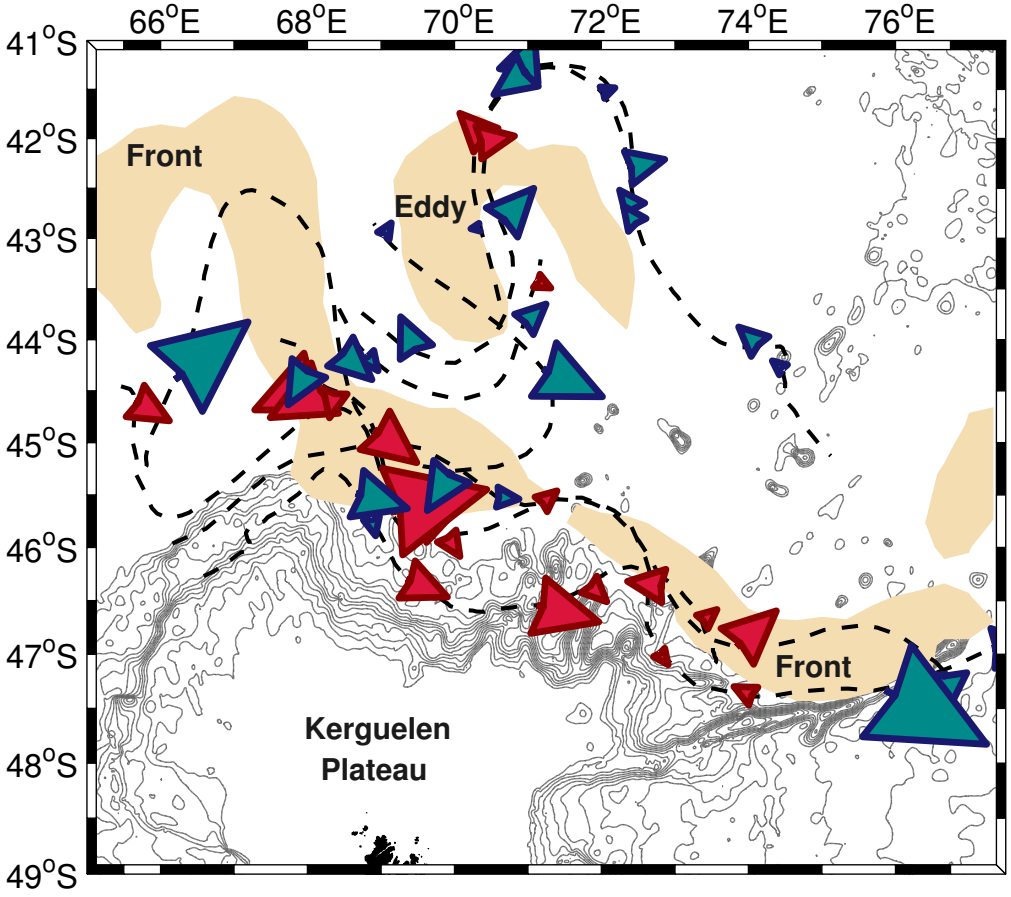

Figure 6.8: Properties of the propagation and location of coherent features over topography contours (grey). The arrow size is proportional to the horizontal intrinsic group velocity of the feature (large arrow is high group velocity) and its colour indicates the energy propagation direction (red is upward; blue is downward). Also indicated in pale brown is the mean location of the Front and the eddy during the sampling period, corresponding to mean surface geostrophic speeds of $0.38\,\mathrm{m\,s^{-1}}$ between the 18/11/2008 and the 30/01/2009. Topography contours range from 600 to 3200 m at 200 m intervals. The black dotted lines indicate the eight EM-APEX floats' trajectories.

Propagation	**Upward**		**Downward**	
Parameter	Median value	Standard deviation	Median value	Standard deviation
Depth of wave (m)	800	220	600	180
Latitude of wave (°)	46°S	2°	44°S	2°
Vertical wavelength (m)	200	66	190	65
Horizontal wavelength (km)	12	6	14	7
Period (hours)	16	1	16	3
Group velocity ($cm\,s^{-1}$)	2.6	1	3.0	1
Dissipation timescale (days)	20	23	38	49
Propagation timescale (days)	9	4	9	6

Table 6.3: Median values and standard deviations of parameters for upwards and downwards propagating internal waves.

deeper than features with downward energy propagation and appear clustered in the southern range of the sampling area (higher latitudes), closer to the Kerguelen Plateau, while features with downwards energy propagation are mostly located away from the Plateau (lower latitudes, see Table 6.3).

Observing deep upward-propagating coherent features closer to the Plateau could be the signature of internal waves generated on the seafloor through the interaction of the flow (either ACC or tidal) and rough topography. Downward-propagating coherent features are likely to be wind generated internal waves (see Section 1.2.1) but can also be the result of background wave field internal waves that have been reflected for example in a critical layer situation.

6.4.3 Distribution of the internal waves with regard to the mixing field

It is noteworthy that the location of nearly all observed coherent features matches areas of high dissipation rate as estimated with the shear-strain finescale parameterization (Figure 6.9a). This is to be expected since large amplitude features are likely associated with large vertical shears leading to large dissipation rates under the assumptions of the finescale parameterization (Chapter 4.1.2). Indeed, observing coherent internal waves in the EM-APEX data set implies large wave amplitudes (necessary for their identification). Identifying coherent features in the areas where finescale parameterization predicts higher dissipation values makes both the internal wave analysis and the shear-strain parameterization consistent with each other.

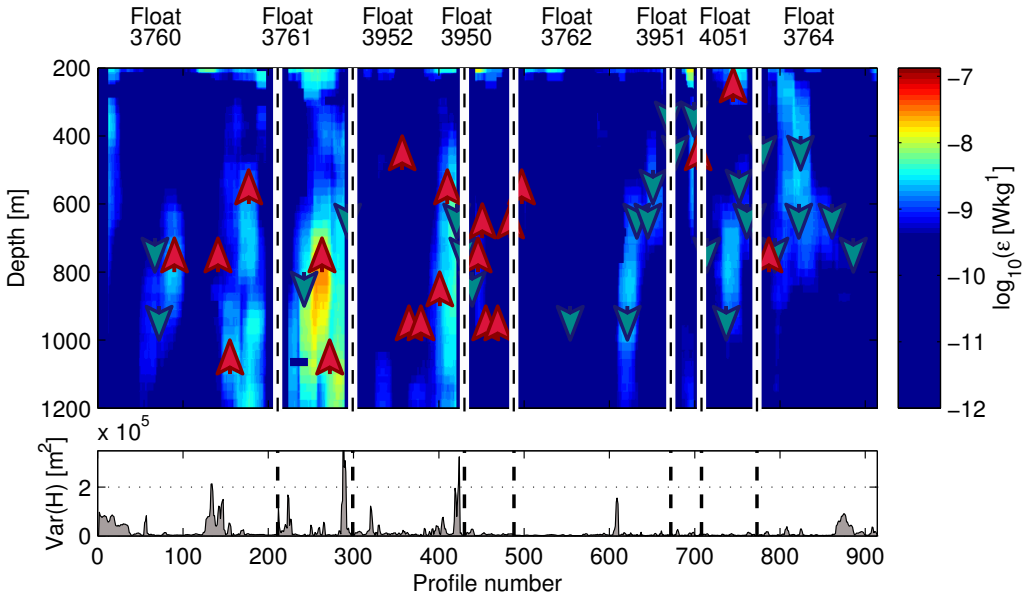

Figure 6.9: Top panel: along float trajectory distribution of the dissipation rate (ϵ). The arrows indicate both the location of the coherent wave features identified and the direction of wave propagation where red is upwards and blue is downwards. The vertical dashed lines separate floats. Bottom panel: along float trajectory topographic roughness var(H) as defined in Section 5.2.1.

To identify the potential dynamics behind the generation of the observed

coherent features, we separate the features as a function of their location: either in the Polar Front Zone, Front, eddy or Subantarctic Zone. This is done by applying definitions used in Chapter 5. The typical properties of coherent features for each region are described next (see Table 6.4).

In the Polar Front Zone, 71% of the coherent features are upward propagating. A typical feature is observed at 800 m depth and has a vertical wavelength $\lambda = 226$ m, a horizontal wavelength $\lambda_h = 15$ km and a period $T = 16$ hours. A coherent feature in the Polar Front Zone will propagate through the mean flow four times faster than it would take it to dissipate.

In the Front, nearly 38% of the coherent features are upward propagating. A typical feature is observed at 700 m depth and has a vertical wavelength $\lambda = 170$ m, a horizontal wavelength $\lambda_h = 12$ km and a period $T = 16$ hours. A coherent feature in the Front will propagate through the mean flow approximately twice as fast as it would take it to dissipate.

In the eddy, 23% of the coherent features are propagating upward. A typical feature is observed at 500 m depth and has a vertical wavelength $\lambda = 182$ m, a horizontal wavelength $\lambda_h = 18$ km and a period $T = 17$ hours, consistent with lower inertial frequencies at lower latitudes. A coherent feature in the eddy will propagate through the mean flow approximately as fast as it would take it to dissipate.

In the Subantarctic Zone, none of the coherent features are propagating upwards. A typical feature is observed at 600 m depth and has a vertical wavelength $\lambda = 131$ m, a horizontal wavelength $\lambda_h = 17$ km and a period $T = 17$ hours. A coherent feature in the Subantarctic Zone will dissipate twice as fast as it would propagate through the mean flow. Since the mean water depth in Subantarctic Zone is 3600 m and the EM-APEX sample between 200 and 1200 m, we might not sampling deep enough to observe upward propagating features.

Mean group velocities are higher in the Polar Front Zone ($C_g = 3$ cm s^{-1}) and in the eddy ($C_g = 3$ cm s^{-1}) but they are particularly low in the Subantarctic Zone ($C_g = 1$ cm s^{-1}).

The Doppler shift is one of many parameters that will impact the propagation of internal waves. The Doppler shift is an advection parameter of

Parameter	**Polar Front Zone**	**Front**	**Eddy**	**Subantarctic Zone**
Number of internal waves	17	13	13	3
Proportion of upward propagating waves	71%	38%	23%	0%
Depth of wave (m)	800	700	500	600
Vertical wavelength (m)	226	170	182	131
Horizontal wavelength (km)	15	12	18	17
Period (hours)	16	16	17	17
Doppler shift over f (rad)	0.4	1.8	0.7	0.4
Horizontal group velocity ($\mathrm{cm\,s^{-1}}$)	3	2	2	1
Dissipation timescale (days)	20	18	10	10
Propagation timescale (days)	6	7	7	17
Watercolumn depth (m)	3500	3500	3900	3800
Topographic roughness ($\mathrm{m^2}$)	15000	10500	6000	8500
Wind speed ($\mathrm{m\,s^{-1}}$)	7	8	8	10
Mean flow speed ($\mathrm{m\,s^{-1}}$)	0.2	0.4	0.4	0.2
ϕ_{CCW}/ϕ_{CW}	1	2	2	2
R_ω	6	5	7	7
Dissipation ($\mathrm{W\,kg^{-1}}$)	4×10^{-10}	15×10^{-10}	6×10^{-10}	1×10^{-10}

Table 6.4: Median values of parameters for observed coherent internal waves features as well other associated parameters separated by dynamical regions.

the flow that affects the orientation of the wave with regard to the flow: large Doppler shifts will lead to the filamentation of an internal wave in the same manner as a passive tracer will be filamented when the rate of strain exceeds the relative vorticity (Bühler and McIntyre, 2005; Polzin and Lvov, 2011). Note that both strain and vorticity refer to the spatial gradients of the advecting field. The filamentation process tends to reduce the angle between the horizontal wave vector and the flow gradients. The Doppler shift, local inertial frequency (f) and the orientation of the coherent features with regard to the flow (angular displacement) are estimated.

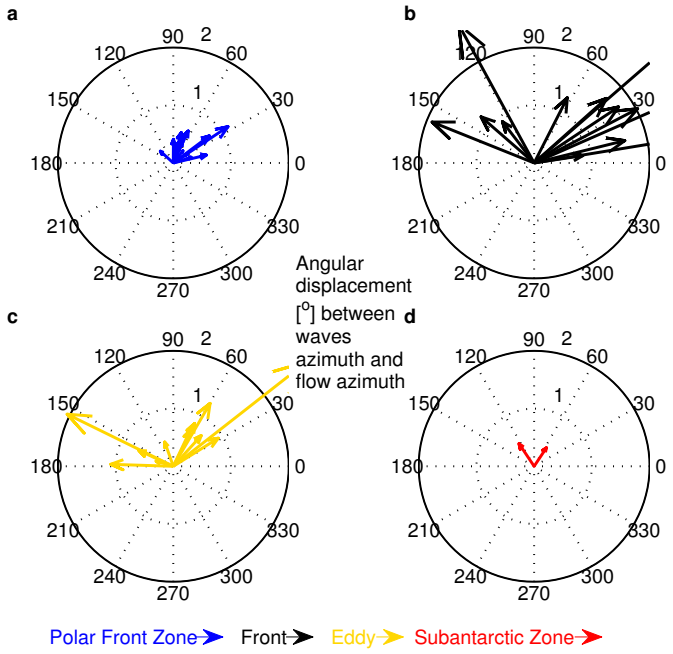

Figure 6.10: Angular displacement (°) between the wave's azimuth and the flow azimuth in the (a) Polar Front Zone, (b) Front, (c) eddy and (d) Subantarctic Zone. The magnitude of the vector is proportional to the ratio of Doppler shift over local inertial frequency (f). Internal waves with an angular displacement close to 90^o are perpendicular to flow; internal waves with an angular displacement close to 0^o are parallel to flow and the angular displacement is positive CCW from the x-axis.

A ratio of Doppler shift to f equal or larger than one suggests the Doppler shift is significant for that coherent feature. We find that the Doppler shift is especially significant in the Front, as well as in the eddy and especially low

in the Subantarctic Zone (see Table 6.4 and Figure 6.10). We also estimate the orientation of the coherent features with regard to the flow gradient (angular displacement between the features' horizontal wave vector and the local flow's horizontal velocity vector, Figure 6.10). Angular displacements close to 90° indicate the coherent feature is perpendicular to the flow while angular displacements close to 0° or 180° indicate the coherent feature is parallel to the flow. We find that particularly large Doppler shift to f ratios are associated with coherent features parallel to the flow (median angle is 30°) while small Doppler shift to f ratios are associated with coherent features near perpendicular to the flow (median angle is 70°).

The importance of the Doppler shift and interaction timescales for internal waves and mixing dynamics will be further discussed in the next section.

6.5 Internal waves and turbulent mixing

6.5.1 Shear-to-strain ratio and ratio of rotary-with-depth shear variance

The shear-to-strain ratio and the ratio of rotary-with-depth shear variance are diagnostics that have been used to analyse the internal wave field in the Southern Ocean (Waterman et al., 2013; Sheen et al., 2013). The shear-to-strain ratio (R_ω) is a measure of the internal wave field's mean aspect ratio and hence bulk frequency content (Polzin et al., 2013). Higher R_ω values imply the presence of near-inertial waves, while lower R_ω values can be attributed to the presence of more high frequency internal waves at high vertical wavenumber or the presence of shear instabilities (Polzin et al., 2003). The ratio of rotary-with-depth shear variance (ϕ_{CCW}/ϕ_{CW} in the Southern Hemisphere) is related to the dominant direction of the propagation of the internal wave energy. We remind the reader that a dominance of CCW polarization of the shear suggests downward energy propagation in the Southern Hemisphere (upward phase propagation) and a dominance of CW polarization of the shear indicates upward energy propagation (downward phase propagation).

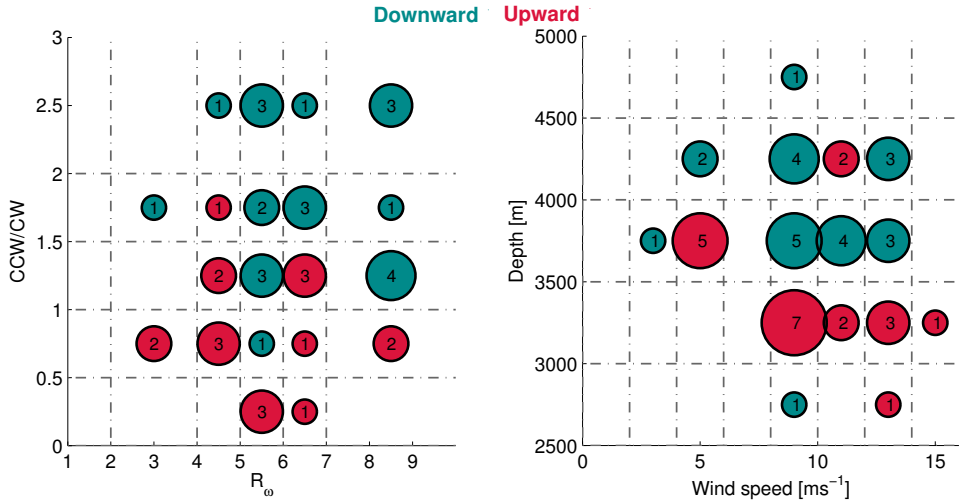

(a) (b)

Figure 6.11: Bin-average number of coherent features as a function of (a) R_ω and ϕ_{CCW}/ϕ_{CW} and (b) as a function of wind speed and total water depth at the location of the features. The color of the dot indicates the energy propagation direction of the features (red is upward and blue is downward). The number inside the circle and the size of the circle indicate the number of features in each bin.

Here we expect internal waves with upward (downward) energy propagation to be found in regions with low (high) ϕ_{CCW}/ϕ_{CW} and low (high) R_ω estimates. For each wave we identify the associated R_ω and ϕ_{CCW}/ϕ_{CW} as the mean value in the depth range of the internal wave in the centre profile of the internal wave. Internal waves with dominant upward energy propagation are found in lower ϕ_{CCW}/ϕ_{CW} conditions and marginally lower R_ω values while upward propagating internal waves are associated with higher value of both ϕ_{CCW}/ϕ_{CW} and R_ω (Figure 6.11a).

To investigate the sources of the observed internal waves, we identify the water depth and wind speed associated with each internal wave (see Section 2.3.1). In the EM-APEX data, internal waves with upward (red) energy propagation are found mostly in shallower waters and with lower wind speeds than waves with downward (blue) energy propagation which are in deeper waters and at somewhat higher wind speeds (Figure 6.11b). Being close to the Kerguelen Plateau means that shallower waters are associated with high

topographic roughness, while greater wind speeds will, to a certain extent, be associated with large atmospheric frontal events. This suggests that internal waves with dominant upward propagating energy are generated by the interaction of the flow with the rough topography of the northern edge of Kerguelen Plateau, while the waves with dominant downward propagating energy are potentially wind generated or potentially reflected from critical layer. We would expect better correlation between depth and upward propagating features with full depth sampling; the distribution of the coherent features as a function of depth and wind speed is impacted by the fact that the EM-APEX floats only sample the upper 1600 m.

6.5.2 Doppler shift impact

The EM-APEX data are consistent with the Front dynamics being dominated by Doppler shifting. Internal waves associated with large Doppler shifting tend to be aligned with the flow, while some internal wave nearly perpendicular to the flow are associated with small Doppler shift to f ratios (Figure 6.12). The latter is a characteristic of internal wave trapping (Kunze, 1985), where the relative vorticity gradient dominates the wave dynamics. Some internal waves in the Polar Front Zone and Subantarctic Zone are likely candidates for waves influenced by relative vorticity.

The local Doppler shift becomes the dominant dynamic when it is at least twice the value of the local relative vorticity. We have estimates of the Doppler shift for each wave but we can only resolve weekly mean relative vorticity fields (Figure 3.8). While the Doppler shift estimates for each internal wave range from $-40 \times 10^{-5}\,\mathrm{s}^{-}1$ to $74 \times 10^{-5}\,\mathrm{s}^{-}1$ with a mean of $11 \times 10^{-5}\,\mathrm{s}^{-}1$, the weekly mean relative vorticity in the area ranges from $-3 \times 10^{-5}\,\mathrm{s}^{-}1$ to $3 \times 10^{-5}\,\mathrm{s}^{-}1$ with a mean of $0.6 \times 10^{-5}\,\mathrm{s}^{-}1$. These estimates suggest that overall, Doppler shift processes rather than relative vorticity dominate the observed internal waves. Yet estimating the relative vorticity gradient for each internal wave would allow us to confirm which of Doppler shift or relative vorticity dominates in each wave and each dynamical region. Doppler shifted internal waves exchange more energy and

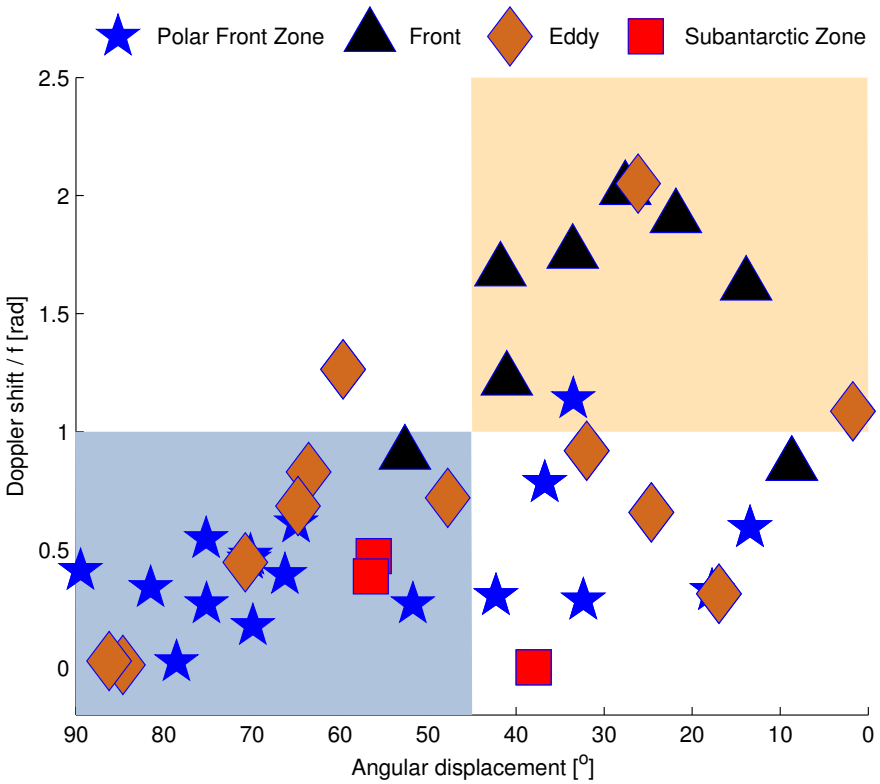

Figure 6.12: Angular displacement between the wave's azimuth and the flow azimuth vs. Doppler shift to f ratio for each internal wave. Internal waves with an angular displacement close to 90^o (waves are perpendicular to flow) and with Doppler shift to f ratio smaller than one are likely affected by relative vorticity (blue shading); internal waves with an angular displacement close to 0^o (waves are parallel to flow) and with Doppler shift to f ratio larger than one are likely dominated by the Doppler shift (red shading). The markers denote which dynamical zone internal waves belong to.

momentum with each other than trapped internal waves. In regions where the dynamics are dominated by the Doppler shift, internal waves could give rise to the divergence of momentum fluxes.

6.5.3 Interaction timescales

We find that particularly in the Front and in the Polar Front Zone, internal waves propagate away much faster than they dissipate, while in the Subantarctic Zone internal waves are likely to dissipate faster than they propagate (Figure 6.13).

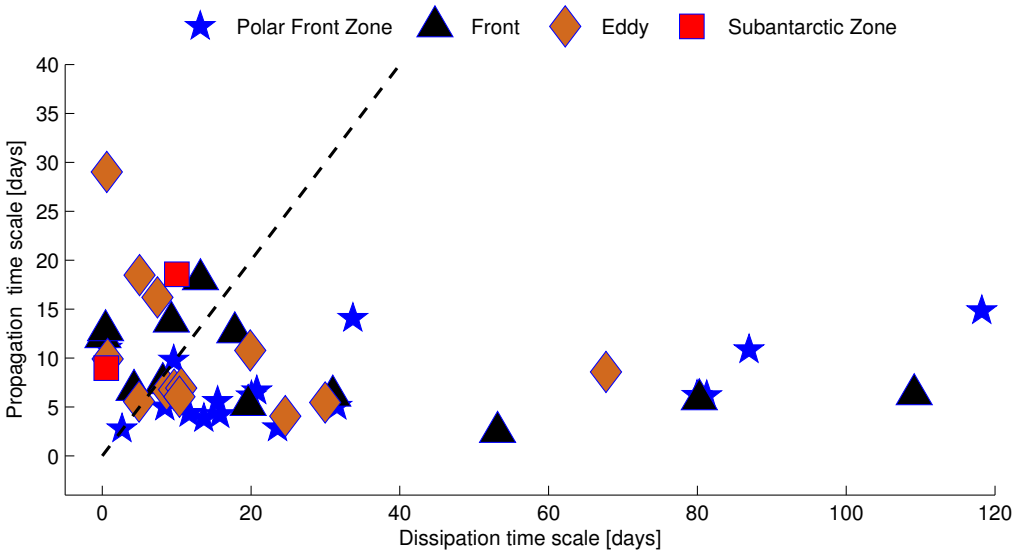

Figure 6.13: Dissipation and propagation time scales associated with the observed internal waves. The markers denote which dynamical zone internal waves belong to. Waves under the black dashed line (1:1 ratio) are more likely to propagate away from site while waves above are more likely to dissipate locally.

This local versus far-field dissipation of internal waves potentially generated near the Kerguelen Plateau has implications for the Southern Ocean stratification. Internal waves that propagate away in the Front imply that they dissipate downstream, driving far-field mixing. The EM-APEX data set strongly indicates that internal waves observed near the Kerguelen Plateau,

in particular in the Front, propagate and advect energy away from the Plateau, affecting the mixing and stratification budget downstream.

6.5.4 Regional dynamics of internal waves

Looking at the distribution of the waves in terms of location, we find that waves in the Polar Front Zone area are associated with the highest percentage of upward propagating waves and the largest dissipation timescale. The internal waves in the Front also have the highest local dissipation value and the lowest local shear-to-strain ratio. In the eddy, internal waves are observed at the shallowest depth, mostly downward propagating and associated with relatively high local dissipation values. In the Subantarctic Zone, the observed internal waves all propagate downwards, are relatively shallow, very slow, associated with high R_ω values, and associated with the lowest local dissipation values (see Table 6.4). We find that internal waves in the eddy and in the Subantarctic Zone areas are shallower and have intrinsic frequencies closer to the local inertial frequency (f). Waves in the Front and in the Polar Front Zone are deeper and have higher vertical wavelength.

This suggests that in the Front, the interaction of the topography and the strong flow generates upward propagating internal waves associated with very large values of energy dissipation while away from topography in the Subantarctic Zone, wind forcing is likely the source of downward propagating near-inertial internal waves associated with smaller values of energy dissipation. Internal waves in the eddy might be interacting with inherent properties of the eddy flow (such as its strain, shear or potential vorticity), breaking locally and enhancing local dissipation. The data do not provide information on whether it is the local tidal flow or the barotropic flow of the ACC that interacts with the topography to generate internal waves. Analysing available local moored data to estimate the tidal flow in the sampling region would help estimating the tidal contribution to turbulent mixing.

6.5.5 Topographic roughness vs. wind forcing

Upward propagating waves are associated twice as often with enhanced values of turbulent mixing ($\epsilon > 1 \times 10^{-9}\,\mathrm{W\,kgm^{-1}}$) than downward propagating waves. Making the assumptions (1) that dissipation associated with upward propagating internal waves is the result of dissipating internal waves generated by flow over rough topography and (2), that dissipation associated with downward propagating internal waves is the result of surface generated internal waves, we find that 63% of the dissipation rate observed in profiles containing internal waves is generated by topography-flow interaction, while 37% is surface driven. Note that this approach is only accounting for internal waves identified in this data set and ignores other sources of downward and upward propagating internal waves, critical layer reflection, internal scattering on topography and internal waves from the internal wave field continuum (low amplitude internal waves).

The internal wave field from the EM-APEX data might be partially biased towards internal waves in critical layer situations. We are likely to find more lower frequency internal waves in the observations since they have longer horizontal scales. Higher frequency internal waves (higher dissipation rates) have smaller amplitude and are therefore harder to identify with the method applied. Also, due to the relatively small number of internal waves being analysed, the correlations that we observe are likely not statistically robust. Analysing data resolving the full water column would certainly increase the confidence of statistics, in particular for the upward propagating internal waves in deeper waters.

6.5.6 Conclusion

The EM-APEX data set provides a unique understanding of the internal wave field spatial distribution and variations north of the Kerguelen Plateau. Internal waves observed near the Kerguelen Plateau typically have a vertical wavelength of 200 m, a horizontal wavelength of 15 km, a period of 16 hours (close to the local inertial period) and a horizontal group velocity of $3\,\mathrm{cm\,s^{-1}}$. The internal wave properties, their location and their direction of propagation

are dependant on regional dynamics, suggesting different generation mechanisms of internal waves dominate in different geographical zones. The wave field in the Front and the Polar Front Zone is more influenced by the local small-scale topography, and flow strength; the eddy wave field seems to be influenced by the large-scale flow structure, while the internal wave field in the Subantarctic Zone appears controlled by atmospheric forcing. The Front has an energetic wave field with the local dissipation rate associated with the waves at least twice as high as anywhere else in the area. Waves in the Front are Doppler shifted and propagate energy and momentum outside the region.

Analysing the internal waves in multiple dimensions (wavenumber and frequency domain) but also resolving much of the variability in the temporal and vertical wavenumber domain result in an unique perspective on the internal wave field north of the Kerguelen Plateau. The results from the analysis of 46 internal waves in the area is consistent and coherent with the previously applied mixing analysis of the same data set (see Chapter 5). In particular, the high sampling density of the EM-APEX floats in space and time over a range of dynamical regions considerably enhances the information in terms of the generation mechanisms of the observed internal waves.

Applying ray tracing theory to estimate the evolution of the wavenumber and frequency of the internal waves would provide key evidence about the sources of the waves identified in this data set. This topic will be explored in future work.

Chapter 7

CONCLUSIONS

The objective of this thesis is to investigate the sources of mixing and the properties of the internal wave field north of the Kerguelen Plateau in the Southern Ocean. Turbulent mixing being mostly attributed to the breaking of internal waves, characterising the internal wave field should further our understanding of mixing dynamics. Using novel observations from EM-APEX floats, we find that topographic roughness, mean current speed and wind speed are key factors in determining local dynamical mixing regimes. The internal wave field analysis is consistent with the mixing field analysis, with both analyses highly dependant on regional dynamics. The main contributions of this thesis are presented first. We then discuss the implications of this work for the Southern Ocean circulation as well as potential future work.

7.1 Contributions

To derive mixing we apply two methods to the EM-APEX data: the Thorpe-scale method and the shear-strain finescale parameterization (**Chapter 4**). The Thorpe-scale method, which is based on measuring density inversions, provides an overview of the distribution of turbulent overturns north of the Kerguelen Plateau but is limited by the instrument's resolution and sampling characteristics. As a result, smaller scale density inversions are significantly underestimated and the mixing estimates are inappropriate for detailed spatial and temporal analysis. The applied shear-strain finescale parameterization method relates the shear and the strain observed in the water column to the internal wave field energy levels to estimate dissipation rates. The shear-strain parameterization mixing estimates are validated with measurements from a microstructure profiler deployed in conjunction with the EM-APEX floats.

We show that observed mixing values have significant spatial and temporal variability (**Chapter 5**). Overall, the diapycnal diffusivity is slightly above typical open-ocean background levels, while enhanced diapycnal diffusivity is found close to the Kerguelen Plateau. Topographic roughness near the Kerguelen Plateau is clearly associated with higher values of mixing in

the water column. On average, mixing values are three times higher in most of the water column above rough topography. This enhanced mixing is likely the result of breaking internal waves generated by the interaction of the ACC fronts with the small-scale topographic features. We also find evidence of wind driven mixing in the upper 800 m of the water column following the passage of large atmospheric fronts (Figure 7.1).

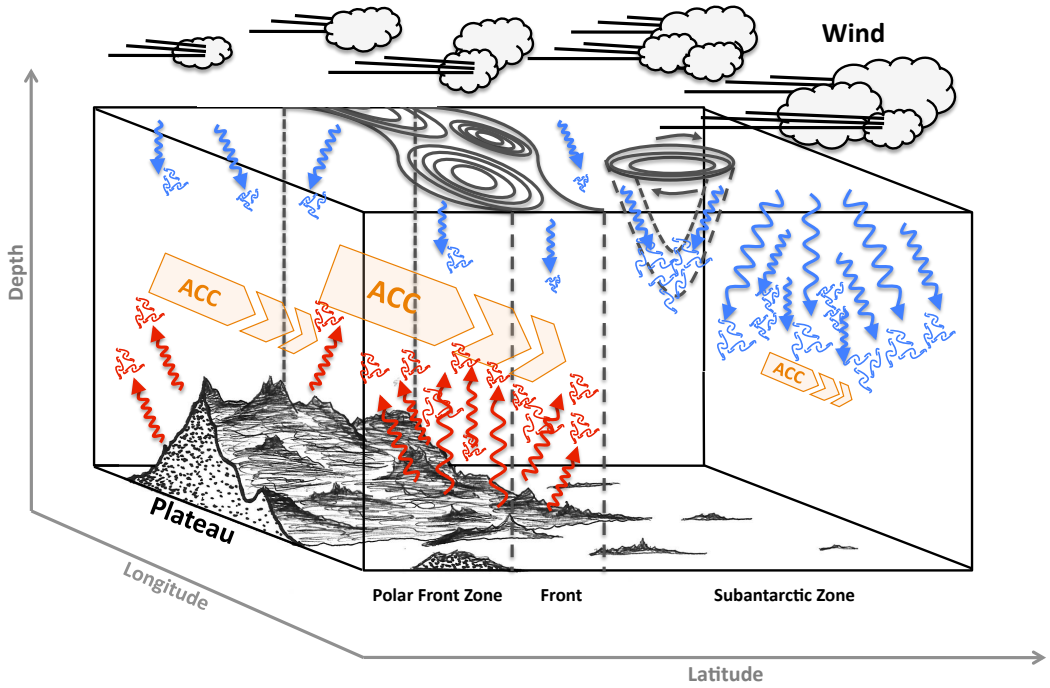

Figure 7.1: Schematic of upper water column mixing spatial distribution and associated potential mixing processes north of the Kerguelen Plateau. The Subantarctic-Subtropical Front separates two different dynamical regions. In the Polar Front Zone, mixing intensities are controlled by topographic roughness. In the Front, the flow over rough topography is clearly associated with high mixing values and upward propagating internal waves (red arrows). In the Subantarctic Zone, stronger wind forcing generates near-inertial downward propagating internal waves (blue arrows). Mesoscale eddy activity associated with enhanced mixing is observed north of the Front.

A key point is the fact that mixing is substantially enhanced within the merged SAF/STF Front. The Front separates the Subantarctic Zone (north of the Front) from the Polar Front Zone (south of the Front). The variability in mixing intensity north of, within and south of the Front suggests that

different dynamical regimes influence mixing. Most of the mixing of water masses in the upper 1600 m impacts the AAIW and UCDW and takes place in the Front and Polar Front Zone.

In the Front, we identify the interaction of a strong current with the rough topography of the Kerguelen Plateau as the source of upward-propagating internal waves associated with enhanced turbulent mixing. Maps of model estimates of energy conversion into internal waves by tides (Nycander, 2005) and by geostrophic motions (Nikurashin and Ferrari, 2011), show that both tidal motions and geostrophic motions contribute to the internal wave field in the Kerguelen Plateau region. We find that the most intense values of mixing estimates from the EM-APEX floats are in areas where energy conversion by both tides and geostrophic motions into internal waves are important (not shown). This supports the theory that enhanced mixing in the Front is the result of breaking internal waves generated by the interaction of the flow and the topography.

In the Subantarctic Zone, where the topographic roughness is weak, mixing dynamics are controlled by wind generated inertial motions. In the Polar Front Zone, where mixing is dominated by the presence of the Kerguelen Plateau and associated rough topography, weaker currents lead to less intense mixing than in the Front but more than in the Subantarctic Zone. The observation of intense bursts of mixing in an eddy highlights the potential role of relative vorticity on the dynamics of internal waves.

The shear-to-strain ratio R_ω is estimated as part of the finescale parameterization applied in this study. In strain-only finescale parameterization methods, R_ω is set as a constant. With this set of observations, we establish that the difference between applying the shear-strain parameterization with the observed R_ω and the strain-only parameterization with a constant R_ω is over an order of magnitude.

The characteristics as well as the locations of the internal waves and their direction of propagation are dependant on regional dynamics (**Chapter 6**). The Front has an energetic wave field with wave-associated local dissipation rates at least twice as high as anywhere else in the area. Internal waves observed near the Kerguelen Plateau typically have a vertical wavelength of

200 m, a horizontal wavelength of 15 km, a period of 16 hours (close to the local inertial period) and a horizontal group velocity of $3\,\mathrm{cm\,s^{-1}}$. Waves in the Front are Doppler shifted and likely to propagate energy and momentum outside the region. Based on the direction of propagation of the observed internal waves, we suggest that most of the dissipation rate (63%) is generated by the interaction topography and flow, while a smaller fraction (37%) is surface driven.

7.2 Implications

The findings from this work have important implications for our understanding of Southern Ocean mixing dynamics and for parameterization of mixing in climate models. First, we have established that mixing in the Southern Ocean is highly temporally and spatially variable. This reinforces the inadequacy of standard approaches to model mixing in climate models, where uniform global mixing is traditionally assumed. We find a significant correlation between depth integrated diapycnal diffusivity and topographic roughness ($R = 0.74$), a first step towards better parameterizing topography driven mixing in numerical models.

Secondly, better constraining the spatial distribution of the shear-to-strain variance ratio would considerably improve strain-based parameterizations of the dissipation rate. We highlight that the uncertainties associated with the strain-based parameterization when $R\omega$ observations are not available are likely underestimated.

This work also suggests that bottom generated internal waves potentially play a bigger role in enhancing local turbulent mixing than downward propagating internal waves. This finding goes against the traditional view of mixing from surface-forced internal waves.

The ratio of rotary-with-depth shear variance (ϕ_{CCW}/ϕ_{CW}), can be used to infer the dominant direction of energy propagation of rotationally effected internal waves (Leaman and Sanford, 1975). A dominance of CCW polarization of the shear suggests predominantly downward energy propagation in the Southern Hemisphere (upward phase propagation) and a dominance

of CW polarization of the shear indicates that upward energy propagation dominates (downward phase propagation). The distribution of ϕ_{CCW}/ϕ_{CW} patterns has been used in previous studies to investigate possible sources of internal internal wave energy, in particular when contrasting wind-generated waves to bottom-generated waves (Waterman et al., 2013; Sheen et al., 2013; Brearley et al., 2013). It appears that while regions with large values of ϕ_{CCW}/ϕ_{CW} match well areas of high dissipation rate and the location of downward propagating internal waves, regions with low ϕ_{CCW}/ϕ_{CW} values fail to overlap areas of enhanced dissipation rate and often miss the location of upward propagating internal waves (not shown). This would lead to an under-representation of upward propagating internal waves when using the distribution of ϕ_{CCW}/ϕ_{CW} as a diagnostic for up versus down energy sources. Such under-representation of upward propagating internal waves is observed in particular in the Front, where we suggest that observed intense mixing is driven by the the interaction of the flow and the topography and where upward-propagating internals waves are observed but where ϕ_{CCW}/ϕ_{CW} indicates downward energy propagation.

This work suggests that under certain conditions, conventional tools for identifying the relative importance between upward and downward propagating internal waves, such as the ϕ_{CCW}/ϕ_{CW} ratio, might not be adequate for upper-ocean data set with waters shallower than 2000 m. Instead, we suggest using the analysis of individual coherent internal wave properties as a complementary diagnostic when assessing the impact of surface or bottom generated waves.

The observed interaction of internal waves with an eddy leads to questions about the possibility of energy transfer between the eddy and the internal wave field, ultimately leading to energy dissipation. With the possible increase of wind stress and therefore eddy field energy in the Southern Ocean (Meredith and Naveira Garabato, 2012) over the coming decades, will the eddy contribution to the mixing increase as well?

In the context of the Southern Ocean overturning circulation, we infer the diapycnal transformation rate of water-masses in the upper 1600 m in terms of potential density using our in situ estimate of diffusivity. Following

the water-mass transformation framework developed by Walin (1982), the diapycnal volume flux or transformation D is defined as

$$D(\rho) = -\frac{1}{\delta\rho}\int_{\rho} K_{\rho}\frac{\partial\rho}{\partial z}dA, \tag{7.1}$$

where K_ρ is the observed diffusivity at the density level (ρ), $\partial\rho/\partial z$ is the observed gradient in density around K_ρ, and A is the area of the density surface (ρ) based on the World Ocean Atlas (Levitus and Boyer, 1994). We first apply Eq. (7.1) to the Kerguelen Plateau region ($40°S - 50°S$ and $67°E - 78°E$), estimating the diapycnal transformation for the Subantarctic Zone, the SAF/STF front, and the Polar Front Zone (Figure 7.2a). Our observed diffusivities in the Kerguelen region lead to a peak in transformation in the SAF/STF front of 0.28 Sv at ρ =27.5 kg m^{-3}, which is the boundary between AAIW and UCDW. We scale the inferred diapycnal transformation to the entire Southern Ocean ($40°S - 63°S$), using the observed diffusivities from the Kerguelen Plateau region (Figure 7.2b). The resulting diapycnal transformation estimates are significant for the Southern Ocean overturning circulation budget with an overall value of 20 Sv of transformation on denser waters along the 27.5 kg m^{-3} isopycnal surface, of which 17 Sv takes place in the SAF/STF front. These results suggest that water-mass transformation is dominant in the frontal zone, over rough topography, at the boundary between UCDW and AAIW. Enhanced transformation in the front is consistent with recent work (Badin et al., 2013) and previous studies showing enhanced mixing in frontal regions (e.g. Sloyan, 2005; Naveira Garabato et al., 2007; Thompson et al., 2007; St. Laurent et al., 2012a). This supports evidence that topographic features and the Antarctic Circumpolar Current play a significant role in the Southern Ocean overturning circulation budget.

The analysis of the internal wave properties has far reaching implications (Chapter 6). Whether the observed internal waves are controlled by Doppler shift dynamics or relative vorticity dynamics has consequences for the regional divergence of momentum and therefore the Southern Ocean momentum balance. Stratification in the Southern Ocean and its overturning circulation is affected by far-field forced internal waves that have propagated

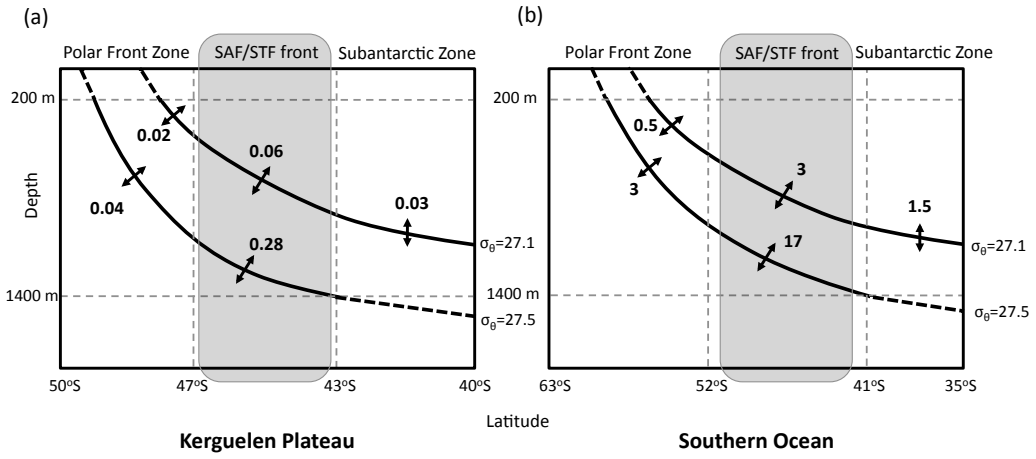

Figure 7.2: Schematic of the inferred diapycnal transformation rates for (a) the Kerguelen Plateau region ($40°S - 50°S$ and $67°E - 78°E$) and (b) scaled to the entire Southern Ocean ($40°S - 63°S$). The transformation rates are based on estimates of diffusivity from the EM-APEX floats and the area of density surfaces from the World Ocean Atlas (Levitus and Boyer, 1994). The latitudinal boundaries of the Polar Front Zone, the SAF/STF front (highlighted in grey) and the Subantarctic Zone boundaries are shown (grey dashed line). Transformation rates as inferred in the sampling range of the EM-APEX floats between 200 m and 1400 m. Transformation rates are in Sverdrups ($1\,\mathrm{Sv}{=}10^6\mathrm{m}^3\mathrm{s}^{-1}$) and density surfaces ($\rho_\theta$) are in kilograms per cubic meter.

away from generation sources. Associating the Doppler shift with wave-mean interaction timescales, highlights the fact that the role of the Front in advecting internal wave energy and momentum away from generation site is important and needs to be quantified.

This thesis highlights the importance of high density observations and the significance of local dynamics. Clearly, the role of local dynamics in the generation of internal waves and therefore in the distribution and intensity of mixing requires more attention. Our understanding of the ocean general circulation and ultimately its representation in ocean models will depend on our knowledge of local dynamics.

7.3 Future work

There are a few limitations in this study and many questions that can be addressed in future work.

In terms of limitations, higher resolution topographic and wind data would likely improve our ability to quantify the impact of the mixing sources. Beside the Smith and Sandwell topographic data set, methods exist to estimate regional small-scale topographic roughness (Nikurashin and Ferrari, 2011). Such estimates of roughness would likely better correlate with topography driven mixing. Higher resolution wind data would permit to estimate wind work and quantify the impact of wind forcing on the estimated turbulent mixing.

We have seen evidence of enhanced mixing above topographic roughness and deduced that it is the result of the strong flow of the ACC interacting with Kerguelen Plateau. Another possibility is that tidal motions also interact with the Plateau. Quantifying the contribution, if any, from tides could be done by analysing mooring data collected simultaneously with the EM-APEX data.

This thesis suggests that Doppler shift is a dominant dynamic in the merged frontal jet. Weekly estimates of the relative vorticity are too low in resolution to establish the relative balance between Doppler shift and vorticity dynamics in regions surrounding the frontal jet. In the upper 400 m of a cyclonic eddy, the observed intense mixing values could be the result of dissipating internal waves that are trapped due to strong relative vorticity gradients. Ascertaining the importance of the relative vorticity would confirm this theory. The potential implications on the dynamics of the Southern Ocean mesoscale eddy field are important and should be investigated.

Many of these findings depend on the origins of the observed internal waves: Are they generated at the sea-floor or at the ocean surface? Are they the result of wave-wave interactions? The estimated properties of the internal waves provide strong clues on their origins and ray tracing of these internal waves could further validate our conclusions. We plan to explore ray tracing methods and apply them to this data set in the future.

Appendices

Appendix A

SYMBOLS AND NOTATIONS

The list below contains most of the parameters and variables used in this document with their equivalent symbol, units and value if appropriate.

a	Empirical constant of proportionality = 0.8	48
A_{wind}	Maximum wind area (km^2)	87
b	Vertical stratification scale =1300 m	56
C_g	Group velocity (ms^{-1})	107
ϕ_{CCW}/ϕ_{CW}	Ratio of CCW to CW rotating shear variance	59
d	Vertical displacement (m)	47
ϵ	Turbulent kinetic energy dissipation rate (Wkg^{-1})	3
ϵ_0	GM76 dissipation rate = 8×10^{-10} W kg^{-1}	55
E_0	Dimensionless energy = 6.3×10^{-5}	56
E_K	Kinetic energy (kg m^2 s^{-2})	105
E_P	Potential energy (kg m^2 s^{-2})	105
E_{cw}	Velocity variance in clockwise component	105
E_{ccw}	Velocity variance in counterclockwise component	105
f	Coriolis or inertial frequency = $2\mathbf{\Omega} sin(\Phi)$ s^{-1}	11
f_0	GM76 inertial frequency = 7.86×10^{-5} s^{-1}	55
Γ	Mixing efficiency = 0.2	48
g	Acceleration due to gravity $\simeq$ 9.81 ms^{-2}	42
$j*$	Mode number scale = 3	56
K_ρ	Diapycnal turbulent eddy diffusivity of mass (m^{2}s^{-1})	3
$\mathbf{k}$	Horizontal wave vector	104
k_h	Horizontal wavenumber (cpm)	103
L_{Ro}	Rossby Radius of deformation (m)	114
L_O	Ozmidov scale (m)	48
L_T	Thorpe scale (m)	47
λ	Wavelength (m)	110
λ_c	Cutoff wavelength (m)	57
λ_0	Minimum limit integration wavelength (m)	57
m	Vertical wavenumber (cpm)	103
m_c	Cutoff vertical wavenumber (cpm)	55
m_0	Minimum vertical wavenumber (cpm)	55
N	Buoyancy frequency = $10^{-2} - 10^{-4}$ rad s^{-1}	55

Appendix B

Australian Argo Delayed Mode Quality Control (DMQC) Processing: a complete example

We present step by step an example for float 3761 of the DMQC procedure applied to all float data profiles. Float 3761 is identified with its World Meteorological Organisation (WMO) ID number "1901136". All the necessary codes and scripts needed to run this DMQC procedure are located at: $/argo/ArgoDM/src$

Obtain source files

Using the routine $get\_next\_batch(1901136, 0, [0\ 1])$, we copy the data files to our working directory. We check that the correct files were created and profiles copied across to:
$\sim /data/dmode/0dmqc/1901136/$ and
$\sim /data/dmode/1gilson\_first/1901136/$.

List and separate parked profiles

With the routine $pre\_gilson(1901136, [], 0)$, we can identify profiles that have a parked period. Going through each profile, we make note of the profiles numbers where with a parked period. We create a $park\_profiles$ folder in $\sim /data/dmode/0dmqc/1901136/$ and profiles with a parked period are added to this folder. These parked profiles are not quality controlled.

Generate raw data plots

Using the routine $plot\_dmqc\_flags(1901136, [1\ 2\ 3], [0])$, we plot the raw data to familiarise ourselves with it.

Flag bad pressure

The $pre\_gilson(1901136, [], 1)$ routine identifies bad pressure points, profile by profile. We check each suspect points (red data points on Figure B.1), and make a decision whether to flag them or not.

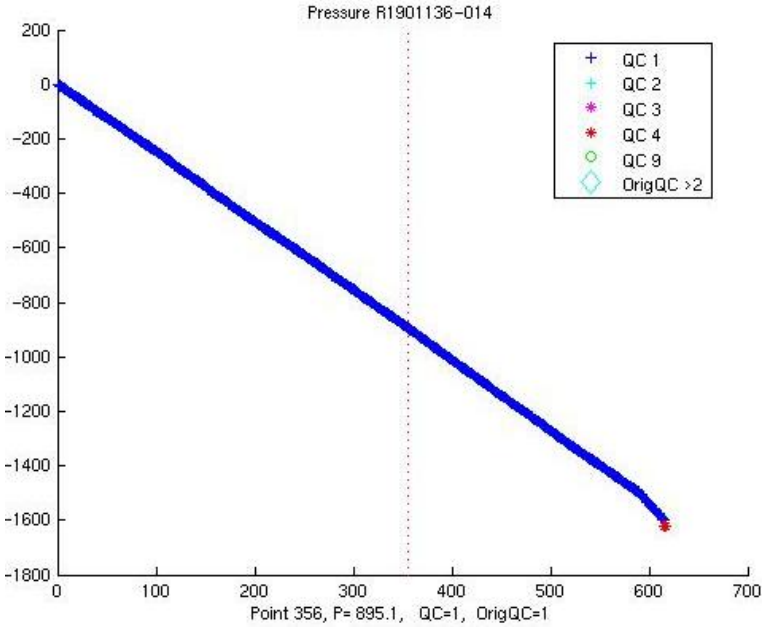

Figure B.1: Pressure on the y-axis and sample points on x-axis of profile 14. Blue denotes good data (QC1), while red denotes bad pressure points (QC4).

Generate float trajectory plot

Next we generate a plot showing the trajectory of the float using the routine $where\_argo\_edit(1901136)$. The figure generated by the routine has two subplots; we zoom in on the bottom subplot and save a copy of that subplot as:

$\sim$ $/pub\_web/dmqc/dmqc\_notes/1901136/plots/argo\_loc\_1901136\_alt.jpg$.

We also crop the figure to only show the lower subplot and save it as:
$\sim$ $/pub\_web/dmqc/dmqc\_notes/1901136/plots/argo\_loc\_1901136.jpg$.

Obtain float characteristics

Typing $load \sim /data/csiromat/A1901136.mat$ accesses the float's characteristics. By typing $fl = floatinfo(1901136)$ we obtain the float launch date and the serial number of the CTD and pressure sensors; by typing $fl.sensor$, $fl.sensor\_model$ and $fl.sensor\_sn$, we access the sensor's name, type and model.

Generate raw data T-S diagram

The routine $plot\_ts(float, 0)$ generates a figure with a T-S diagram, a plot of the maximum temperature recorded for each profile against "year day" and a plot of the sea surface salinity for each profile against "year day". This figure is saved as:

$\sim$ /*pub_web*/*dmqc*/*dmqc_notes*/1901136/*plots*/*TS*_1901136.*jpg*.

We then crop the T-S diagram and zoom on the deeper waters (Figure B.2) to save it as

$\sim$ /*pub_web*/*dmqc*/*dmqc_notes*/1901136/*plots*/*TS*_1901136_*deep.jpg*.

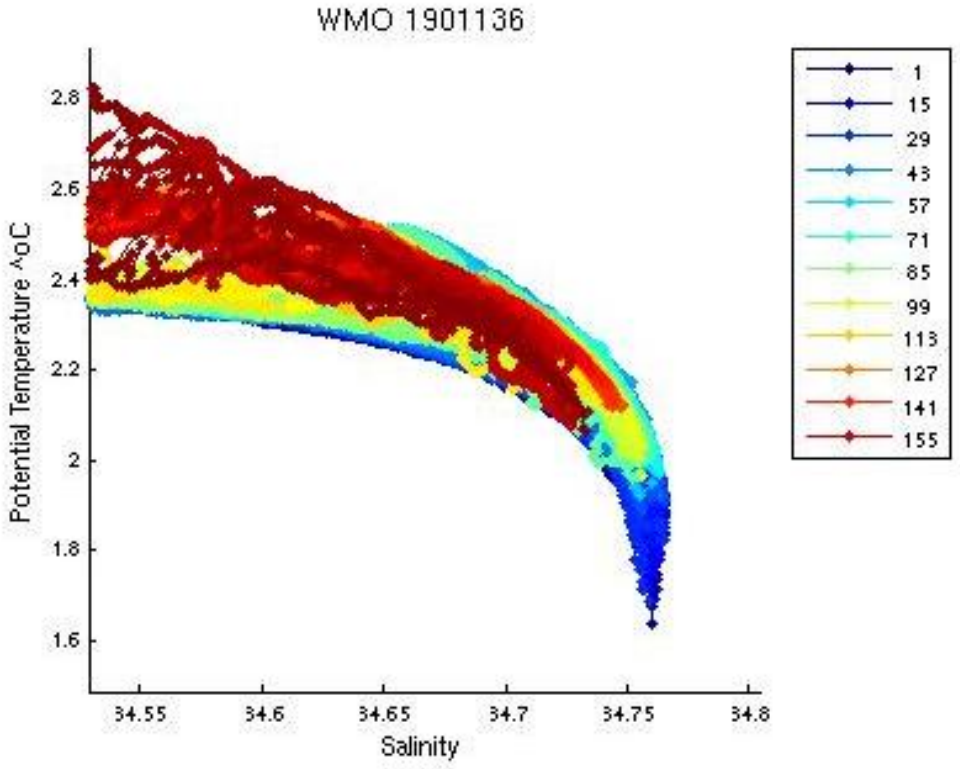

Figure B.2: Plot of potential temperature versus salinity of all the profiles for float 1901136. Colours denote the profile numbers where blue hues are the first profiles and red hues are the last profiles of the float.

Generate T-S diagram comparison with nearby argo data

To compare float 1901136 T-S data with other float's T-S data, we use $plot\_ts\_nearby(1901136, 0, 1, 1, 500)$. This routine searches nearby profiles (in space and time) from other floats, producing a figure with a map of the location of the identified profiles as well as a T-S diagram of all the profiles. In Figure B.3, the black points represent the profiles from float 1901136 while other colour points are profiles from other floats listed in the legend.

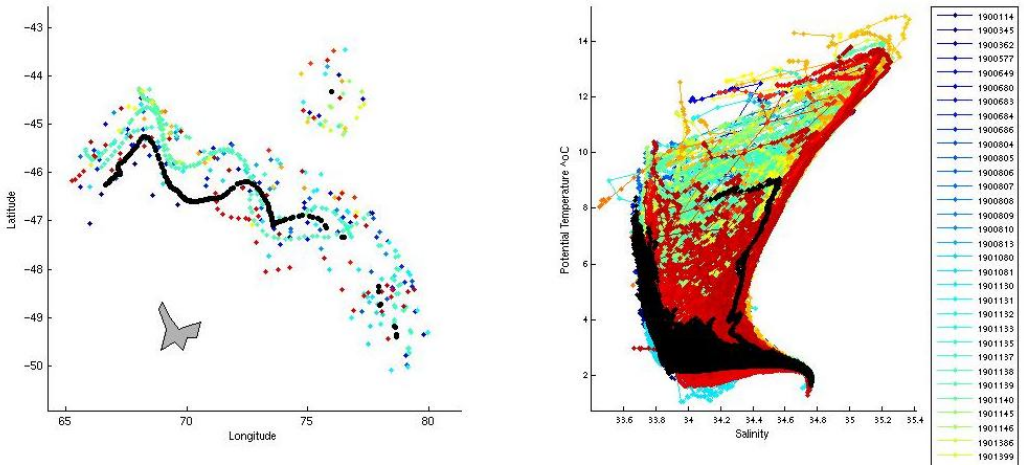

Figure B.3: Float 1901163 T-S data comparison with other nearby float data: (a) Location of float 1901136 profiles (black dots) and profiles of all other nearby floats (colour dots); and (b) T-S diagram of the profiles of float 1901136 (black dots) as well as of the profiles of all the other nearby floats (colour dots).

A copy of the figure is saved as:

$\sim$ /*pub_web*/*dmqc*/*dmqc_notes*/1901136/*plots*/*TS*_1901136_*nearby.jpg*. We then zoom on the T-S diagram deeper waters and save that subplot as:

$\sim$ /*pub_web*/*dmqc*/*dmqc_notes*/1901136/*plots*/*TS*_1901136_*nearby_deep.jpg*. The T-S diagram on Figure B.3(b) shows that our float T-S data (black) is well contained within the other floats T-S data (colour), making it unlikely that entire profiles have corrupted data.

Generate temperature, salinity and density section plots

With the routines $[fgrid, junk] = gridfloat(float)$ and $plot\_gridfloat(fgrid)$, we generate temperature, salinity and density section plots. We save a copy of each figure at the following location before pressing "enter" to see the next one:
$\sim$ /*pub_web/dmqc/dmqc_notes*/1901136/*plots/pt*_1901136.*jpg*
$\sim$ /*pub_web/dmqc/dmqc_notes*/1901136/*plots/pt*_1901136_*sur.jpg*
$\sim$ /*pub_web/dmqc/dmqc_notes*/1901136/*plots/sal*_1901136.*jpg*
$\sim$ /*pub_web/dmqc/dmqc_notes*/1901136/*plots/sal*_1901136_*sur.jpg*
$\sim$ /*pub_web/dmqc/dmqc_notes*/1901136/*plots/sig*_1901136.*jpg*
$\sim$ /*pub_web/dmqc/dmqc_notes*/1901136/*plots/sig*_1901136_*sur.jpg*
where "pt" is for potential temperature, "sur" for surface, "sal" for salinity and "sig" for density.

Identify salt hooks

The routine $toss\_deepestvals\_apex(1901136)$ automatically identifies salt hooks in the data set. The details are logged in a file by using the "diary" function before applying the salt hook routine[1]. If it says "processing 0 profiles", it means that no salt hooks were identified. Looking at the log, we check that the "max pressure" is approximately 1600 dbar for each profile (and not 2000 dbar as with Argo floats).

Identify density inversions

We use the routine $plot\_profiles\_single(1901136, 0)$ to look at each profile one by one for density inversions. The routine automatically flags density inversion based on a density inversion criteria of 0.004. Using our knowledge of the instrument (salinity sensor resolution is 0.01-0.005 and temperature sensor resolution is 0.002) and understanding of local water characteristics, we decide whether or not the flagged density inversions are legitimate or spurious. For example, profile 180 at 931 dbar has a suspicious salinity spike

[1] $diary('\sim$ /*pub_web/dmqc/dmqc_notes*/1901136/*plots*/1901136_*strip_drift.log*$')$

(Figure B.4). We make note of the location of spurious density inversions (profile number, variable and depth) to be able to flag the bad data point later on.

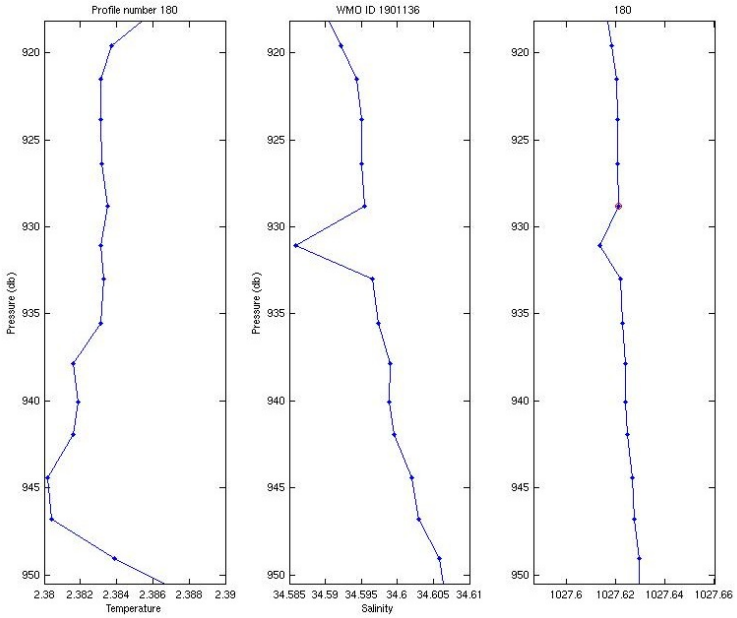

Figure B.4: Vertical profiles of (a) temperature, (b) salinity and (c) density from float 1901136, profile 180.

Flag data and apply QC

To be able to flag bad profiles or single bad data points, we run the following script: *edit_netcdf_first_intercomp* 1901136. We call up the "T-S" plot window and the "Lat/Lon" plot window. On the Lat/Lon window, we click "BthB" to have the bathymetry plot. We save a copy of this plot as:
$\sim$ */pubweb/dmqc/dmqc_notes/*1901136*/plots/lat_lon_*1901136*.jpg*.
We click "SltB" to obtain the climatological salinity plot and save this it as:
$\sim$ */pubweb/dmqc/dmqc_notes/*1901136*/plots/lat_lon_sal_*1901136*.jpg*. We go to index and click on "zero index". We want to inspect all the temperature profiles and all the salinity profiles. We are looking for profiles that stick out of the envelope. When we identify a suspicious profile, we click on it and zoom in on various plots to see if there is an explanation. If it is bad data, we click

on the bad data point, then click on the "1good" menu and choose "4bad", then click on "Cng_Qc". This flags that data point as a bad data point. If we want to quality control a whole profile, we click "CupQC" to select all the above data points. There is the option of flagging both temperature and salinity or just temperature or just salinity ("QC Fw").
When finished, we need to change the the data state for all profiles: Click "action" and "open". The action window displays: "D state= Data state =2B A = Real time data and real time adjusted data". Click on "StateM..." (top left) and the data state changes to "2CA". Then we hit "save" on profile window (click once only) and check in the background that all the profiles are being saved. Once it is done, we click "quit". We only update the data flags status when we are happy that we have done all the previous steps properly using the following script: $gilson1ed(1901136)$. This changes the file prefix type from "R" to "G", indicating that the file has gone through the first step of quality control.

Generate raw and flagged data plots

The routine $plot\_dmqc\_flags(1901136, [1\ 2\ 3], [0\ 1])$ generates plots of raw data, flagged data and the difference between raw and flagged for temperature, salinity and density. These plots are automatically saved in given directories.

Pressure drift correction

The pressure sensor on the floats can develop an bias over time leading to a drift in the measured pressure values. This drift is most easily identified in the surface pressure measurements. When the float is at the surface where the pressure should be zero, we can look at the recorded pressure to compare it to its theoretical value (Figure B.5). We then apply the surface pressure offset correction to the float $surf\_pres\_cor(1901136, [], 1, 1, 0)$ and save the output figure as:
$\sim /pub\_web/dmqc/dmqc\_checks/surf\_press/spcor\_1901136.jpg$.

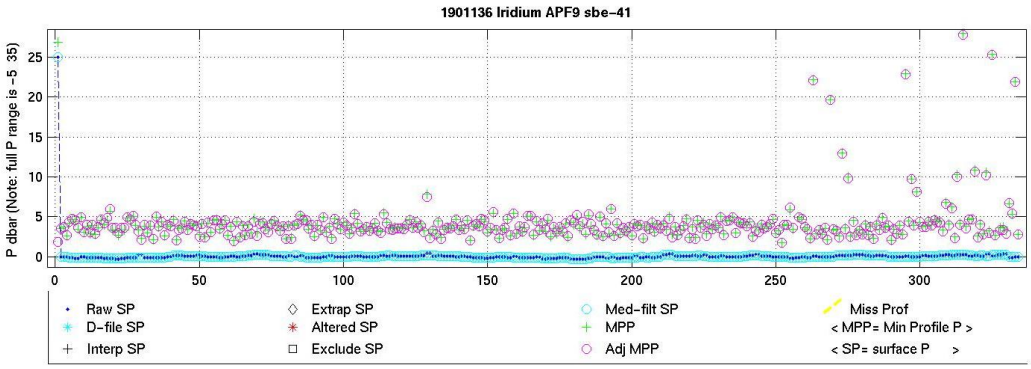

Figure B.5: Raw surface pressure of each profile and other key parameters to diagnostic the pressure drift correction for float 1901136.

Thermal lag correction

We apply a cell thermal lag correction to salinity following citetJohnson:2007: $thermal\_lag(1901136)$. We check that the correction has been applied by running: $plot\_dmqc\_flags(1901136, [1\ 2\ 3], [0\ 1\ 2\ 5])$.

Assess salinity drift

We create plots that will allow us to determine whether or not the salinity sensor is drifting.
First we generate a plot of salinity anomalies with 3 different climatologies on potential temperature surfaces: $plot\_s\_anom(1901136)$(Figure B.6). We save a copy of the figure after resizing at:
$\sim /pubweb/dmqc/dmqc\_checks/anomalies/pt\_s\_anom\_1901136.jpg$
We zoom in on bottom subplot to check accuracy ± 0.01. We also generate a set of salinity plots that uses data from nearby Argo floats where salinities are plotted on various potential temperature surfaces: $nearby\_salt(1901136, 1, 1, 1000)$
We resize Figure B.3 and save it as:
$\sim /pub\_web/dmqc/dmqc\_checks/nearby\_salt/raw/1901136\_loc.jpg$.

We stretch the figure horizontally and click with cursor on figure and press "return". This will go up one potential temperature surface level. We are looking for our float (black points) to be well within the envelop of the other floats and climatologies. We then select the plot with the po-

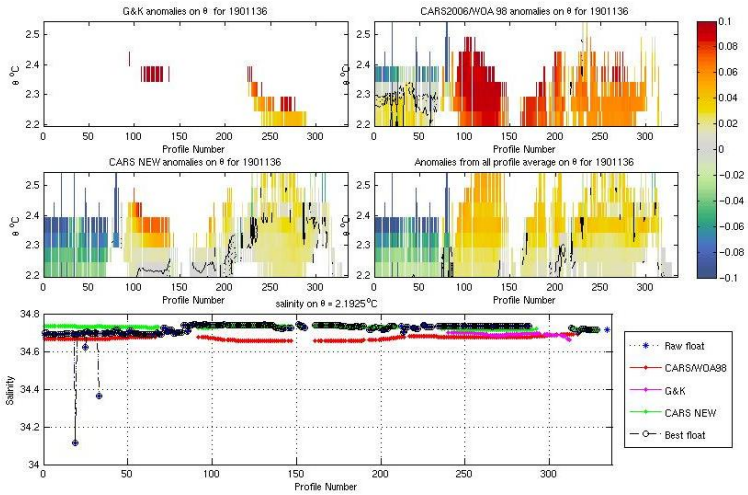

Figure B.6: The four contour plots show the temperature anomaly of each profile from float 1901136 with three climatologies and with the mean from float 1901136. On the contour plots, white means that no data were available. The bottom plot shows the salinity at each profile location at the potential temperature level of $\theta = 2.1925°C$, for float 1901136 (black crosses), and the three climatologies (colour diamonds).

tential temperature surface that best describe the data and save it under:
$\sim$ */pub_web/dmqc/dmqc_checks/nearby_salt/raw/*1901136*_data.jpg*
and if two data plots are necessary to illustrate, then save the second as:
$\sim$ */pub_web/dmqc/dmqc_checks/nearby_salt/raw/*1901136*_data_alt.jpg*

Update scientific calibration files, fields and comments

We write scientific calibration comments into a database that stores information about the quality control and error values by running the following routine: *edit_dm_db*(1901136). Say "n" to the first question and type [1:334] to cover all profiles; then select "11" on the drop down list for the float type (Apex EM APF9) and click "ok apply". Finish by typing [0].

We copy files from original directories into new directories and standardise fields as well as add comments: *apply_ow*(1901136) and type "y" to run routine.

Final check and flagging of data

This is the final check of data before completion of the quality control and submission of T,S profiles to the QC Argo database. There should not be any major problem with the data at this point. We use the following routine: *edit_netcdf_final_gilson*. Enter WMO ID: "1901136" and click on "*action*" and "*open*" and change the data mode from "2CR" to "2CD" by clicking once the bottom left button "*ModeM*". Then, we hit "save" on profile window (click once only) and monitor that the file is saved correctly in the background.

Update calibration comments

We update the float with records stored in the '*edit_dm_db*' database using the routine: *update_calib_comments*(1901136). We can check the file by typing:
$ncload \sim /data/dmode/4gilson\_final/1901136/profiles/D1901136\_30.nc$
$SCIENTIFIC\_CALIB\_COMMENT$.

Update error values and calibration date

We standardise the error values and update the calibration date in the netcdf files: $prepare\_final\_files(1901136)$.

Final check plots

We undertake a final overview of the files that are about to be submitted to the Argo database using the routine: $plot\_dmqc\_flags(1901136, [1\ 2\ 3], [0\ 1\ 2\ 5\ 3\ 4])$. Copies of the figures are saved in
$\sim /pub\_web/dmqc/dmqc\_checks/D\_files$.

Check ranges of data

We run the data through a series of range checks. This uses climatologies to determine expected properties ranges. It is conservative and we check the flagged values using the following routine: $range\_checks(1901136, 4, [])$.

Generate the html file

The final task is to generate an html file for that float that will be upload to the CSIRO DMQC website[2]. To set the right permission on figures, we type "$chmodgo + rx * .*$" in each of the following folders:
$cd \sim /pubweb/dmqc/dmqc\_checks/D\_files$
$cd \sim /pubweb/dmqc/dmqc\_checks/nearby\_salt/raw$
$cd \sim /pubweb/dmqc/dmqc\_checks/anomalies$
$cd \sim /pubweb/dmqc/dmqc\_checks/surf\_press$
Then we change directory and generate file:
$cd \sim /pub\_web/dmqc/html$ and $Float\_doc\_master\_generate$(1901136)
We check the generated file by opening it in web browser and textpad:
$\sim /pub_web/dmqc/html/DMQCnotes_$1901136.$html$
We edit the html file to correct and add fields:
$editDMQCnotes_$1901137.$html$
- Change the profile depth from 2000 m to 1600 m;
- Add serial numbers of instruments;
- Add the launch date: dd-mm-yyyy;
- Add the number of profiles;
- Resize plots where needed.

[2] (*http://www.cmar.csiro.au/argo/dmqc/html/Argo_DM.html*)

Appendix C

DERIVATIONS

C.1 Deriving the internal wave equation

The momentum equations in Cartesian coordinates on the f plane are

$$\frac{\partial u}{\partial t} - fv = -\frac{\partial p}{\partial x}, \tag{C.1}$$

$$\frac{\partial v}{\partial t} + fu = -\frac{\partial p}{\partial y}, \tag{C.2}$$

$$\frac{\partial w}{\partial t} = -\frac{\partial p}{\partial z} - \rho\frac{g}{\rho_0}. \tag{C.3}$$

The density equation is

$$\frac{\partial \rho}{\partial t} + w\frac{\partial \rho}{\partial z} = 0, \tag{C.4}$$

The continuity equation is

$$\frac{\partial u}{\partial x} + \frac{\partial v}{\partial y} + \frac{\partial w}{\partial z} = 0. \tag{C.5}$$

The buoyancy equation is

$$-\frac{g}{f}\frac{\partial \rho}{\partial z} = N^2, \tag{C.6}$$

and we define

$$\nabla^2 = \frac{\partial^2}{\partial x^2} + \frac{\partial^2}{\partial y^2} \tag{C.7}$$

so that

$$\nabla^2 p = \frac{\partial^2 p}{\partial x^2} + \frac{\partial^2 p}{\partial y^2}. \tag{C.8}$$

First, we want remove the vorticity terms

We can rewrite (C.5) as

$$f\frac{\partial w}{\partial z} = -f\frac{\partial u}{\partial x} - f\frac{\partial v}{\partial y}. \tag{C.9}$$

We then take the derivative of (C.1) with respect to y and assume f constant

$$\frac{\partial^2 u}{\partial t \partial y} - f\frac{\partial v}{\partial y} = -\frac{\partial^2 p}{\partial y \partial x}, \tag{C.10}$$

$$f\frac{\partial v}{\partial y} = -\frac{\partial^2 p}{\partial y \partial x} - \frac{\partial^2 u}{\partial t \partial y}, \tag{C.11}$$

and take the derivative of (C.2) with respect to x

$$\frac{\partial}{\partial x}(\frac{\partial v}{\partial t}) + \frac{\partial}{\partial x}(fu) = -\frac{\partial}{\partial x}(\frac{\partial p}{\partial y}), \tag{C.12}$$

$$f\frac{\partial u}{\partial x} = \frac{\partial^2 v}{\partial t \partial x} + \frac{\partial^2 p}{\partial x \partial y}. \tag{C.13}$$

Substituting (C.11) and (C.13) into (C.9), we obtain

$$\frac{\partial}{\partial t} f(\frac{\partial v}{\partial x} - \frac{\partial u}{\partial y}) = f^2 \frac{\partial w}{\partial z}. \tag{C.14}$$

We then take $\frac{\partial}{\partial x}$ of (C.1)

$$f\frac{\partial v}{\partial x} = \frac{\partial^2 u}{\partial t \partial x} + \frac{\partial^2 p}{\partial x^2} \tag{C.15}$$

and $\frac{\partial}{\partial y}$ of (C.2)

$$-f\frac{\partial u}{\partial y} = \frac{\partial^2 p}{\partial y^2} + \frac{\partial^2 v}{\partial t \partial y}. \tag{C.16}$$

Subtracting (C.16) from (C.15), we obtain

$$f\frac{\partial v}{\partial x} - f\frac{\partial u}{\partial y} = \frac{\partial^2 u}{\partial t \partial x} + \frac{\partial^2 p}{\partial x^2} + \frac{\partial^2 p}{\partial y^2} + \frac{\partial^2 v}{\partial t \partial y}, \tag{C.17}$$

and using (C.8), we rewrite (C.17) as

$$f(\frac{\partial v}{\partial x} - \frac{\partial u}{\partial y}) = \frac{\partial}{\partial t}(\frac{\partial u}{\partial x} + \frac{\partial v}{\partial y}) + \nabla^2 p, \tag{C.18}$$

and taking $\frac{\partial}{\partial t}$

$$\frac{\partial}{\partial t} f(\frac{\partial v}{\partial x} - \frac{\partial u}{\partial y}) = \frac{\partial^2}{\partial t^2}(\frac{\partial u}{\partial x} + \frac{\partial v}{\partial y}) + \frac{\partial}{\partial t}\nabla^2 p. \tag{C.19}$$

Substituting (C.14) and (C.5) into (C.19), we obtain

$$f^2\frac{\partial w}{\partial z}+\frac{\partial^2}{\partial t^2}\frac{\partial w}{\partial z}-\frac{\partial}{\partial t}\nabla^2 p. \tag{C.20}$$

To remove the pressure term, we express (C.3) as

$$-\frac{\partial p}{\partial z}=\frac{\partial w}{\partial t}+\rho\frac{g}{\rho_0}. \tag{C.21}$$

Taking $\frac{\partial}{\partial z}$ of (C.20) and substituting (C.21), we obtain

$$f^2\frac{\partial^2 w}{\partial z^2}+\frac{\partial^2}{\partial t^2}\frac{\partial^2 w}{\partial z^2}+\frac{\partial}{\partial t}\nabla^2(\frac{\partial w}{\partial t}+\rho\frac{g}{\rho_0})\frac{\partial^2 w}{\partial z^2}(f^2+\frac{\partial}{\partial t^2})+\frac{\partial^2 w}{\partial t^2}\nabla^2+\frac{\partial\rho}{\partial t}\frac{g}{\rho_0}\nabla^2=0. \tag{C.22}$$

From (C.22) we substitute (C.4) and obtain

$$\frac{\partial^2 w}{\partial z^2}(f^2+\frac{\partial}{\partial t^2})+\nabla^2(\frac{\partial^2 w}{\partial t^2}-\frac{g}{\rho_0}\frac{\partial\rho}{\partial z}w)=0. \tag{C.23}$$

Substituting (C.6) into (C.23), we obtain an expression for the internal wave equation

$$\frac{\partial^2 w}{\partial z^2}(f^2+\frac{\partial}{\partial t^2})+w(\frac{\partial^2}{\partial t}+N^2)(\frac{\partial^2}{\partial x^2}+\frac{\partial^2}{\partial y^2})=0. \tag{C.24}$$

Terms are define in Appendix A.

C.2 Polarization relations

To interpret the horizontal azimuth of the horizontal wave vector (φ) in terms of the observed phase of the rotary velocity component (φ_0), we first define the horizontal azimuth of the wave vector

$$\tan\varphi=\frac{l}{k} \tag{C.25}$$

In the case of CCW velocity component rotation

$$k=k_h\sin\varphi_0 \tag{C.26}$$

and

$$l = -k_h \cos\varphi_0, \tag{C.27}$$

and so

$$\tan\varphi = \frac{-\cos\varphi_0}{\sin\varphi_0} \tag{C.28}$$

and

$$\varphi = \tan^{-1}\frac{-\cos\varphi_0}{\sin\varphi_0}. \tag{C.29}$$

In the case of CW velocity component rotation

$$k = k_h \sin\varphi_0 \tag{C.30}$$

and

$$l = k_h \cos\varphi_0, \tag{C.31}$$

and so

$$\tan\varphi = \frac{-\cos\varphi_0}{-\sin\varphi_0} \tag{C.32}$$

and

$$\varphi = \tan^{-1}\frac{-\cos\varphi_0}{-\sin\varphi_0}. \tag{C.33}$$

C.3 Group velocity approximations

The group velocity(C_g) is the gradient of the intrinsic frequency in the vertical wavenumber space:

$$\mathbf{C}_g = \left[\frac{k(N^2-\omega_0^2)^2}{\omega_0 m^2(N^2-f^2)}, \frac{l(N^2-\omega_0^2)^2}{\omega_0 m^2(N^2-f^2)}, -\frac{(\omega_0^2-f^2)(N^2-\omega_0^2)}{\omega_0 m(N^2-f^2)}\right]. \tag{C.34}$$

Under the hydrostatic approximation, $\omega_0 \simeq f$ and $\omega_0 \leqslant N$ so that

$$\mathbf{C}_g \simeq \left[\frac{kN^4}{\omega_0 m^2(N^4-\omega_0^2)}, \frac{lN^2}{\omega_0 m^2(N^2-\omega_0^2)}\right], \tag{C.35}$$

and

$$\mathbf{C}_g \simeq \left[\frac{kN^4}{\omega_0 m^2 N^2}, \frac{lN^4}{\omega_0 m^2 N^2}\right], \tag{C.36}$$

so that

$$\mathbf{C}_g \simeq \left[\frac{kN^2}{\omega_0 m^2}, \frac{lN^2}{\omega_0 m^2}\right]. \tag{C.37}$$

C.4 Aspect ratio derivations

The aspect ratio definition is

$$\frac{E_k}{E_P} = \frac{\omega^2 + f^2}{\omega^2 - f^2}, \tag{C.38}$$

and from the dispersion relation we have

$$\omega^2 - f^2 = \frac{k_h^2(N^2 - \omega^2)}{m^2}, \tag{C.39}$$

and

$$\omega^2 + f^2 = \frac{k_h^2(N^2 - \omega^2)}{m^2} + 2f^2. \tag{C.40}$$

Substituting (C.39) and (C.40) into (C.38) we have

$$\frac{E_k}{E_P} = 1 + \frac{2f^2m^2}{k_h^2N^2 - k_h^2\omega^2}. \tag{C.41}$$

Applying the hydrostatic approximation ($k_h^2\omega^2 = 0$), (C.41) becomes

$$\frac{E_k}{E_P} = 1 + \frac{2f^2m^2}{N^2k_h^2}. \tag{C.42}$$

References

Alford, M. H., 2001: Internal swell generation: The spatial distribution of energy flux from the wind to mixed layer near-inertial motions. *Journal of Physical Oceanography*, **31 (8)**, 2359–2368, doi:{10.1175/1520-0485(2001)031⟨2359:ISGTSD⟩2.0.CO;2}.

Alford, M. H., 2003: Improved global maps and 54-year history of wind-work on ocean inertial motions. *Geophysical Research Letters*, **30 (8)**, 1424.

Alford, M. H., M. F. Cronin, and J. M. Klymak, 2012: Annual Cycle and Depth Penetration of Wind-Generated Near-Inertial Internal Waves at Ocean Station Papa in the Northeast Pacific. *Journal of Physical Oceanography*, **42 (6)**, 889–909, doi:{10.1175/JPO-D-11-092.1}.

Alford, M. H. and M. C. Gregg, 2001: Near-inertial mixing: Modulation of shear, strain and microstructure at low latitude. *Journal of Geophysical Research*, **106 (C8)**, 16,947–16,968.

Alford, M. H., M. C. Gregg, V. Zervakis, and H. Kontoyiannis, 2012: Internal wave measurements on the Cycladic Plateau of the Aegean Sea. *Journal of Geophysical Research*, **117**, C01 015.

Alford, M. H., J. A. MacKinnon, Z. Zhao, R. Pinkel, J. M. Klymak, and T. Peacock, 2007: Internal waves across the Pacific. *Geophysical Research Letters*, **34**, L24 601.

Badin, G., R. J. Williams, Z. Jing, and L. Wu, 2013: Water mass transformations in the southern ocean diagnosed from observations: Contrasting

effects of air-sea fluxes and diapycnal mixing. *Journal of Physical Oceanography*, **43**, 1472–1484.

Balmforth, N. J. and W. R. Young, 1999: Radiative damping of near-inertial oscillations in the mixed layer. *Journal of Marine Research*, **57 (4)**, 561–584, doi:{10.1357/002224099321549594}.

Belkin, I. M. and A. L. Gordon, 1996: Southern Ocean fronts from the Greenwich meridian to Tasmania. *Journal of Geophysical Research - Oceans*, **101 (C2)**, 3675–3696, doi:{10.1029/95JC02750}.

Bell, T. H., 1975: Topographically generated internal waves in open ocean. *Journal of Geophysical Research*, **80 (3)**, 320–327.

Bray, N. A. and N. P. Fofonoff, 1981: Available potential-energy for mode eddies. *Journal of Physical Oceanography*, **11 (1)**, 30–47.

Brearley, J. A., K. L. Sheen, A. C. Naveira Garabato, D. A. Smeed, and S. N. Waterman, 2013: Eddy-Induced Modulation of Turbulent Dissipation over Rough Topography in the Southern Ocean. *Journal of Physical Oceanography*, **43**, 2288–2308.

Brillouin, L., 1926: Remarques sur la mécanique ondulatoire. *J. de Physique*, **7**, 353–368.

Bryan, F., 1987: Parameter sensitivity of primitive equation ocean general-circulation models. *Journal of Physical Oceanography*, **17 (7)**, 970–985, doi:{10.1175/1520-0485(1987)017⟨0970:PSOPEO⟩2.0.CO;2}.

Bühler, O. and M. E. McIntyre, 2005: Wave capture and wave-vortex duality. *Journal of Fluid Mechanics*, **534**, 67–95.

Cairns, J. L. and G. O. Williams, 1976: Internal wave observations from a midwater float .2. *Journal of Geophysical Research*, **81 (12)**, 1943–1950.

Crawford, W. R., 1986: A comparison of length scales and decay times of turbulence in stably stratisfied flows. *Journal of Physical Oceanography*,

16 (11), 1847–1854, doi:10.1175/1520-0485(1986)016⟨1847:ACOLSA⟩2.0.CO;2.

Crawford, W. R. and R. K. Dewey, 1990: Confidence-limits for friction velocity determined from turbulence profiles in coastal waters. *Journal of Atmospheric and Oceanic Technology*, **7 (1)**, 50–57, doi:10.1175/1520-0426(1990)007⟨0050:CLFFVD⟩2.0.CO;2.

Cushman-Roisin, B. and J.-M. Beckers, 2006: *Introduction to geophysical Fluid Dynamics Physical and Numerical Aspects*. Academic Press.

Da Silva, J. C. B., J. M. Magalhães, T. Gerkema, and L. R. M. Maas, 2012: Internal Solitary Waves in the Red Sea. *Oceanography*, **25 (2)**, 96–107.

Damerell, G. M., K. J. Heywood, and D. P. Stevens, 2013: Direct observations of the Antarctic circumpolar current transport on the northern flank of the Kerguelen Plateau. *Journal of Geophysical Research - Oceans*, **118 (3)**, 1333–1348.

Damerell, G. M., K. J. Heywood, D. P. Stevens, and A. C. N. Garabato, 2012: Temporal Variability of Diapycnal Mixing in Shag Rocks Passage. *Journal of Physical Oceanography*, **42 (3)**, 370–385, doi:{10.1175/2011JPO4573.1}.

D'Asaro, E. A. and R. C. Lien, 2000: The wave-turbulence transition for stratified flows. *Journal of Physical Oceanography*, **30**, 1669–1678.

D'Asaro, E. A. and M. D. Morehead, 1991: Internal waves and velocity finestructure in the Arctic Ocean. *Journal of Geophysical Research*, **96 (12)**, 725–738.

Davis, R., 1996: Sampling turbulent dissipation. *Journal of Physical Oceanography*, **26**, 341–358.

de Boyer Montégut, C., G. Madec, A. Fischer, A. Lazar, and D. Ludicone, 2004: Mixed layer depth over the global ocean: An examination of profile data and a profile-based climatology. *Journal of Geophysical Research - Oceans*, **109 (C12)**, doi:{10.1029/2004JC002378}.

Dillon, T. M., 1982: Vertical overturns - a comparison of thorpe and ozmidov length scales. *Journal of Geophysical Research*, **87 (NC12)**, 9601–9613.

Dong, S., J. Sprintall, S. T. Gille, and L. D. Talley, 2008: Southern Ocean mixed-layer depth from Argo float profiles. *Journal of Geophysical Research - Oceans*, **113 (C06013)**.

Efron, B., 1979: Bootstrap methods: Another look at the jackknife. *The Annals of Statistics*, **7 (1)**, 1–26.

Egbert, G. D. and R. D. Ray, 2000: Significant dissipation of tidal energy in the deep ocean inferred from satellite altimeter data. *Nature*, **405**, 775–778.

Elipot, S., R. Lumpkin, and G. Prieto, 2010: Modification of inertial oscillations by the mesoscale eddy field. *Journal of Geophysical Research - Oceans*, **115**, doi:{10.1029/2009JC005679}.

Fer, I., R. Skogseth, and F. Geyer, 2010: Internal Waves and Mixing in the Marginal Ice Zone near the Yermak Plateau. *Journal of Physical Oceanography*, **40 (7)**, 1613–1630, doi:10.1175/2010JPO4371.1.

Ferrari, R. and C. Wunsch, 2009: Ocean circulation kinetic energy: Reservoirs, sources adn sinks. *Annual Review of Fluid Mechanics*, **41**, 253–282.

Ferron, B., H. Mercier, K. Speer, A. Gargett, and K. Polzin, 1998: Mixing in the Romanche Fracture Zone. *Journal of Physical Oceanography*, **28 (10)**, 1929–1945.

Finnigan, T. D., D. S. Luther, and R. Lukas, 2002: Observations of enhanced diapycnal mixing near the Hawaiian ridge. *Journal of Physical Oceanography*, **32 (11)**, 2988–3002.

Fofonoff, N. P., 1966: Oscillation modes of a deep-sea mooring. *Geo-Marine Technology*, **2**, 13–17.

Fofonoff, N. P., 1969: Spectral characteristics of internal waves in the ocean. *Deep-Sea Research*, **S**, 59–71.

Galbraith, P. S. and D. E. Kelley, 1996: Identifying overturns in CTD profiles. *Journal of Atmospheric and Oceanic Technology*, **13 (3)**, 688–702, doi: 10.1175/1520-0426(1996)013⟨0688:IOICP⟩2.0.CO;2.

Garrett, C., 2003: Mixing with latitude. *Nature*, **422 (6931)**, 477–478.

Garrett, C. and W. Munk, 1975: Space-time scales of internal waves - progress report. *Journal of Geophysical Research*, **80 (3)**, 291–297.

Garrett, C. and W. H. Munk, 1972: Oceanic mixing by breaking internal waves. *Deep-Sea Research*, **19 (12)**, 823–832, doi:{10.1016/0011-7471(72) 90001-0}.

Garrett, C. and W. H. Munk, 1979: Internal waves in the ocean. *Annual Review of Fluid Mechanics*, **11**, 339–369.

Glover, D. M., W. J. Jenkins, and S. C. Doney, 2011: *Modelling Methods for Marine Science*. Cambridge University Press.

Gonella, J., 1972: A rotary-component method for analysing meteorological and oceanographic vector time series. *Deep-Sea Research*, **19**, 833–846.

Gordon, A. L., 1986: Is there a global scale ocean circulation? *Eos, Transactions American Geophysical Union*, **67 (9)**, 109–110.

Gregg, M. C., 1987: Diapycnal mixing in the thermocline - a review. *Journal of Geophysical Research*, **92 (C5)**, 5249–5286.

Gregg, M. C., 1989: Scaling turbulent dissipation in the thermocline. *Journal of Geophysical Research*, **94 (C7)**, 9686–9698.

Gregg, M. C., C. S. Cox, and P. W. Hacker, 1973: Vertical Microstructure Measurements in the Central North Pacific. *Journal of Physical Oceanography*, **3 (458-469)**.

Gregg, M. C., T. B. Sanford, and D. P. Winkel, 2003: Reduced mixing from the breaking of internal waves in equatorial waters. *Nature*, **422 (6931)**, 513–515.

Gurvich, A. S. and A. M. Yaglom, 1967: Breakdown of eddies and probability distributions for small-scale turbulence. *Physics of Fluids*, **10 (9P2)**, doi: 10.1063/1.1762505.

Harrison, m. and R. Hallberg, 2008: Pacific subtropical cell response to reduced equatorial dissipation. *Journal of Physical Oceanography*, **38**, 1894–1912.

Henyey, F. S., J. Wright, and S. M. Flatte, 1986: Energy and Action Flow Through the Internal Wave Field: an Eikonal Approach. *Journal of Geophysical Research*, **91 (C7)**, 8487–8495.

Heywood, K. J. and Garabato, A. C. N. and Stevens, D. P., 2002: High mixing rates in the abyssal Southern Ocean. *Nature*, **415 (6875)**, 1011–1014.

Holte, J., L. D. Talley, T. K. Chereskin, and B. M. Sloyan, 2012: The role of air-sea fluxes in Subantarctic Mode Water formation. *Journal of Geophysical Research*, **117**.

Huang, R. X., 1999: Mixing and energetics of the thermocline circulation. *Journal of Physical Oceanography*, **29 (4)**, 727–746.

Ivey, G. N., K. B. Winters, and J. R. Koseff, 2008: Density stratification, turbulence, but how much mixing? *Annual Review of Fluid Mechanics*, **40**, 169–184, doi:{10.1146/annurev.fluid.39.050905.110314}.

Jing, Z. and L. Wu, 2010: Seasonal variation of turbulent diapycnal mixing in the northwestern Pacific stirred by wind stress. *Geophysical Research Letters*, **37**, doi:{10.1029/2010GL045418}.

Jing, Z. and L. Wu, 2013: Low-frequency modulation of turbulent diapycnal mixing by anticyclonic eddies inferred from the hot time series. *Journal of Physical Oceanography*, **43**, 824–835.

Johnson, G. C., J. M. Toole, and N. G. Larson, 2007: Sensor corrections for sea-bird SBE-41CP and SBE-41 CTDs. *Journal of Atmospheric and Oceanic Technology*, **24 (6)**, 1117–1130.

Johnson, H. L. and C. Garrett, 2004: Effects of noise on Thorpe scales and run lengths. *Journal of Physical Oceanography*, **34 (11)**, 2359–2372, doi:{10.1175/JPO2641.1}.

Kantha, L. H. and C. A. Clayson, 2000: *Small Scale Processes in Geophysical Fluid Flows*, Vol. 67. Academic Press.

Klymak, J. M., M. Buijsman, S. Legg, and R. Pinkel, 2013: Parameterizing surface and internal tide scattering and breaking on supercritical topography: the one- and two-ridge cases. *Journal of Physical Oceanography*, **43**, 1380–1397.

Klymak, J. M., R. Pinkel, and L. Rainville, 2008: Direct breaking of the internal tide near topography: Kaena Ridge, Hawaii. *Journal of Physical Oceanography*, **38 (2)**, 380–399, doi:{10.1175/2007JPO3728.1}.

Kramers, H. A., 1926: Wellenmechanik und halbzahlige quantisierung. *Zeits. f. Physik*, **39**, 828–840.

Kunze, E., 1985: Near-inertial wave-propagation in geostrophic shear. *Journal of Physical Oceanography*, **15 (5)**, 544–565.

Kunze, E., E. Firing, J. M. Hummon, T. K. Chereskin, and A. M. Thurnherr, 2006: Global abyssal mixing inferred from lowered ADCP shear and CTD strain profiles. *Journal of Physical Oceanography*, **36 (12)**, 2350–2352.

Langlais, C., S. Rintoul, and A. Schiller, 2011: Variability and mesoscale activity of the Southern Ocean fronts: Identification of a circumpolar coordinate system. *Ocean Modelling*, **39 (1-2, SI)**, 79–96, doi:{10.1016/j.ocemod.2011.04.010}.

Leaman, K. D. and T. B. Sanford, 1975: Vertical energy propagation of internal waves - vector spectral analysis of velocity profiles. *Journal of Geophysical Research*, **80 (15)**, 1975–1978.

Ledwell, J. R., E. T. Montgomery, K. L. Polzin, L. C. St Laurent, R. W. Schmitt, and J. M. Toole, 2000: Evidence for enhanced mixing over rough topography in the abyssal ocean. *Nature*, **403 (6766)**, 179–182.

Ledwell, J. R., L. C. St Laurent, J. B. Girton, and J. M. Toole, 2011: Diapycnal Mixing in the Antarctic Circumpolar Current. *Journal of Physical Oceanography*, **41**.

Ledwell, J. R., A. J. Watson, and C. S. Law, 1993: Evidence for slow mixing across the pycnocline from an open-ocean tracer-release experiment. *Nature*, **364 (6439)**, 701–703.

Ledwell, J. R., A. J. Watson, and C. S. Law, 1998: Mixing of a tracer in the pycnocline. *Journal of Geophysical Research - Oceans*, **103 (C10)**, 21 499–21 529.

Levitus, S. and T. P. Boyer, 1994: World ocean atlas 1994. Noaa atlas nesdis 4, U.S. Department of Commerce, 117 pp., Washington D.C.

Love, A. E. H., 1891: Wave motion in a heterogeneous heavy liquid. *Proceedings London Mathematical Society*, **22 (S1)**, 307–316.

Lueck, R. G., 1988: Turbulent mixing at the Pacific Sub-Tropical Front. *Journal of Physical Oceanography*, **18 (12)**, 1761–1774, doi:10.1175/1520-0485(1988)018⟨1761:TMATPS⟩2.0.CO;2.

Lueck, R. G. and J. J. Picklo, 1990: Thermal Inertia of Conductiviyt Cells: Oberservations with a Sea-Bird Cell. *Journal of Atmospheric and Oceanic Technology*, **7**, 756–768.

Lueck, R. G. and R. Reid, 1984: On the production and dissipation of mechanical energy in the ocean. *Journal of Geophysical Research - Oceans*, **89 (NC3)**, 3439–3445, doi:{10.1029/JC089iC03p03439}.

Lumpkin, R. and K. Speer, 2007: Global ocean meridional overturning. *Journal of Physical Oceanography*, **37**, 2550–2562.

Lvov, Y. V., K. L. Polzin, and E. G. Tabak, 2004: Energy spectra of the ocean's internal wave field: Theory and observations. *Physical Review Letters*, **92 (12)**, doi:10.1103/PhysRevLett.92.128501.

MacKinnon, J. A., M. H. Alford, R. Pinkel, J. Klymak, and Z. Zhao, 2011: Mixing across the Pacific. *Journal of Physical Oceanography*.

Mauritzen, C., K. L. Polzin, M. S. McCartney, R. C. Millard, and D. E. West-Mack, 2002: Evidence in hydrography and density fine structure for enhanced vertical mixing over the Mid-Atlantic Ridge in the western Atlantic. *Journal of Geophysical Research*, **vol.107, no.C10**, 11–1–19.

McComas, C. H. and P. Muller, 1981: The dynamic balance of internal waves. *Journal of Physical Oceanography*, **11 (7)**, 970–986, doi:{10.1175/1520-0485(1981)011⟨0970:TDBOIW⟩2.0.CO;2}.

Meijers, A. J. S., N. L. Bindoff, and S. R. Rintoul, 2011: Estimating the Four-Dimensional Structure of the Southern Ocean Using Satellite Altimetry. *Journal of Atmospheric and Oceanic Technology*, **28 (4)**, 548–568, doi:{10.1175/2010JTECHO790.1}.

Meredith, M. P. and A. C. Naveira Garabato, 2012: Sensitivity of the overturning circulation in the Southern Ocean to decadal changes in wind forcing. *Journal of Climate*, **25**, 99–110.

Morison, J., R. Andersen, N. Larson, E. Dasaro, and T. Boyd, 1994: The correction for thermal-lag effects in Sea-Bird CTD data. *Journal of atmospheric and oceanic technology*, **11 (4, Part 2)**, 1151–1164.

Moum, J. N. and R. G. Lueck, 1985: Causes and implications of noise in oceanic dissipation measurements. *Deep-Sea research Part A-Oceanographic Research Papers*, **32 (4)**, 379–390, doi:10.1016/0198-0149(85)90086-X.

Müller, P., G. Holloway, F. Henyey, and N. Pomphrey, 1986: Nonlinear-interactions among internal gravity-waves. *Reviews of Geophysics*, **24 (3)**, 493–536.

Müller, P., D. Olbers, and J. Willebrand, 1978: IWEX spectrum. *Journal of Geophysical Research*, **83**, 479–500.

Munk, W. H., 1966: Abyssal recipes. *Deep-Sea Research*, **13**, 707–730.

Nansen, F., 1902: The Oceanography of the North Polar Basin. *Scientific Research Norwegian North Pole Expedition 1893-1896*, **3 (9)**, 427.

Naveira Garabato, A. C., 2009: RRS James Cook Cruise 29, 01 Nov-22 Dec 2008. SOFine Cruise Report: Southern Ocean Finestructure. Southampton Cruise Report 35, National Oceanography Centre.

Naveira Garabato, A. C., K. I. C. Oliver, A. J. Watson, and M. J. Messias, 2004: Turbulent diapycnal mixing in the Nordic seas. *Journal of Geophysical Research - Oceans*, **109 (C12)**, doi:{10.1029/2004JC002411}.

Naveira Garabato, A. C., K. L. Polzin, B. A. King, K. J. Heywood, and M. Visbeck, 2004: Widespread intense turbulent mixing in the Southern Ocean. *Science*, **303 (5655)**, 210–213.

Naveira Garabato, A. C., D. P. Stevens, A. J. Watson, and W. Roether, 2007: Short-circuiting of the overturning circulation in the antarctic circumpolar current. *Nature*, **447**, 194–197.

Nikurashin, M. and R. Ferrari, 2010: Radiation and Dissipation of Internal Waves Generated by Geostrophic Motions Impinging on Small-Scale Topography: Application to the Southern Ocean. *Journal of Physical Oceanography*, **40 (9)**, 2025–2042, doi:10.1175/2010JPO4315.1.

Nikurashin, M. and R. Ferrari, 2011: Global energy conversion rate from geostrophic flows into internal lee waves in the deep ocean. *Geophysical Research Letters*, **38 (L08610)**.

Nikurashin, M. and R. Ferrari, 2013: Overturning circulation driven by breaking internal waves in the deep ocean. *Geophysical Research Letters*, **40**, 1–5.

Nikurashin, M. and G. K. Vallis, 2012: A Theory of the Interhemispheric Meridional Overturning Circulation and Associated Stratification. *Journal of Physical Oceanography*, **42 (1652-1667)**.

Nycander, J., 2005: Generation of internal waves in the deep ocean by tides. *Journal of Geophysical Research*, **110 (C10028)**.

Orsi, A. H., T. Whitworth, and W. D. Nowlin, 1995: On the meridional extent and fronts of the Antarctic Circumpolar Current. *Deep-Sea Research Part I-Oceanographic Research Papers*, **42 (5)**, 641–673, doi:{10.1016/0967-0637(95)00021-W}.

Osborn, A. R. and T. L. Burch, 1980: Internal solitons in the Andaman Sea. *Science*, **208**, 451–460.

Osborn, T. R., 1980: Estimates of the local-rate of vertical diffusion from dissipation measurements. *Journal of Physical Oceanography*, **10 (1)**, 83–89.

Osborn, T. R. and R. G. Lueck, 1985: Turbulence measurements with a submarine. *Journal of Physical Oceanography*, **15 (11)**, 1502–1520, doi:10.1175/1520-0485(1985)015⟨1502:TMWAS⟩2.0.CO;2.

Ozmidov, R. V., 1965: On the turbulent exchange in a stably stratified ocean. *Izv. Acad. Sci. URSS, Atmos. Oceanic Phys.*, **1**, 861–871.

Park, Y. H., E. Charriaud, and M. Fieux, 1998: Thermohaline structure of the Antarctic Surface Water Winter Water in the Indian sector of the Southern Ocean. *Journal of Marine Systems*, **17 (1-4)**, 5–23, doi:{10.1016/S0924-7963(98)00026-8}, International JGOFS Symposium on Carbon Fluxes and Dynamic Processes in the Southern Ocean - Present and Past, BREST, FRANCE, AUG 28-31, 1995.

Park, Y. H., J. L. Fuda, I. Durand, and A. C. N. Garabato, 2008: Internal tides and vertical mixing over the Kerguelen Plateau. *Deep-Sea Research Part II-Topical Studies in Oceanography*, **55 (5-7)**, 582–593.

Pedlosky, J., 2003: *Waves in the Ocean and Atmosphere: Introduction to Waves Dynamics*. Springer.

Peltier, W. R. and C. P. Caulfield, 2003: Mixing efficiency in stratified shear flows. *Annual Review of Fluid Mechanics*, **35**, 135–167.

Phillips, H. E. and N. L. Bindoff, 2014: Ocean velocity from EM-APEX profilers: A comparison with traditional measurements. *Journal of Atmospheric and Oceanic Technology*, **Submitted**.

Phillips, O. M., 1977: *The Dynamics of the Upper Ocean*. Cambridge University Press.

Pickard, G. L. and W. J. Emery, 1990: *Descriptive Physical Oceanography An Introduction*. 5th ed., Pergamon Press.

Pinot, J. M., P. Velez, J. Tintore, and J. L. LopezJurado, 1997: The thermal-lag effect in SBE-25 CTDs: Importance of correcting data collected in the Mediterranean summer thermocline. *CIENTIA MARINA*, **61 (2)**, 221–225.

Pol, A. and C. Jermaine, 2005: Relational confidence bounds are easy with the bootstrap*. *SIGMOD Conference*, ACM, Ed., 587–598.

Pollard, R. T. and R. C. Millard, 1970: Comparison between observed and simulated wind-generated inertial oscillations. *Deep-Sea Research*, **17**, 813–821.

Polzin, K., 2004: A heuristic description of internal wave dynamics. *Journal of Physical Oceanography*, **34 (1)**, 214–230.

Polzin, K., E. Kunze, J. Hummon, and E. Firing, 2002: The finescale response of lowered ADCP velocity profiles. *Journal of Atmospheric and Oceanic Technology*, **19 (2)**, 205–224.

Polzin, K. L., 2008: Mesoscale Eddy-Internal Wave Coupling. Part I: Symmetry, Wave Capture, and Results from the Mid-Ocean Dynamics Experiment. *Journal of Physical Oceanography*, **38 (11)**, 2556–2574.

Polzin, K. L., E. Kunze, J. M. Toole, and R. W. Schmitt, 2003: The partition of finescale energy into internal waves and subinertial motions. *Journal of Physical Oceanography*, **33**, 234–248.

Polzin, K. L. and Y. V. Lvov, 2011: Toward regional characterizations of the oceanic internal wavefield. *Reviews of Geophysics*, **49 (RG4003)**.

Polzin, K. L., A. C. Naveira Garabato, T. N. Huussen, B. M. Sloyan, and S. N. Waterman, 2013: Finescale parameterizations of turbulent dissipation. *Submitted*.

Polzin, K. L., J. M. Toole, J. R. Ledwell, and R. W. Schmitt, 1997: Spatial variability of turbulent mixing in the abyssal ocean. *Science*, **276 (5309)**, 93–96.

Polzin, K. L., J. M. Toole, and R. W. Schmitt, 1995: Finescale parameterizations of turbulent dissipation. *Journal of Physical Oceanography*, **25 (3)**, 306–328.

Rayleigh, L., 1912: On the propagation of waves through a stratified medium, with special reference to the question of reflection. *Proceedings of Royal Society London*, **86**, 207–226.

Ridgway, K. R., J. R. Dunn, and J. L. Wilkin, 2002: Ocean Interpolation by Four-Dimensional Weighted Least Squares - Application to the Waters around Australasia. *Journal of Atmospheric and Oceanic Technology*, **19**, 1357–1375.

Rintoul, S. R. and A. C. Naveira Garabato, 2013: *Ocean Circulation and Climate: A 21st Century Perspective*, chap. Dynamics of the Southern Ocean Circulation, 471–492. 2d ed., No. 103 in International Geophysics, Oxford, GB, Academic Press.

Ruddick, B. and K. Richards, 2003: Oceanic thermohaline intrusions: observations. *Progress in Oceanography*, **56**, 499–527.

Sallee, J. B., K. Speer, and R. Morrow, 2008: Response of the Antarctic Circumpolar Current to atmospheric variability. *Journal of Climate*, **21 (12)**, 3020–3039, doi:{10.1175/2007JCLI1702.1}.

Sallee, J. B., K. G. Speer, and S. R. Rintoul, 2010: Zonally asymmetric response of the Southern Ocean mixed-layer depth to the Southern Annular Mode. *Nature Geoscience*, **3 (4)**, 273–279, doi:10.1038/NGEO812.

Sanford, T. B., 1971: Motionally Induced Electric and Magnetic Fields in the Sea. *Journal of Geophysical Research*, **76 (15)**, 3476–3493.

Sanford, T. B., R. G. Drever, and J. H. Dunlap, 1974: The Design and Performance of a Free-Fall Electro-Magnetic Velocity Profiler (EMVP). Tech. Rep. AD0786315, Woods Hole Oceanographic Institution Mass.

Sanford, T. B., R. G. Drever, and J. H. Dunlap, 1978: A velocity profiler based on the principles of geomagnetic induction. *Deep-Sea Research*, **25 (2)**, 183–210.

Sanford, T. B., J. H. Dunlap, J. A. Carlson, D. C. Webb, and J. B. Girton, 2005: Autonomous velocity and density profiler: EM-APEX. *Proceedings of the IEEE/OES eighth working conference on current measurement technology - Proceedings*, 152–156.

Sanford, T. B., J. F. Price, and J. B. Girton, 2011: Upper-Ocean Response to Hurricane Frances (2004) Observed by Profiling EM-APEX Floats. *Journal of Physical Oceanography*, **41 (6)**, 1041–1056, doi:{10.1175/2010JPO4313.1}.

Schmitz, W. J., 1995: On the interbasin-scale thermohaline circulation. *Reviews of Geophysics*, **33**, 151–173.

Scott, R. B. and Y. Xu, 2009: An update on the wind power input to the surface geostrophic flow of the world ocean. *Deep-Sea Research Part I-Oceanographic Research Papers*, **56**, 295–304.

Sheen, K. L., et al., 2013: Rates and mechanisms of turbulent disspiation and mixing in the Southern Ocean: Results from the Diapycnal and Isopycnal Mixing Experiment in the Southern Ocean (DIMES). *Journal of Geophysical Research - Oceans*, **118**, 1–19.

Sloyan, B. M., 2005: Spatial variability of mixing in the Southern Ocean. *Geophysical Research Letters*, **vol.32, no.18**.

Sloyan, B. M., 2006: Antarctic bottom and lower circumpolar deep water circulation in the eastern Indian Ocean. *Journal of Geophysical Research*, **111 (C2)**.

Sloyan, B. M. and S. R. Rintoul, 2001: The southern ocean limb of the global deep overturning circulation. *Journal of Physical Oceanography*, **31 (1)**, 143–173.

Sloyan, B. M., L. D. Talley, T. K. Chereskin, R. Fine, and J. Holte, 2010: Antarctic Intermediate Water and Subantarctic Mode Water Formation in the Southeast Pacific: The Role of Turbulent Mixing. *Journal of Physical Oceanography*, **40 (7)**, 1558–1574, doi:10.1175/2010JPO4114.1.

Smith, W. H. F. and D. T. Sandwell, 1997: Global sea floor topography from satellite altimetry and ship depth soundings. *Science*, **277 (5334)**, 1956–1962, doi:{10.1126/science.277.5334.1956}.

Sokolov, S. and S. R. Rintoul, 2007: Multiple jets of the Antarctic circumpolar current South of Australia. *Journal of Physical Oceanography*, **37 (5)**, 1394–1412.

Sokolov, S. and S. R. Rintoul, 2009a: Circumpolar structure and distribution of the Antarctic Circumpolar Current fronts: 1. Mean circumpolar paths. *Journal of Geophysical Research - Oceans*, **114**, doi: 10.1029/2008JC005108.

Sokolov, S. and S. R. Rintoul, 2009b: Circumpolar structure and distribution of the Antarctic Circumpolar Current fronts: 2. Variability and relationship to sea surface height. *Journal of Geophysical Research - Oceans*, **114**, doi:10.1029/2008JC005248.

St. Laurent, L., A. C. Naveira Garabato, J. R. Ledwell, A. M. Thurnherr, J. M. Toole, and A. J. Watson, 2012a: Turbulence and Diapycnal Mixing in Drake Passage. *Journal of Physical Oceanography*, **42**, 2143–2152.

St. Laurent, L. C., M. H. Alford, and T. Paluszkiewicz, 2012b: An introduction to the special issue on internal waves. *Oceanography*, **25 (2)**, 15–19.

St. Laurent, L. C., J. M. Toole, and R. W. Schmitt, 2001: Buoyancy forcing by turbulence above rough topography in the abyssal Brazil Basin. *Journal of Physical Oceanography*, **31**, 3476–3495.

Stansfield, K., C. Garrett, and R. Dewey, 2001: The probability distribution of the Thorpe displacement within overturns in Juan de Fuca Strait. *Journal of Physical Oceanographyy*, **31 (12)**, 3421–3434, doi: 10.1175/1520-0485(2001)031⟨3421:TPDOTT⟩2.0.CO;2.

Stokes, G. G., 1847: On the theory of oscillatory waves. *Transactions of the Cambridge Philosophical Society*, **8**, 127–137.

Sun, O. and R. Pinkel, 2012: Energy transfer from high-shear, low-frequency internal waves to high-frequency waves near Kaena Ridge, Hawaii. *Journal of Physical Oceanography*, **42**, 1524–1547.

Talley, L. D., 2013: Closure of the global overturning circulation through the Indian, Pacific, and Southern Oceans: Schematics and transports. *Oceanography*, **26 (1)**, 80–97.

Talley, L. D., G. L. Pickard, W. J. Emery, and J. H. Swift, 2011: *Descriptive Physical Oceanography An Introduction*. 6th ed., Elsevier.

Thompson, A. F., S. T. Gille, J. A. MacKinnon, and J. Sprintall, 2007: Spatial and temporal patterns of small-scale mixing in Drake Passage. *Journal of Physical Oceanography*, **37 (3)**, 572–592.

Thorpe, S. A., 1977: Turbulence and mixing in a Scottish Loch. *Philosophical transactions of the royals society of London series A-Mathematical Physical and Engineering Sciences*, **286 (1334)**, 125–181.

Thorpe, S. A., 2005: *The Turbulent Ocean*. 439p, Cambridge University Press.

Thoulet, J., 1894: Contribution a l'étude des lacs des Vosges. *Bulletin de la Societe de Geographic (Paris)*, **15 (7)**, 557–604.

Vallis, G. K., 2006: *Atmopsheric and Oceanic Fluid Dynamics*. 745pp, Cambridge University Press.

Van Haren, H. and L. Gostiaux, 2012: Energy release through internal wave breaking. *Oceanography*, **25 (2)**, 124–131.

van Meurs, P., 1998: Interactions between near-inertial mixed layer currents and the mesoscale: The importance of spatial variabilities in the vorticity field. *Journal of Physical Oceanography*, **28 (7)**, 1363–1388, doi:{10.1175/1520-0485(1998)028⟨1363:IBNIML⟩2.0.CO;2}.

Walin, G., 1982: On the relation between sea-surface heat flow and thermal circulation in the ocean. *Tellus*, **34**, 187–195.

Watanabe, M. and T. Hibiya, 2002: Global estimates of the wind-induced energy flux to inertial motions in the surface mixed layer. *Geophysical Research Letters*, **29 (8)**, doi:{10.1029/2001GL014422}.

Waterman, S. N., A. C. Naveira Garabato, and K. L. Polzin, 2013: Internal Waves and Turbulence in the Antarctic Circumpolar Current. *Journal of Physical Oceanography*, **43**, 259–282.

Watson, E. R., 1903: Internal oscillation in the water of Loch Ness, as indicated by temperature observations. *Nature*, **69**, 174.

Wentzel, G., 1926: Eine Verallgemeinerung der Quantenbedingungen für die Zwecke der Wellen-mechanik. *Zeits. f. Physik*, **38**, 518–529.

Whalen, C. B., L. D. Talley, and J. A. MacKinnon, 2012: Spatial and temporal variability of global ocean mixing inferred from argo profiles. *Geophysical Research Letters*, **39**, L18 612.

Whitworth, T. and W. D. Nowlin, 1987: Water masses and currents of the Southern-Ocean at the Greenwich meridian. *Journal of Geophysical Research - Oceans*, **92 (C6)**, 6462–6476, doi:{10.1029/JC092iC06p06462}.

Winters, K. B. and E. A. D'Asaro, 1997: Direct simulation of internal wave energy transfer. *Journal of Physical Oceanography*, **27 (9)**, 1937–1945, doi:{10.1175/1520-0485(1997)027⟨1937:DSOIWE⟩2.0.CO;2}.

Wu, L., Z. Jing, S. Riser, and M. Visbeck, 2011: Seasonal and spatial variations of Southern Ocean diapycnal mixing from Argo profiling floats. *Nature Geoscience*, **4 (6)**, 363–366, doi:{10.1038/NGEO1156}.

Wunsch, C., 1998: The work done by the wind on the oceanic general circulation. *Journal of Physical Oceanography*, **28 (11)**, 2332–2340, doi:{10.1175/1520-0485(1998)028⟨2332:TWDBTW⟩2.0.CO;2}.

Wunsch, C. and R. Ferrari, 2004: Vertical mixing, energy and the general circulation of the oceans. *Annual Review of Fluid Mechanics*, **36**, 281–314.

Yamazaki, H. and R. G. Lueck, 1990: Why oceanic dissipation rates are not lognormal. *Journal of Physical Oceanography*, **20 (1907-1918)**.

Zheng, Q., V. Klemas, and X. H. Yan, 2002: Advance instudies of ocean internal waves observed from space. *Recent Research Developments in Geophysics*, **4**, 143–156.